POLYPUBLIE
Polytechnique Montréal

POLYTECHNIQUE MONTRÉAL
UNIVERSITÉ D'INGÉNIERIE

Titre: Title: 3D Numerical Modeling of Transient Conditions in Francis Turbines

Auteur: Author: Hossein Hosseinimanesh

Date: 2016

Type: Mémoire ou thèse / Dissertation or Thesis

Référence: Citation: Hosseinimanesh, H. (2016). 3D Numerical Modeling of Transient Conditions in Francis Turbines [Ph.D. thesis, École Polytechnique de Montréal]. PolyPublie. https://publications.polymtl.ca/2104/

Document en libre accès dans PolyPublie
Open Access document in PolyPublie

URL de PolyPublie: PolyPublie URL: https://publications.polymtl.ca/2104/

Directeurs de recherche: Advisors: Marcelo Reggio, & François Guibault

Programme: Program: Génie mécanique

Ce fichier a été téléchargé à partir de PolyPublie, le dépôt institutionnel de Polytechnique Montréal
This file has been downloaded from PolyPublie, the institutional repository of Polytechnique Montréal

https://publications.polymtl.ca

UNIVERSITÉ DE MONTRÉAL

3D NUMERICAL MODELING OF TRANSIENT CONDITIONS IN FRANCIS TURBINES

HOSSEIN HOSSEINIMANESH

DÉPARTEMENT DE GÉNIE MÉCANIQUE

ÉCOLE POLYTECHNIQUE DE MONTRÉAL

THÈSE PRÉSENTÉE EN VUE DE L'OBTENTION

DU DIPLÔME DE PHILOSOPHIAE DOCTOR

(GÉNIE MÉCANIQUE)

AVRIL 2016

© Hossein Hosseinimanesh, 2016.

UNIVERSITÉ DE MONTRÉAL

ÉCOLE POLYTECHNIQUE DE MONTRÉAL

Cette thèse intitulée :

3D NUMERICAL MODELING OF TRANSIENT CONDITIONS IN FRANCIS TURBINES

présentée par : HOSSEINIMANESH Hossein

en vue de l'obtention du diplôme de : Philosophiae Doctor

a été dûment acceptée par le jury d'examen constitué de :

M. VO Huu Duc, Ph. D., président

M. REGGIO Marcelo, Ph. D., membre et directeur de recherche

M. GUIBAULT François, Ph. D., membre et codirecteur de recherche

M. TRÉPANIER Jean-Yves, Ph. D., membre

M. PARASCHIVOIU Marius, Ph. D., membre externe

DEDICATION

To my beloved family Mohammad, Zahra, Ahmad and Golriz

ACKNOWLEDGEMENTS

I would like to take this opportunity to express sincere gratitude to my supervisors, Professor Francois Guibault and Professor Marcello Reggio for their excellent guidance, caring, patience, suggestions and availability during my research.

I gratefully acknowledge Dr. Christophe Devals for his support and share valuable expertise from the initial to the final level of the project. I would also thank Dr. Julien Dompierre and Dr. Marie-Gabrielle Vallet for providing valuable comments and suggestions.

I would like to thank Andritz Hydro Canada Inc. for their supports for the project. I also deeply appreciate members of R&D division: Mr. Vu, Mr. Nennemann for their excellent guidance and instructive comments during the research work.

The financial support of NSERC for this research is acknowledged.

A great thank you goes to my colleagues and teammates at Ecole Polytechnique for their valuable emotional and technical supports during the completion of the project.

Finally, I would like to thank with deepest gratitude to my father and mother who provided unconditional supports and encouragements throughout my life. I would also like to acknowledge my brother and sister for their supports.

RÉSUMÉ

Ces dernières années, plusieurs études se sont intéressées à l'amélioration de la conception des turbines hydroélectrique dans le but de réduire les effets négatifs des conditions d'opération hors design et des phénomènes transitoires. Néanmoins, encore plus d'efforts sont nécessaires pour fournir aux ingénieurs de conception des méthodes de simulation efficaces et robustes pour des conditions d'exploitation complexes et instationnaires. Il existe plusieurs approches concurrentes en cours de développement qui doivent être évaluées et comparées. Cette recherche vise à combler ce manque, en développant et en évaluant des méthodologies d'analyse des turbines Francis lors des opérations de rejet de charge, de vitesse à vide et d'emballement.

Cette recherche évalue des techniques de calcul de la vitesse d'emballement et de la vitesse à vide en utilisant des simulations numériques stationnaires et instationnaires. Deux méthodes sont comparées en calculant des paramètres dynamiques de la turbine pour trois cas composés de turbines Francis de haute et moyenne chute. Les simulations en stationnaire sont faites en utilisant un résoluteur fluide commercial, couplé avec un algorithme itératif basé sur la relation entre le couple de la roue et la vitesse. Toutes les simulations stationnaires sont faites sur un seul passage du distributeur et de la roue, connectés avec un modèle d'interface de mélange. Pour la seconde méthode, les simulations instationnaires, utilisant la moyenne de Reynolds des équations de Navier-Stokes (RANS), sont couplées à une sous-routine maison qui calcule et retourne le pas de temps, la vitesse de rotation de la roue et le couple de frottement. Les simulations instationnaires sont effectuées sur deux configurations géométriques: une turbine complète et sur un seul passage du distributeur et de la roue. Le modèle de rotor-stator transitoire (TRS) est utilisé pour coupler le distributeur avec la roue, et la roue avec l'aspirateur, dans le cas de la turbine complète. Un modèle d'interface de mélange est utilisé coupler un passage du distributeur avec un passage de la roue, et un passage de la roue avec l'aspirateur. Les simulations instationnaires avec le modèle TRS sont plus précises que les simulations stationnaires et instationnaires avec le modèle d'interface de mélange, pour calculer la vitesse d'emballement et la vitesse à vide pour plusieurs angles d'ouverture. Les simulations stationnaires fournissent un compromis entre la précision et l'effort de calcul nécessaire pour calculer les vitesses d'emballement et à vide.

Dans la deuxième partie du projet, les simulations instationnaires sont utilisées avec succès pour étudier le fonctionnement sans charge d'une turbine Francis. La simulation numérique d'un écoulement fluide est difficile parce que l'écoulement est irrégulier et instable à cause de la présence de décollements de l'écoulement, de formation de tourbillons, et d'oscillations de large amplitude de la pression dans la roue et l'aspirateur. Ces simulations permettent une meilleure compréhension de la physique de l'écoulement et des fluctuations de la pression dans la roue et l'aspirateur. On observe que les simulations instationnaires avec une interface de mélange ne sont pas capables de prédire les détails relatifs aux fluctuations du couple et de la pression durant les phénomènes transitoires. En outre, les résultats des simulations montrent une différence significative dans le calcul de la pression sur les pales entre les simulations instationnaires avec le modèle TRS et le modèle d'interface de mélange. Le principal défi des simulations instationnaires avec le modèle TRS est son très grand coût de calcul.

Enfin, l'objectif principal de cette thèse est atteint par l'élaboration et la validation d'une méthode basée sur la CFD pour prédire le comportement d'une turbine Francis dans le cas du rejet de charge. La méthodologie utilisée pour modéliser le rejet de charge est une extension de celle utilisée pour modéliser l'emballement et la vitesse à vide. Le principal défi de simulation provient de la rotation des directrices et est résolu avec la déformation de maillage et le remaillage. La variation de la vitesse de la roue est calculée en utilisant une équation du moment angulaire mis en œuvre dans une fonction définie par l'utilisateur. La méthodologie proposée a été élaborée en effectuant des simulations 2D instationnaires sur le modèle de turbine Francis de haute chute utilisé dans le workshop Francis-99, et validé par des simulations instationnaires 3D sur une turbine Francis de moyenne chute. Ces simulations permettent le calcul de paramètres d'ingénierie tels que la vitesse angulaire de la roue, la physique de l'écoulement et la charge sur les pales durant le rejet de charge. La validation des résultats numériques avec les résultats expérimentaux montrent un écart de 9% dans la prédiction de la vitesse maximale atteinte par la roue pendant le rejet de la charge. L'étude de l'écoulement relève la présence de structures complexes tels que le flux inversé, ou de pompage, à proximité du centre du diffuseur conique, et un flux tangentiel vers le bas près de la paroi du diffuseur conique. Des fluctuations de pression sont observées lorsque le point d'opération de la turbine Francis traverse les conditions de couple négatif. La méthodologie proposée présente une analyse qualitative de la physique de l'écoulement et du comportement de la turbine en cas de rejet de charge. Des mesures de la

pression sur la pale durant le rejet de charge sont calculées et validées. Une forte pression au bord d'attaque est prédite par les simulations numériques et est observée dans les résultats expérimentaux.

Pour conclure, les méthodologies proposées utilisant des simulations instationnaires de l'emballement, prédisent avec succès l'évolution des quantités d'ingénierie telles que la vitesse de rotation et le couple, ce qui peut contribuer au design de turbines dans ces conditions transitoires. En outre, une meilleure compréhension des phénomènes complexes à l'intérieur de la turbine est obtenue pour le rejet de charge et l'emballement.

ABSTRACT

In recent years, several studies have focused on improving hydroelectric turbine designs in order to decrease the negative influence of off-design conditions and transient processes. Nevertheless, greater effort is still needed to provide design engineers with efficient and robust simulation methodologies for complex unsteady operating condition. There are several competing approaches currently in development that must be evaluated and compared. This study aimed to reduce this gap in the research, by evaluating and developing methodologies for analyzing Francis turbine operations during load rejection, no-load condition, and runaway.

The research evaluated techniques for the calculation of the runaway speed, and no-load speed using steady and unsteady simulations. Two methods were compared by calculating turbine dynamic parameters for three test cases, consisting of high and medium head Francis turbines. The steady simulations were conducted using a commercial flow solver, and an iterative algorithm based on the relation between runner torque and speed. All steady simulations were performed on a single runner/distributor passage connected through a stage interface model. In the second method, unsteady RANS simulations were integrated with a user subroutine, to compute and return the value of the runner speed, the time step, and the friction torque. The unsteady simulations were performed for two geometric configurations: the complete turbine, and a single runner/distributor passage. The transient-rotor stator (TRS) model was used for connecting the runner and distributor, and the runner and draft tube in the complete turbine. The stage interface model was used for connecting the runner and distributor passages, and the runner's passage and draft tube. The unsteady simulations using TRS model were found more accurate than the steady and unsteady stage simulations for calculating the runaway and no-load speed for many opening angles. The steady simulations provided a compromise between accuracy and the computational effort required to calculate the runaway and no-load speed.

In the second part of the project, the unsteady simulations were successfully applied in order to investigate the operation of a Francis turbine at no-load conditions. Numerical flow simulation was challenging, because the flow was irregular and unstable owing to large flow separation, vortex formation, and large amplitude pressure oscillations in the turbine and draft tube. The simulations led to a deeper understanding of flow physics and pressure fluctuations in the turbine and draft tube. It was observed that the unsteady simulations with stage interface model were not

capable of predicting details pertaining to fluctuations of the torque and pressure during transient processes. Moreover, the simulation results showed the sizeable difference in computing the pressure on the blades between the unsteady simulations with TRS and stage interface models. The main challenge of unsteady simulations with the TRS model was dependency on more expensive computational costs.

Finally, the main objective of this thesis was achieved by developing and validating a methodology to predict the operation of a Francis turbine during load rejection, based on CFD simulations. The methodology for the runaway and no-load simulation was extended for modelling the load rejection. Mesh deformation and re-meshing techniques were used to address the simulation challenges caused by the guide vane rotation. The runner speed variation was computed using an angular momentum equation, implemented in a user defined function. The proposed methodology was developed by performing 2D unsteady simulations on a high head model Francis turbine used in the Francis-99 workshop, and validated by 3D unsteady simulations on a medium head Francis turbine. These simulations allowed the computing of the engineering quantities such as turbine angular speed, flow physics, and unsteady load on blades during the process. The validation of CFD results with experiments showed 9% discrepancy in the prediction of the maximum speed attained by turbine during the load rejection. The investigation of flow physics revealed the presence of complex flow structures such as reversed flow (pumping flow) near the draft tube cone center, and a downward tangential flow near the cone wall of the draft tube. Pressure fluctuations were captured when the Francis turbine's operating point moves through conditions of negative torque. The proposed methodology presented a qualitative analysis of the flow physics, and turbine behavior during load rejection. The pressure signals on the blade were evaluated, and validated during load rejection. Strong pressure signals were predicted at the leading edge for CFD and observed in the experiments.

To conclude, the proposed methodologies using unsteady simulations successfully predicted the evolution of engineering quantities such as the rotational speed and torque during the runaway process, which could contribute in designing turbine considering the transient behaviors. Moreover, the better insights of complex phenomena inside the turbine were obtained during load rejection and runaway processes.

TABLE OF CONTENTS

DEDICATION III

ACKNOWLEDGEMENTS IV

RÉSUMÉ V

ABSTRACT VIII

TABLE OF CONTENTS X

LIST OF TABLES XIV

LIST OF FIGURES XV

LIST OF SYMBOLS AND ABBREVIATIONS XX

CHAPTER 1 INTRODUCTION 1

1.1 Hydropower 1

1.2 Hydroelectric turbines operation 1

Francis Turbine 2

1.3 Present work 4

1.3.1 Problematic 4

1.3.2 Transient processes 5

1.3.3 Objectives 6

1.3.4 Structure of the Document 7

CHAPTER 2 LITERATURE REVIEW 8

2.1 One dimensional-hydro acoustic methods 8

2.1.1 Method of characteristics 9

2.1.2 Impedance method 10

2.1.3 Limitation of hydro acoustic methods 10

2.2 Experimental methods 10

2.2.1 Limitation of experimental methods 12
2.3 Computational fluid dynamics (CFD) 12
2.3.1 Limitation of Computational fluid dynamics 16
2.4 Summary 20
CHAPTER 3 ORGANIZATION OF THE WORK 21
CHAPTER 4 ARTICLE 1: COMPARISON OF STEADY AND UNSTEADY SIMULATION METHODOLOGIES FOR PREDICTING NO-LOAD SPEED IN FRANCIS TURBINES 23
4.1 Presentation of the article 23
4.2 Abstract 23
4.3 Introduction 24
4.4 Computational aspect 26
4.4.1 Geometry and mesh description 26
4.4.2 Numerical set-up 29
4.4.3 Methodologies 31
4.5 Results 37
4.5.1 Engineering parameters 37
4.5.2 Accuracy and convergence analysis of the steady-state algorithm 43
4.5.3 Convergence of the unsteady simulation algorithm 44
4.6 Conclusion 46
4.7 Acknowledgments 47
CHAPTER 5 ARTICLE 2: A NUMERICAL STUDY OF FRANCIS TURBINE OPERATION AT NO-LOAD CONDITION 48
5.1 Presentation of the article 48
5.2 Abstract 48

5.3 Introduction 49
5.4 Computational aspects 54
5.4.1 Studied cases 54
5.4.2 Numerical set up 60
5.4.3 Modeling rotor-stator interfaces 61
5.4.4 No-load simulation methodology 63
5.5 Results 66
5.5.1 Engineering parameters 66
5.5.2 Pressure 69
5.5.3 Flow physics of no-load condition for medium head TRS simulation 73
5.5.4 Comparison of flow physics inside the runner and draft tube between medium head TRS and stage simulations 76
5.6 Conclusion 81
CHAPTER 6 ARTICLE 3: UNSTEADY SIMULATION FOR FRANCIS TURBINE DURING LOAD REJECTION EVENTS 84
6.1 Presentation of the article 84
6.2 Abstract 85
6.3 Introduction 85
6.4 Computational aspect 88
6.4.1 Studied cases 88
6.4.2 Numerical set up 91
6.4.3 Load rejection simulation methodology 91
6.5 Results 95
6.5.1 Engineering parameters 95
6.5.2 Pressure 97

6.5.3 Flow physics during load rejection 102
6.6 Conclusion 104
6.7 Acknowledgments 105
CHAPTER 7 GENERAL DISCUSSION 106
7.1 Comparison between steady and unsteady simulations of Francis turbines at no-load condition 106
7.1.1 Engineering parameters: Speed factor and discharge factor 106
7.1.2 Computational cost 108
7.1.3 Evolution of turbine flow behavior 109
7.2 Friction torque computation 110
7.3 Load rejection simulation 111
7.3.1 Comparison between unsteady simulations of load rejection and no-load condition 112
7.3.2 Mesh quality during load rejection 115
7.4 Summary 117
CHAPTER 8 CONCLUSION AND RECOMMENDATIONS 118
8.1 Conclusion and contributions 118
8.2 Recommendations for future studies 120
BIBLIOGRAPHY 122

LIST OF TABLES

Table 2-1 Literature review of CFD simulations of hydraulic turbines during transient processes 17

Table 4-1: Test case specifications.....27

Table 4-2: Number of nodes for simulation domains. 27

Table 4-3 : Maximum discrepancy between the numerical and experimental speed factors.....38

Table 4-4 : Maximum variation of dimensionless parameters near the N_{ed}-axis. 44

Table 5-1 : Turbine geometry and mesh specifications used in no-load simulations 56

Table 5-2 : Average Y+ for simulation domains.....61

Table 5-3 : Maximum discrepancy between the numerical and experimental speed factors N_{ed} and discharge factors Q_{ed} at no-load condition 69

Table 5-4 : Comparison of normalized averaged pressure fluctuations in BEP and no-load condition for medium head-TRS & stage simulations at gva 16°.(PS: blade pressure side, SS: blade suction side) 70

Table 5-5 : Comparison of averaged and maximum pressure at no-load between medium head-TRS & stage simulations for a gva 16°. 80

Table 6-1: Turbine specifications at load rejection simulations. 90

Table 7-1 : Comparison of typical no-load simulations of a high head Francis turbine launched on a high performance computer (HPC) platform. 109

LIST OF FIGURES

Figure 1-1: Schematic diagram of a hydroelectric power plant 1

Figure 1-2: Operation areas of hydro turbines(Wagner et al., 2011) 3

Figure 1-3: Cross-section view of a Francis turbine installation (Round, 2004) 3

Figure 1-4: Side view of a typical Francis turbine layout (Round, 2004) 4

Figure 4-1: Mesh for components for test case 1: (a) distributor passage, stay vane and guide vane, (b) runner passage, (c) draft tube. 28

Figure 4-2: Geometry and boundary conditions of computational domains (test case 1). 29

Figure 4-3 : Speed factor N_{ed} & discharge factor Q_{ed} vs. wicket gate angles (WG) from CFD and experiments at no-load speed. 39

Figure 4-4: No-load speed line computed from CFD and experiments. 40

Figure 4-5 : Normalized axial velocity field, velocity vectors and streamlines on a section plane crossing the draft tube in steady (left) and unsteady (right) simulations at wicket gate angle of 15 degrees case 2 41

Figure 4-6 : Comparison time-averaged normalized velocity field and 2D streamlines between steady (left) and unsteady (right) simulations at wicket gate angle of 15 degrees at 1% span case 2 42

Figure 4-7 : Comparison time-averaged normalized velocity field and 2D streamlines between steady (left) and unsteady (right) simulations at wicket gate angle of 15 degrees at 50% span case 2 42

Figure 4-8 : Power factor P_{ed} vs. speed factor Ned for test case 2 in steady simulations. 44

Figure 4-9 : Speed factor N_{ed} vs dimensionless accumulated time step t^* by steady and unsteady methods 45

Figure 4-10 : Speed factor N_{ed} vs dimensionless accumulated time step t^* by unsteady method .. 46

Figure 5-1 : Mesh for Francis turbine & distributor (left), computational domain of complete turbine in medium head-TRS simulation (right). 55

Figure 5-2 : Mesh for components in medium head-stage simulation: (a) distributor passage, stay vane and guide vane, (b) runner passage, (c) draft tube. 55

Figure 5-3 : Mesh quality histograms (a) Element volume (log value) distribution, (b) Minimum angle distribution,(c) Expansion factor distribution 58

Figure 5-4 : Comparison of simulated and experimental discharge factor N_{ed} at no-load condition for different mesh densities. 59

Figure 5-5 : Comparison of simulated and experimental discharge factor Q_{ed} at no-load condition for different mesh densities 59

Figure 5-6 : Distribution of Y^+ at no-load on medium head Francis turbine components (gva 16°) 62

Figure 5-7 : Geometry and boundary conditions of computational domains in medium head-stage simulation. 63

Figure 5-8 : Variation of the normalized runner angular speed, flow rate, torque in medium head-TRS & stage simulations for a gva 16° 67

Figure 5-9 : Comparison between CFD predictions and experimental measurements (ANDRITZ Hydro, 2014) of speed coefficients Ned at no-load conditions (E=Error bar) 68

Figure 5-10 : Comparison between CFD predictions and experimental measurements (ANDRITZ Hydro, 2014) of flow coefficients Qed at no-load conditions (E= Error bar) 69

Figure 5-11 : Monitoring points on pressure (PS) and suction (SS) sides of blade in medium head-TRS & stage simulations 70

Figure 5-12 : Time history of normalized pressure fluctuation at PS and SS in medium head-TRS & stage simulations for a gva 16° 71

Figure 5-13 : Spectral analysis of normalized pressure fluctuations at SS & PS at no-load from medium head-TRS & stage simulations for a gva 16° 72

Figure 5-14 : Normalized time-averaged pressure distribution on the blade pressure (left) and suction (right) sides at BEP (top) and no-load (bottom) from medium head-TRS simulation for a gva 16° 73

Figure 5-15 : 3D Streamlines of normalized time-averaged velocity within runner at no-load in medium head-TRS simulation for a gva 16° 74

Figure 5-16 : Normalized time-averaged axial vorticity at 1% span (left) and 50% span (right) runner at no-load from medium head-TRS simulation for a gva 16° 75

Figure 5-17 : Normalized time-averaged velocity streamlines & vorticity magnitude at mid surface in blade channel at no-load condition from medium head-TRS simulation for a gva 16°. 75

Figure 5-18 : Normalized time-averaged tangential velocity (left) and axial velocity field (right) on a plane section through the draft tube at no-load from medium head-TRS simulation for a gva 16° 76

Figure 5-19 : Comparison of time-average pressure coefficient C_p at no-load from medium head-TRS & stage simulations for a gva 16° at different spans 77

Figure 5-20 : Comparison of normalized time-averaged velocity field and 2D velocity streamlines at no-load condition between medium head-TRS (left) and medium head-stage (right) simulations for a gva 16° on the plane z/L = -0.4 crossing the runner 78

Figure 5-21 : Comparison of normalized time-averaged pressure distribution on the blade suction side at no-load condition between medium head-TRS (left) and medium head-stage (right) simulations for a gva 16° 79

Figure 5-22 : Comparison of normalized time-averaged pressure distribution on the blade pressure side at no-load condition between medium head-TRS (left) and medium head-stage (right) simulations for a gva 16° 79

Figure 5-23 : Comparison of normalized time-averaged velocity field and 2D velocity streamlines at no-load condition between medium head-TRS (left) and medium head-stage (right) simulations for a gva 16° at a plane crossing the draft tube 81

Figure 6-1: Computational domain of high head model Francis turbine (Francis-99) in 2D unsteady simulations. 89

Figure 6-2: Geometry and boundary conditions of computational domains in 3D-medium head simulation. 89

Figure 6-3 : Wicket gate closing scenario for 3D medium head Francis simulations. 92

Figure 6-4 : Schematic illustration of the wicket gate closing simulation 93

Figure 6-5 : Mesh motion conditions of the wicket gate passage 94

Figure 6-6 : Variation of the normalized runner angular speed in 3D medium head simulations and experiment. 96

Figure 6-7 : Variation of the normalized runner torque and flow rate during load rejection in 3D medium head simulation. 96

Figure 6-8: Monitoring points on pressure (PS) and suction (SS) sides of blade in medium head-TRS & stage simulations. 97

Figure 6-9: Time history of normalized pressure at monitoring points on the pressure side. 98

Figure 6-10: Time history of normalized pressure at monitoring points on the suction side. 98

Figure 6-11: Spectral analysis of normalized pressure fluctuation at monitoring points on the pressure side (f_n: frequency of runner rotation at best efficiency operating point). 100

Figure 6-12: Spectral analysis of normalized pressure fluctuation at monitoring points on the suction side (f_n: frequency of runner rotation at best efficiency operating point).....100

Figure 6-13: Evolution of normalized pressure distribution on the blade pressure (left) and suction (right) sides during load rejection from 3D medium head simulation.....101

Figure 6-14 : Evolution of normalized swirl at draft tube inlet during load rejection simulation. 102

Figure 6-15: Normalized tangential velocity field on a cross section through the draft tube during load-rejection from 3D medium head simulation. 103

Figure 6-16: Normalized axial velocity field on a cross section through the draft tube at no-load from 3D medium head simulation. 103

Figure 7-1: Evolution of dimensionless speed and torque during no-load simulation of a medium head Francis turbine at gva 16º. 110

Figure 7-2 : Evolution of friction and turbine torque at the end of the runaway simulation for the medium head Francis turbine. 111

Figure 7-3 : Time history of normalized pressure fluctuation in medium head-Francis turbine during load-rejection (left) and at no-load condition (right). 113

Figure 7-4 : Evolution of the runner's speed during load rejection and no-load simulations at the medium head turbine. 114

LIST OF SYMBOLS AND ABBREVIATIONS

BEP	Best efficiency operating point
C_m	Torque coefficient ($= 0.0311\left(\frac{1}{Re_1^{0.2}}\right)\left(\frac{r_{hub}}{GAP_C}\right)^{0.1}$)
C_n	torque coefficient ($= 0.065(\frac{Gap}{\bar{r}_{shroud}})^{0.3}(Re)^{-0.2}$)
C_P	pressure coefficient ($= \frac{P-Patm}{\frac{1}{2}\rho V_{bldt}^2}$)
$C_{\varepsilon 1}$	constant number (*=1.44)*
$C_{\varepsilon 2}$	constant number *(=1.92)*
C_μ	constant number (*=0.09)*
D *or* D_h	turbine throat diameter, m
F	body force of unit mass fluid, N
E	hydraulic energy
f	frequency, Hz
f_n	turbine frequency at BEP, Hz
g	gravitational Acceleration, m/s^2
gva	*guide vane angle (degree)*
H	turbine net head, m
I_z	moment of inertia of the runner, kg m^2
K	turbulent kinetic energy ($= \frac{1}{2}\sqrt{\overline{u_i' u_i'}}$)
L	height of distributor passage, m
l_i	shroud seal length, m
n	iteration number

N	turbine rotational speed, rpm
N_{ed}	speed factor, Energy Units ($= \frac{ND}{60\sqrt{gH}}$)
P	pressure, N/m^2
P_{atm}	atmospheric pressure, Pa
$P_{ed,n}$	power factor at n iteration,
P_{ref}	reference pressure, Pa ($= \rho gH$)
$\overline{P_{ed\ ,n}}$	average of power factor at n-5 cycles
P^*	normalized pressure $(= P/P_{ref})$
Q	discharge, m^3/s
Q_{ed}	discharge factor ($= \frac{Q}{D^2\sqrt{gH}}$)
Q^*	normalized discharge (Q/Q$_{BEP}$)
r_{hub}	runner leading edge radius at the hub, m
$\bar{r}_{shroud}$	average shroud radius, m
Re	Reynolds number ($=\pi N D_h^2/60\,\nu$)
Re_1	Reynolds number ($= \frac{\omega \rho r_{hub}^2}{\mu}$)
Re_2	Couette Reynolds number ($= \frac{\rho \omega Gap \bar{r}_{shroud}}{\mu}$)
t	time, sec
$t_{Gap\ shroud}$	width of the runner shroud clearance, m
$t_{Gap\ hub}$	runner hub clearance, m
t^*	dimensionless accumulated time step
T *or* T_n	hydraulic force torque, Nm ($= T_r(t) - T_{fr}(t)$)
T^*	normalized turbine torque, Nm ($= T/T_{BEP}$)

T_{fr}	friction torques on turbine hub and shroud, Nm ($= T_{fr,hub} + T_{fr,shroud}$)
$T_{fr,hub}$	friction torques on hub, Nm ($= \frac{C_m \rho \omega^2 r_{hub}^5}{2}$)
$T_{fr,shroud}$	friction torque on shroud, Nm ($= \frac{C_n \rho \pi \omega^2 \bar{r}_{shroud}^4 \cdot l_i}{2}$)
T_g	torque of the electromagnet, Nm
T_r	torque of the pressure and viscous forces on runner blade, Nm
V	velocity, m/s
V_{bldt}	average flow velocity on blade draft tube interface, m/s
V_{ref}	reference velocity, m/s ($= \sqrt{gH}$)
V^*	normalized velocity $(= V/V_{ref})$
ρ	fluid density, kg/m^3
$\rho\overline{u_i' u_j'}$	Reynolds shear stress, N/m^2
δ_{ij}	Kronecker delta
σ_k	constant number (=1.0)
ω	runner angular speed, rad/sec
ω^*	normalized angular speed (ω/ω_{BEP})
σ_ε	constant number (=1.3)
μ_t	turbulent viscosity, N s/m^2
μ	dynamic viscosity of water, N s/m^2
wga	wicket gate angle (degree)

CHAPTER 1 INTRODUCTION

1.1 Hydropower

According to Renewables Global Status Report (GSR) (Ren, 2015), hydroelectric power provided an estimated 16.6% of the global electricity demand, and about 73% of the electricity from renewable sources. With virtually no output of greenhouse gas compared to fossil fuels, no direct waste and lower safety risk in comparison to nuclear power plants, hydroelectric power appears to be one of the most ecologically-friendly sources to meet the growing energy demand.

Hydroelectric power plants are composed of four main parts: the turbine, electric generator, transformer as well as upper and lower reservoirs. Figure 1-1 illustrates a schematic diagram of a hydroelectric power plant. Basically the flow passes through the penstock from the reservoir to reach the turbine which converts the energy in the water into mechanical power through a rotating shaft. Then the rotation of the shaft is converted into electric power by the electric generator. A series of rotating coils inside a magnetic field produces the electrical current. Finally the transformer increases the voltage of the electrical current before transmitting the power to the grid.

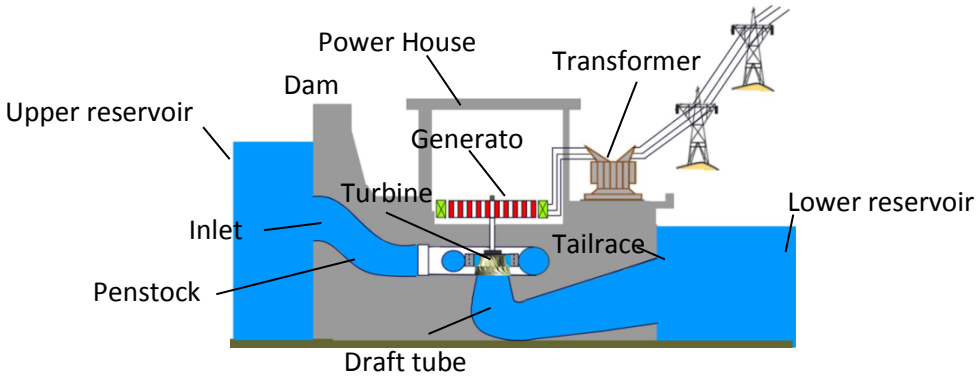

Figure 1-1: Schematic diagram of a hydroelectric power plant

1.2 Hydroelectric turbines operation

Hydroelectric turbines are synchronous machines, which implies that all the energy extracted from the water must immediately be consumed on the network. Therefore, the electric load on the generator must always balance the power mechanically extracted from the water. In case of slight

perturbations on the load, the turbine governor system will adjust the mass flow rate to compensate for the variations. However, in case of a complete drop or absence of load, the turbine cannot be suddenly stopped. Otherwise, the entire system may experience severe and extreme pressure fluctuations called water hammer, which may seriously damage and even destroy the turbine (Seleznev et al., 2014).

The turbine may be identified as the heart of the hydropower plants because of its role for developing torque from the dynamic action of water. This important part can be classified based on pressure change of water into two types: the impulse turbine, such as the Pelton turbine, which uses a high speed jet for converting kinetic energy of the fluid into revolving movement of the shaft while the pressure of the fluid doesn't change in this condition. The second type is called the reaction turbine, because the reaction of the fluid on the turbine blades produces the power through variation of velocity and pressure.

Two important types of reaction turbines are the Francis and the Kaplan. In the Kaplan turbine, the passing flow is in direction of axis of the rotation. But the flow inside a Francis turbine comes in the radial direction and leaves in the axial direction. Hence the Francis turbine is called as mixed flow turbine.

Additionally these types of turbines can be selected for different operation conditions (see Figure 1-2). Basically the Pelton turbine operates at low discharge and high head. The Francis turbine is appropriate for medium to high head and medium to high discharge, but Kaplan is limited to high discharge and low head. In this project, the Francis turbine operation is analyzed because the use of this type of turbine is the most prevalent for electrical power production.

Francis Turbine

Francis turbines are the most often selected hydroelectric turbines for electrical power production. They produce about sixty percent of the global hydroelectric power capacity, mostly because they can work efficiently under a wide range of operating conditions.

A Francis turbine comprises five main components: the spiral casing, stay vanes, guide vanes (wicket gates), runner and draft tube. Figure 1-3 shows a side view of a typical Francis turbine including the electric generator. Inside the spiral case; the axial flow is changed to radial flow. Then the guide vanes adjust the velocity and angle of the flow that reaches the runner in order to

control the power output (see Figure 1-4). The passing water rotates the runner about its axis. The rotational motion is converted to electric power through the runner shaft which is coupled with the generator. Finally, water flow passes in the draft tube to reach the lower reservoir. In this way, the draft tube acts as a diffuser to convert the residual energy of the flow into static pressure.

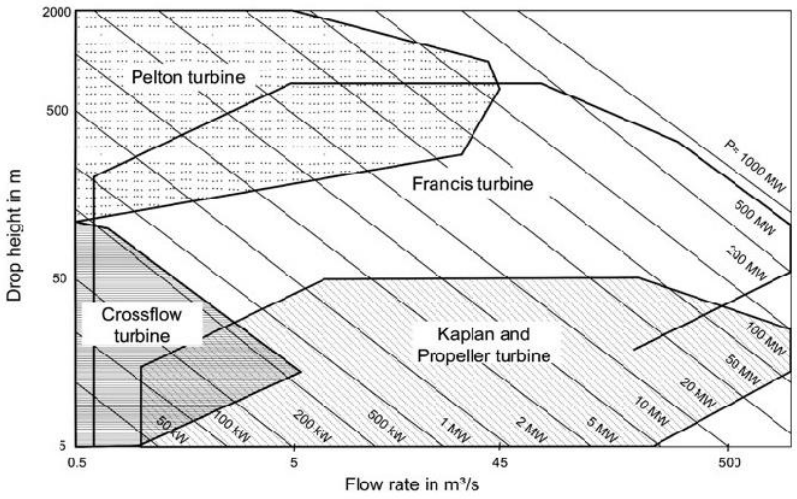

Figure 1-2: Operation areas of hydro turbines(Wagner et al., 2011)

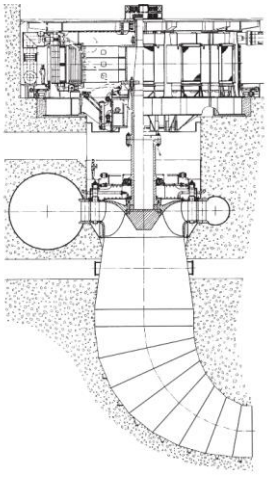

Figure 1-3: Cross-section view of a Francis turbine installation (Round, 2004)

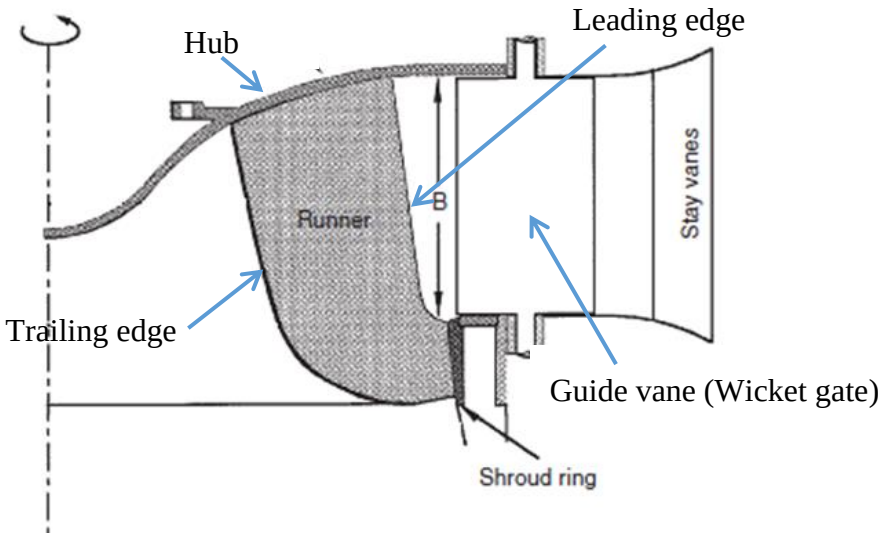

Figure 1-4: Side view of a typical Francis turbine layout (Round, 2004)

1.3 Present work

1.3.1 Problematic

Recently, the hydroelectric power plants have been deemed to play a new role as a flexible supplier of energy in the modern electrical grid because of the non-dispatchable production by renewables, such as wind and solar power (Dörfler et al., 2013). Under such circumstances, the hydroelectric power plants have to operate under off-design conditions, while they have traditionally been designed for a stable demand and continuously running conditions.

In addition, the new exploitation strategies often lead to more frequent transient processes due to sudden variations of the operating conditions such as machine shut-down or start-up and power variations. These transient processes may have a detrimental impact on the electrical grid (Dörfler et al., 2013; Nicolet, 2007). Irregular transient processes such as load rejection, no-load conditions and runaway (see below) may also occur. In hydroelectric power plants, the transient processes produce complex and time-dependent flow phenomena which induce pressure fluctuations and unsteady stresses on the structure. These conditions may influence the mechanical safety of hydraulic machines. In general, off-design operating conditions have a damaging effect on hydroelectric power plants such as shortening the runner's life, increasing cost of plant operation and losing power generation (Trivedi, 2014).

Several studies have focused on improving the turbomachinery designs so as to efficiently decrease the influence of off-design conditions and transient processes. Nevertheless, these investigations must be evaluated and compared to provide the hydroelectric power industry with efficient and robust methodologies for complex unsteady operating conditions.

1.3.2 Transient processes

Some harmful transient processes which may occur in hydroelectric power plants are presented in this section.

1.3.2.1 Speed no-load

Speed no-load condition typically happens when turbines are in standby mode for immediate connection to the grid. In this regard, the turbine operates at synchronous speed without electricity production. The speed no-load condition may happen over a long period (B. Nennemann et al., 2014).

1.3.2.2 No-load and Runaway

No-load condition is one of the most harmful transient processes. This process happens if the control system of the hydroelectric power plant fails to close the guide vanes when the generator is disconnected from the grid, and this failure leads to an instant rise of the runner's speed. The maximum speed attained by a runner is called runaway at full-gate opening and no-load speed at other guide vane angles. The value of runaway speed changes based on the turbine design, operation, and its setting. It may reach 150 to 350 % of its normal speed (Warnick, 1984).

1.3.2.3 Load Rejection

Load rejection occurs when the generator is disconnected from the network because grid parameters change beyond the generators prescribed range (Trivedi, 2014). In contrast to the runaway, during load rejection, the governor system of the turbine rapidly takes action to prevent the rotational speed from reaching an excessive value by closing the guide vanes. However, the rapid closing of the guide vanes may lead to pressure waves, which move forward and backward through the whole water passage. Consequently, it may lead to serious damage to hydroelectric power plants if not adequately managed.

1.3.3 Objectives

The main objective of this thesis is to develop and validate a methodology to predict the operation of a Francis turbine during load rejection based on the CFD simulations.

The main objective involves three specific objectives:

1. Developing a method based on the steady simulation for computing the runaway and no-load speeds(steady method)
2. Developing an approach for studying Francis turbine operation at runaway and no-load conditions using an unsteady simulation(unsteady method)
3. Developing the unsteady method for studying Francis turbine performance during load rejection by considering the movement of guide vanes.

The first objective of this thesis is to develop and validate a simple and fast method to calculate the runaway and no-load speeds using steady-state CFD simulations (steady method) based on the following essential phases:

- Development of an iterative algorithm that relies on a relation between turbine torque and speed coefficient
- Assessment of the steady method by computing no-load speed curves for the different Francis turbine cases
- Validation of the engineering quantities of the turbine computed by the steady method.

The second objective is to develop and validate an approach using an unsteady simulation (unsteady method) for studying Francis turbines at runaway and no-load conditions with fixed guide vanes according to the following steps:

- Development of an algorithm using an unsteady CFD simulation coupled with a user function which computes the runner acceleration based on the angular momentum equation
- Development of the unsteady CFD simulation by computing the dynamic time step, and the friction torque on the hub and shroud in addition to the turbine runner torque

- Systematic comparison between steady and unsteady simulations for computing the runaway and the no-load speeds of the Francis turbine
- Comprehensive analysis of the evolution of the engineering quantities, unsteady pressure and flow physics inside the turbine at runaway and no-load conditions computed by unsteady method
- Comparison between unsteady simulations of Francis turbines for two geometry configurations: a complete turbine and a single runner/distributor passage in order to determine the influence of interface models: transient rotor-stator (TRS) and stage on the accuracy and computational cost.

The third specific objective is to evolve the unsteady method that simulates the Francis turbine during load rejection based on the following steps:

- Development of an algorithm for modeling the guide vane movement using the mesh deformation and re-meshing techniques.
- Assessment of the proposed methodology by computing the unsteady pressure, flow physics and turbine engineering quantities during a load rejection process
- Validation of unsteady loads and runner speed computed by the load rejection simulations.

1.3.4 Structure of the Document

This thesis is organized in the following manner. In Chapter 2, previous studies regarding the investigation of hydroelectric turbines during transient processes are described. Indeed, Chapter 2 presents the methods applicable to analyze operation of hydroelectric turbines during load rejection, runaway and at no-load conditions. The scientific approach for the present research as well as the publication strategy is presented in Chapter 3. The three articles resulting from this project are included as Chapters 4 to 6. The connection between the articles is discussed in Chapter 7. Finally, the conclusion summarizes the main contributions of the thesis, and provides recommendation for future studies.

CHAPTER 2 LITERATURE REVIEW

In recent years, several attempts have been undertaken to study hydroelectric turbines in off-design conditions and during transient processes. The main objective of this chapter is to provide a comprehensive review of the state-of-the art in this field. In this regard, the limitation and strength of the proposed methods such as the hydro acoustic, experimental and computational fluid dynamic methods are explained. This survey is limited to reaction hydroelectric turbines especially Francis, Kaplan, Bulb, and reversible pump-turbines.

2.1 One dimensional-hydro acoustic methods

The hydro acoustic theory uses a mathematical model based on the one-dimensional hyperbolic equations of the elastic water hammer propagation in a pipeline to represent the dynamic behavior of hydropower plants (Nicolet, 2007):

$$\frac{\partial h}{\partial x}+\frac{1}{gA}\frac{\partial Q}{\partial t}+\frac{\lambda Q|Q|}{2gDA^2}=0 \tag{2-1}$$

$$\frac{\partial h}{\partial t}+\frac{a^2}{gA}\frac{\partial Q}{\partial x}=0 \tag{2-2}$$

with:

A : pipe cross-section [m^2];

a : wave speed [m/s].

D : pipe diameter [m];

g : gravitational acceleration [m/s^2];

Q: discharge [m^3/s];

h : piezometric head [m];

λ : friction coefficient.

The set of equations can be solved by various methods such as the method of characteristics, the transfer matrix method and the impedance method. The next sections describe two important

methods: the method of characteristics and the impedance method for simulating hydroturbines during transient processes.

2.1.1 Method of characteristics

In the method of characteristics, equations (2-1) and (2-2), which are related to the elastic water hammer propagation in a pipeline, are solved using a mathematical technique which is called the method of characteristics. This technique changes the governing partial differential equations to ordinary differential equations (Joukowsky, 1900; Streeter et al., 1993; Swaffield, 1993).

The method of characteristics, because of its simplicity and high performance, is commonly used for solving the water hammer equations during transient events such as a sudden valve closure or opening in a pipe and duct system, starting or stopping pumps, and so on. However, the method of characteristics cannot be applied for predicting 3D unsteady flows in hydraulic turbines, since it is a one-dimensional approach based on the inviscid hypothesis.

Afshar (Afshar et al., 2010) used the implicit method of characteristics (IMOC) to simulate transient flow in the penstock due to the power plant load rejection. In this manner, the variation of head and flow rate parameters were accurately predicted.

During transient operations in hydropower plants, dropping local pressure under the vapor pressure induces a water column separation phenomenon which could damage the turbine runner and non-rotating parts. Pejovic (Stanislav Pejovic, 2004) studied water column separation during load rejection in an underground hydroelectric power plant with long tailrace. Pressure measurements at the draft tube cone and 1-D transient numerical modeling based on the water hammer theory were used to analyze water column separation. The results displayed a huge pressure rise after a drop due to the collapse of the large void which was formed because of the pressure reducing below the vapor pressure in the draft tube. Therefore, it was suggested to consider a minimum submergence of the turbine installation as a function of the rotational speed in order to control the excessive pressure drop and subsequent pressure rise due to large void collapse.

2.1.2 Impedance method

The impedance method may be used for solving the hyperbolic system of equations for compressible mass flow and momentum conservation which describe the dynamic flow behavior in a hydroelectric power plant. In the method of impedance, the fluid fluctuation is analyzed using vibration and electrical transmission line theories (Streeter et al., 1993).

Nicolet (Nicolet, 2007) modeled the hydraulic components based on the impedance method in the SIMSEN software for modeling electrical power networks systems in transient or steady state mode, in order to simulate transient phenomena in Francis turbines. In this regard, three models: hydraulic, electric and hydroelectric were used for studying the transient behavior of a power plant with two Francis turbines. The simulation was performed for hydroelectric power plant transient conditions such as load rejection. During the simulation, parameters such as rotational speed, pressure, and discharge were analyzed. Finally, the simulation using the hydroelectric model was found more beneficial because it considers the strong interactions between the electric and hydraulic parts. In addition, results obtained from simulations were applied to test new control strategies.

2.1.3 Limitation of hydro acoustic methods

Generally, hydro acoustic methods are appropriate for predicting water hammer, which dominates in the dynamic behavior of the entire hydraulic circuit during transient processes. These methods offer compromise in terms of computational effort and accuracy. Nevertheless, hydro acoustic methods depend on experimental data such as the turbine hill-chart in order to define the hydraulic resistance and inductance needed in transient simulations. Furthermore, hydro acoustic methods are not capable of predicting unsteady 3D flow features such as vortices, cavitation, and recirculation inside a hydro turbine.

2.2 Experimental methods

In recent years, experimental methods have been applied for analyzing the performance of hydraulic turbines during transient processes and off-design conditions due to advancement of measuring instruments and techniques. For instance, the experimental data collected from different hydroelectric power plants was used to develop a theoretical model. The model showed

that increased start-stop cycles may reduce the predefined refurbishment time of power plants by up to 50 % (Sjelvgren, 1997). Experimental studies (Hasmatuchi et al., 2011) were performed in a reduced scale model of a pump-turbine in order to analyze the flow unsteadiness under runaway transient and low-flow conditions. These experiments revealed unsteady vortex formation and break down for the turbine brake mode. The vortex destruction led to asymmetric unsteady pressure pulsations and strong vibration. Furthermore, experiments showed that swirling flow developed at the runner inlet during closure of the guide vanes. This swirling flow caused more flow separation, instability in the runner blade passage, and asymmetric loading on the blades (Antonsen, 2007).

Transient pressure measurements were performed (Trivedi et al., 2015; Trivedi et al., 2014; Trivedi, Cervantes, et al., 2013; Trivedi, Gandhi, et al., 2013) in a high head model Francis turbine during start-up, shut-down, load variations, load rejections, and spin-no-load covering the entire range of the turbine operation. The pressure fluctuations, measured on model tests, were normalized with either the net head (H) or the specific hydraulic energy (E) in order to transfer from the model turbine to the prototype (Trivedi, 2014). Measurements from model tests showed that movement of guide vanes during load acceptance and rejection increase the pressure difference between the pressure and suction sides of the blade. The largest pressure variation occurred during the partial load rejection at the trailing edge of the blade (Trivedi et al., 2014).

Pressure measurements during spin-no-load showed that the instantaneous amplitude of unsteady loads was similar to that computed for the critical transient conditions such as load variation, start-stop, emergency shutdown, and total load rejection (Trivedi et al., 2015). (Trivedi et al., 2014) indicated that the maximum amplitudes of the unsteady pressure fluctuations in a high head model Francis turbine at runaway condition were 2.1 and 2.6 times that of the pressure loading at the best efficiency operating point in the vaneless space and runner, respectively.

The pressure fluctuations on the runner blade of a propeller turbine were measured during a runaway test (Houde et al., 2012). The post-processing of experimental data showed that the main source of pressure fluctuations in the runner is associated with instabilities in the draft tube flow.

2.2.1 Limitation of experimental methods

Transient measurements are usually performed on sites or in labs with prototypes and model test turbines, respectively. Although, there has been an advancement of new measuring instruments and techniques, the collection and application of experimental data has been partial during transient processes because of difficulties. For instance, the startup or total load rejection of a prototype turbine may be damaging and expensive due to the fact that it induces strong unsteady loads on the turbine during the transient process. For instance, one turbine start-stop cycle might shorten the predefined refurbishment period by15 hours (Nilsson, 1997).

Moreover, model testing is widely used for studying the flow field in hydroelectric turbines. However, it is required to scale up the experimental data in order to use in designing and manufacturing the prototype. Generally, the basic parameters such as head, discharge, power, and speed can be transferred from a model test to prototype using similarity laws. Nevertheless, the transformation of pressure fluctuations may result in large scaling errors. For instance, a scaling error of 20-50% was reported over the extended turbine operating range (Alligné et al., 2010; Dorfler, 2009; Ida, 1989).

2.3 Computational fluid dynamics (CFD)

Over the past decade, increase in the computational capacity and advancements in numerical techniques have allowed to simulate hydraulic turbines during transient processes using CFD. Nevertheless, the numerical simulation of hydraulic turbines at off-design conditions and near no-load operation is challenging because the flow physics are complex and dominated by vortex formation in all parts of the turbine as well as backflow zones (Dörfler et al., 2013).

Table 2-1 summarizes the characteristics of the most relevant CFD simulations carried out for hydraulic turbines in different transient processes. The majority of these studies solve unsteady viscous flow in order to predict time-dependent phenomena. The steady-state simulations of a Francis turbine were performed to compute the pressure loading on the runner blades, hub and shroud hydraulic surfaces (Melot et al., 2014). Validation of simulation results with experimental measurements showed good agreement for strain calculations.

In addition, Table 2-1 shows that the time-averaged turbulence models such as the two equations $k-\varepsilon$ and $k-\omega$ are generally used in these simulations. These models require substantially less

computational effort than sophisticated turbulence models such as the Reynolds stress model or filtering methods such as Large eddy simulation (LES).

The modelling of the variation in turbine speed is necessary during transient processes such as load rejection, start-stop and emergency shutdown. Most studies in Table 2-1 computed the runner acceleration or deceleration using angular momentum equations as follows, through a user function which is coupled with a CFD solver:

$$\dot{\omega} = \frac{d\omega}{dt} = \frac{T}{I} \tag{2-3}.$$

where *T* denotes the total torque on the main turbine axis acting on the runner, and I is the mass moment of inertia of rotating components. The torque may be computed from a CFD solver by hydraulic forces including pressure and shear forces acting on runner blades and hub surfaces. After a discretization, the runner angular speed is computed as follows:

$$\omega_n = \omega_{n-1} + \frac{T\Delta t}{I} \tag{2-4}.$$

where index *n* indicates the time step number in the unsteady simulation.

Experimental data was used to set the runner speed during some of the processes. For instance, (Fortin et al., 2014) updated the runner rotational speed based on the measurements during a runaway simulation of a model propeller turbine. These simulations showed that the numerical torque decreased more slowly than the actual torque in experiments. In addition, the amplitude of pressure fluctuations was underestimated in CFD simulations.

Furthermore, Table 2-1 indicates the computational domains used in each study, which generally consists of the complete distributor (stay vanes and guide vanes), complete runner and draft tube, despite the high computational effort. In addition, a transient rotor-stator interface model (TRS) was frequently used for matching stationary and rotating parts.

(Nicolle et al., 2012) evaluated various numerical setups for modeling a low head Francis turbine during a startup process, as shown in Table 2-1. A transient rotor-stator interface model was applied in all simulations. The unsteady simulations showed that a configuration including one runner and distributor channel may predict the main turbine physics such as runner speed

variation during runner acceleration. In addition, considering the draft tube in simulations improved the results by allowing for better pressure recovery. Finally, the simulation with complete turbine allowed for capturing rotating stall in the vaneless space at the speed no-load regime.

The flow behavior in a Francis turbine during load rejection was investigated using the hypothesis of “frozen” hydraulic conditions (Côté et al., 2014). The unsteady RANS equations were solved on the fixed boundary conditions related to a specific operating condition on the runaway hill chart. The frozen rotor stator ("ANSYS CFX-User manual,") was used for matching rotating and stationary parts so that they each have a fixed relative position during the calculation. The analysis of flow revealed a downward tangential flow near the band and draft tube cone wall, and strong pumping flow near the draft tube cone center. Interaction of the inlet and reversed flow in the runner resulted in very unsteady flow patterns which induced dynamic loads.

In load rejection simulations, the modelling of the movement of guide vanes is a challenging task. Generally, after each blade movements, the internal hydrodynamic mesh must be adjusted to the newly computed boundary nodes. Large displacement during transient processes degrade the mesh quality significantly (Casartelli et al., 2014). Therefore, developing a robust and efficient mesh deformation technique is necessary.

In order to simulate the opening of guide vanes, a user defined function was applied (Nicolle et al., 2012), which updated the mesh around the guide vane at each time step based on a prescribed motion. (J. T. Liu et al., 2012) simulated guide vane shutoff of a prototype pump-turbine during a load-rejection process using a dynamic mesh method. However, the dynamic mesh method details were not explained in this paper. The simulations predicted that a vortex rope appears inside the draft tube before reaching the turbine zero-torque condition.

(Casartelli et al., 2014) investigated unstable characteristics which caused oscillations in the reversible pump-turbines at no-load and in the turbine brake operation. The unsteady RANS equations were solved using the OPEN FOAM toolbox. The movement of the guide vanes was simulated by an explicit mesh deformation technique, based on Inverse Distance Weighting (IDW) interpolation of the boundary node movement to the interior of the flow domain. The proposed mesh motion method was time-efficient and memory-efficient (Witteveen et al., 2009).

The simulations predicted a complex flow inside the computational domain, including strong tangential flow at the guide vane outlet, and reversed flow at the hub and shroud of the runner.

(Y. Li et al., 2015) applied an active dynamic mesh technique in order to simulate the opening and closing of guide vanes in a Bulb hydraulic turbine in start transition process and load rejection. The technique was based on the simple concept of regenerating the mesh for each time step during large displacements. However, the method introduced inevitable interpolation errors during the simulation that caused an increase of the computational cost. The load rejection simulation depicted reflux in the runner entrance, a vortex phenomenon at the guide vanes and the draft tube, which caused significant swing and vibration of the Bulb turbine.

The emergency shutdown process of a ring gate was investigated numerically in a low head Francis turbine (Xiao et al., 2012). The unsteady RANS equations with the $k-\varepsilon$ RNG turbulence models were solved on the full flow passage of the Francis hydraulic turbine. Dynamic meshes and sliding meshes were used to simulate the movement of the ring gate. Moreover, the numerical analysis included the study of air and liquid multiphase flows in the flow passage using a mixture model. The analysis of results showed that the ring gate experiences a certain overturning torque due to a difference in pressure distribution between inner and outer surfaces. The turbine group vibration and uniform flow field in the guide vanes are observed at the end of closing.

Table 2-1 shows that many studies focused on the analysis of reversible pump-turbines for conditions around the no-load condition (Casartelli et al., 2014; Widmer et al., 2011). In these studies, the main goal was to investigate and predict the characteristic instability in the S-shaped region of the characteristic curve and as well the radial force imbalance on the machine caused by rotating stall.

In addition, Table 2-1 shows that the runaway transient in Francis turbines was studied by (Cherny et al., 2010; Jinwei LI et al., 2009; J Li et al., 2010). These investigations depicted the reversed flow in the runner and the vortex rope in the draft tube, which induces pressure fluctuations. The evolution of engineering quantities computed (Jinwei Li et al., 2007) showed that the runner speed increased by 58% and flow rate decreased by 14% at runaway.

2.3.1 Limitation of Computational fluid dynamics

As mentioned in the previous section, CFD simulations of hydraulic turbines during transient processes and off-design conditions are very challenging due to complex flow structures consisting of irregular backflows and vortices. Simulations must be time-dependent with high grid resolution in order to provide realistic flow prediction. Therefore, the CFD simulations depend on high computational effort (Dörfler et al., 2013). In addition, (Magnan et al., 2014) indicated challenges for assessing the grid sensitivity of hydroelectric turbine CFD simulations. Grid independence analysis for complex, detached flows involved many challenges among which: making refined meshes and comparing with experiments.

Besides, the complex flow structures lead to large stochastic pulsations of the flow, pressure, and guide vane torque. Thus, the assessment of unsteady flow is difficult due to wide-band fluctuations in CFD simulations of transient processes (Dörfler, Sick *et al.*, 2013). For instance, (B Nennemann et al., 2014) showed that turbulence model and numerical dissipation have a significant influence for predicting dynamic loads on the runner at no-load conditions.

In addition, the validation of unsteady CFD simulations of the flow close to no-load condition is partial because the measurements of unsteady pressure distribution in the runner and draft tube are very hard and expensive to obtain (Dörfler et al., 2013).

Table 2-1 Literature review of CFD simulations of hydraulic turbines during transient processes

Author	Turbine type	Transient process	Computational domain	Mesh (Mil)	Code	Analysis type	Interface model	Turbulence model	Runner speed variation
(Kolšek et al., 2006)	Bulb turbine	Shutdown	Full distributor, runner, draft tube	--	ICCM	Unsteady	--	Standard $k-\varepsilon$	Angular momentum
(Jinwei Li et al., 2007)	Francis Turbine	Runaway	Full spiral casing , distributor, runner, draft tube	--	--	Unsteady	TRS	RNG $k-\varepsilon$	Angular momentum
(Li, Yu *et al.*, 2010)	Francis Turbine	Load rejection	Penstock, full spiral casing , distributor, runner, draft tube	3.4	Fluent	Unsteady	TRS	RNG $k-\varepsilon$	Angular momentum
	Model Francis turbine	Runaway	Full spiral casing , distributor, runner, draft tube	2.4	Fluent	Unsteady	TRS	RNG $k-\varepsilon$	Angular momentum
(Cherny et al., 2010)	Francis	Runaway	One distributor channel, runner channel and draft tube	0.45	--	Unsteady	Periodic-stage	Standard $k-\varepsilon$	Angular momentum
(S. Liu et al., 2010)	Model Kaplan turbine	Runaway	Casing, distributor, and runner passages and draft tube	1.777	Fluent	Unsteady	Sliding mesh	RNG $k-\varepsilon$	Angular momentum
(Widmer et al., 2011)	Prototype pump-turbine	Brake operation	Full spiral casing , distributor, runner, draft tube	5	CFX	Unsteady	TRS	Standard SST model	Constant

Table 2-1: Literature review of CFD simulations of hydraulic turbines during transient processes “cont’d”

Author	Turbine type	Transient process	Computational domain	Mesh (Mil)	Code	Analysis type	Interface model	Turbulence model	Runner speed variation
(J. T. Liu et al., 2012)	Prototype pump-turbine	Load rejection	Full spiral casing , distributor, runner, draft tube	5	CFX	Unsteady	TRS	RANS v2-f	Angular momentum
(Yan et al., 2012)	Model pump-turbine	Runaway	Full spiral casing , distributor, runner, draft tube	7.7	CFX	Unsteady	TRS	Standard $k-\varepsilon$	Constant
(Huang et al., 2012)	Francis	Load-rejection	Casing, distributor, and runner passages and draft tube	2.19	Fluent	Unsteady	Sliding	RNG $k-\varepsilon$	Angular momentum
(Nicolle et al., 2012)	Francis	Startup	One channel distributor, runner, DRA, DRA360, DRAS 360	0.36	CFX	Unsteady	TRS	Standard $k-\varepsilon$	Angular momentum
			One channel distributor, runner, draft tube	0.63	CFX	Unsteady	TRS	Standard $k-\varepsilon$	Angular momentum
			360 distributor , runner, draft tube	6.49	CFX	Unsteady	TRS	Standard $k-\varepsilon$	Angular momentum
			360 spiral casing, distributor, runner, draft tube	14.4	CFX	Unsteady	TRS	Standard $k-\varepsilon$	Angular momentum

Table 2-1: Literature review of CFD simulations of hydraulic turbines during transient processes "cont'd"

Author	Turbine type	Transient process	Computational domain	Mesh (Mil)	Code	Analysis type	Interface model	Turbulence model	Runner speed variation
(Casartelli et al., 2014)	Pump-turbine	Speed-no load	Full spiral casing , distributor, runner, draft tube	--	Open FOAM	Unsteady	TRS	$k-\omega$ SST	Constant
(B. Nennemann et al., 2014)	Francis	No-load condition	1st setup: full distributor, runner, draft tube	5	CFX	Unsteady	TRS	$k-\varepsilon$ & SAS	Constant
(Melot et al., 2014)	Francis	Speed-no-load	Casing, distributor, and runner passages and draft tube	--	CFX	steady	stage	Standard $k-\varepsilon$	--
(Côté et al., 2014)	Francis	Load-rejection	1/24 distributor and full runner, draft tube	--	CFX	Unsteady	Frozen-rotor-stator	--	--
(Fortin et al., 2014)	Model propeller turbine	Runaway	Full semi-spiral casing, distributor ,runner draft tube	7	CFX	Unsteady	TRS	Standard $k-\varepsilon$	Experimental data

2.4 Summary

Transient simulation of runaway, no-load conditions and load rejection events in hydraulic turbines is a very active field of the research, where great efforts are still required to provide design engineers with efficient and robust simulation methodologies. There are several competing approaches under development that must be evaluated and compared. Based on the previous literature review, it appears that thorough validation of steady and unsteady CFD simulation approaches for runaway, no load condition and load rejection evens is still required. This constitutes the research topic covered in the present thesis.

CHAPTER 3 ORGANIZATION OF THE WORK

In this chapter, the contents of three articles, presented in this thesis, are briefly described. These articles are the scientific contributions of this thesis in order to reach the aforementioned objectives.

The first article, presented in Chapter four, is entitled “Comparison of steady and unsteady simulation methodologies for predicting no-load speed in Francis turbines”. This article, published in International Journal of Fluid Machinery and Systems, compares two numerical simulation approaches: steady and unsteady methods for studying the dynamic parameters of the Francis turbine during runaway and no-load conditions at fixed guide vane angles. In this regard, the article focuses on the calculation of the runaway speed and no-load speed of the Francis turbine in a wide range of guide vane angles. In a runner design process, the accurate determination of these turbine speeds is important to ensure the safe operation of the hydroelectric power plant.

The second article presented in Chapter five, entitled “A numerical study of the Francis turbine operation at no-load condition”, was submitted to the ASME Journal of Fluid engineering. This article focuses on analyzing the Francis turbine operation at no-load conditions using the unsteady method, developed in the first article. In this regard, unsteady RANS simulations are performed on two types of Francis turbines, medium and high head with two geometry configurations including a complete turbine, and a single runner/distributor passage connected through a stage interface model. The complete turbine contains the full distributor, runner and draft tube. In addition, the transient rotor-stator interface model is applied for connecting rotating and stationary components. The single runner/distributor passage simulations use a similar setup as for the unsteady simulations of the first article. The evolution of engineering quantities such as runner torque, angular speed, and inlet flow rate are investigated at no-load condition. The unsteady pressure loads and average pressure are computed on runner blades. Furthermore, the simulations reveal the details of flow physics in the runner and draft tube that dissipate the input energy into the turbine, and yield a near zero-torque at no-load condition. The main outcome of this paper is the comparison of simulations performed using transient rotor-stator (TRS) and stage interface models.

The third article, presented in Chapter six, is entitled “Unsteady Simulation for Francis turbine during load rejection events”. This manuscript was published in the proceeding of the ASME 2016 fluids engineering division summer meeting. The work develops an automated methodology for simulating Francis turbine operation during transient processes induced by load rejection occurring in an emergency shutdown. Two main challenges are addressed by the proposed methodology including the guide vane movement and runner speed variation. The simulation of the guide vane movement is difficult, due to the large displacement during transient process. This challenge has been solved by combining mesh deformation and re-meshing techniques. Similar to the unsteady method in the first article, the angular momentum equation is used to simulate the runner’s acceleration process. The proposed methodology is developed using 2D simulations and validated using 3D cases for a medium head Francis turbine during an emergency shutdown scenario. These simulations allow to evaluate successfully the engineering quantities such as the turbine angular speed, flow physics and unsteady loads on blades during the shutdown. Furthermore, the unsteady loads on runner blades are investigated in order to assess the behavior of the turbine in the transient conditions.

In Chapter seven, the overall discussion of the articles is presented followed by conclusion and future works.

CHAPTER 4 ARTICLE 1: COMPARISON OF STEADY AND UNSTEADY SIMULATION METHODOLOGIES FOR PREDICTING NO-LOAD SPEED IN FRANCIS TURBINES

Hossein Hosseinimanesh[1], Christophe Devals[2], Bernd Nennemann[3] and François Guibault[2]

[1]Department of Mechanical Engineering, École Polytechnique de Montréal

CP 6079, succ. Centre-ville, Montréal, QC, H3C 3A7, Canada, hossein.hosseinimanesh@polymtl.ca

[2]Department of Computer Engineering, École Polytechnique de Montréal

CP 6079, succ. Centre-ville, Montréal, QC, H3C 3A7, Canada, christophe.devals@polymtl.ca, francois.guibault@polymtl.ca

[3]Andritz Hydro Canada Inc.

6100 Transcanadienne, Pointe-Claire, QC, H9R 1B9, Canada, bernd.nennemann@andritz.com

4.1 Presentation of the article

In this chapter, two methodologies were developed and compared using the steady and unsteady simulations for calculating the no-load speed of Francis turbines, an important parameter that quantifies the turbine behavior at no-load condition. The methodologies were validated on a medium head and two high head Francis turbines. The article was published in International Journal of Fluid Machinery and Systems on July 18th, 2015 as:

Hosseinimanesh, H., Devals, C., Nennemann, B., and Guibault, F., 2015, "Comparison of steady and unsteady simulation methodologies for predicting no-load speed in Francis turbines," International Journal of Fluid Machinery and Systems, 8(3), pp. 155-168.

4.2 Abstract

No-load speed is an important performance factor for the safe operation of hydropower systems. In turbine design, the manufacturers must conduct several model tests to calculate the accurate value of no-load speed for the complete range of operating conditions, which are expensive and

time-consuming. The present study presents steady and unsteady methods for calculating no-load speed of a Francis turbine. The steady simulations are implemented using a commercial flow solver and an iterative algorithm that relies on a smooth relation between turbine torque and speed factor. The unsteady method uses an unsteady RANS simulation that has been integrated with a user subroutine to compute and return the value of runner speed, time step and friction torque. The main goal of this research is to evaluate and compare the two methods by calculating turbine dynamic parameters for three test cases consisting of high and medium head Francis turbines. Overall, the numerical results agreed well with experimental data. The unsteady method provided more accurate results in the opening angle range from 20 to 26 degrees. Nevertheless, the steady results showed more consistency than unsteady results for the three different test cases at different operating conditions.

4.3 Introduction

Hydropower manufacturers must guarantee the performance of the turbine runner at the end of the design process. Hence tests are performed on homologous models to demonstrate the guaranteed values of dynamic parameters such as the efficiency, cavitation, stability, runaway, and hydraulic axial thrust for the complete range of operating conditions. Among these parameters, runaway speed and no-load speed have an essential role in ensuring the safety of a power plant.

No-load speed is the maximum speed attained during no-load operation of a turbine-generator at maximum head. It is also called runaway speed at full gate opening. No-load and runaway conditions happen when the control system fails to close rapidly the vanes during a load rejection event, and this failure may lead to dangerous situations. The runner speed rises while there is no generator-load to dissipate the runner kinetic energy. Under such circumstances, slim structures such as turbine blades may be deformed due to increased centrifugal and hydraulic forces. Consequently, the rotor may become unbalanced and produce vibration, which can lead to failure of the entire turbine. Although the runaway and no-load conditions occur far from the turbine design operating condition, they constitute plausible events during an emergency situation such as a fault of the control system during emergency shutdown. Thus the accurate prediction of runaway speed and no-load speed at different wicket gate angles is necessary to ensure the structural integrity of turbine components and the safety of the hydropower plant.

An accurate value of no-load speed is usually obtained from model tests, which are performed by the turbine manufacturers. Experimental tests are expensive and time-consuming. Thus it is desirable to develop alternative numerical methods for computing no-load speed of prototype turbines. For this purpose, hydro acoustic models are fast and robust, and allow simulating the dynamic behaviour of the complete hydropower plant. Nicolet (Nicolet et al., 2004) used a 1D hydro acoustic method for modelling the hydraulic components of a hydropower plant in both transient and steady modes. The model could show the evolution of turbine dynamic parameters such as angular speed, pressure and discharge during a load rejection event. However, this method depends on experimental data. For instance it requires the turbine hill-chart to determine hydraulic resistance and inductance needed in transient simulations.

Over the past two decades, industrial computational fluid dynamics (CFD) has been applied for solving difficult engineering problems because of computational capacity increase and numerical techniques advancements. Vu (Thi C Vu et al., 2002) used steady-state stage computations for accurate prediction of efficiency characteristics of a Francis turbine near its best efficiency point. He also showed steady-state simulations to be a highly effective methodology for comparing global draft tube performance for nearby design operating points (Thi C. Vu, Devals, Zhang, Nennemann, Guibault, et al., 2011). Melot (Melot et al., 2014) performed steady-state stage simulations with RANS solver in order to compute the static stresses at speed no-load conditions. The computational domain included the casing, stay vane and runner passage and draft tube. The results were in good agreement with on-site strain gauge measurements. He concluded that the steady-state methodology is robust and flexible enough to be used in different projects under no-load condition during the design phase. Hosseinimanesh (Hosseinimanesh et al., 2014) used a methodology based on the steady-state RANS flow simulations in order to calculate no-load speed. The results showed good agreement with experiments.

In hydro turbines, unsteady CFD simulations have been used for analyzing highly turbulent flows at off-design conditions and transient processes. The results showed the existence of unsteady flow phenomena such as vortex break down, rotor-stator interaction and vortex shedding inside flow passage (Guo et al., 2009; Levchenya et al., 2010; Nennemann et al., 2005; A. Ruprecht et al., 2002). Kolšek (Kolšek et al., 2006) used unsteady flow simulations with the standard k-ε turbulence model to predict the angular speed, axial force and pressure at selected points during the shut-down of an axial water turbine. Nicolle (Nicolle et al., 2012) obtained the loading on the

blades in a 3D transient numerical simulation of a hydraulic turbine during the start-up phase. The unsteady simulations included wicket gate motion and angular speed variation algorithms. Cherny (Cherny et al., 2010) studied the transient behavior of Francis turbine during runaway using the unsteady stage simulations. He developed an approach, consisting of a one-dimensional water hammer calculation for the penstock and 3D unsteady periodic stage simulation for the turbine. The results showed that a periodic stage approach ignored the effects of the runner-stator interaction and damped the vortex rope in the draft tube. Li (J Li et al., 2010) simulated the no-load condition at 9 wicket gate angles for a Francis turbine with the RNG k-ε turbulence model. However, very little details were given about the results and numerical methods used. He reported the presence of intense swirling flow at the draft tube inlet, and secondary and transverse flows in the runner.

The present paper, which is an extension to the study presented at the 27th IAHR Symposium on Hydraulic Machinery and Systems (Hosseinimanesh et al., 2014), applies steady and unsteady RANS methodologies to accurately estimate turbine no-load speed and runaway in Francis turbines. The unsteady and steady methods are compared on three test cases over a range of operating conditions in order to introduce an efficient methodology. The numerical results are validated using data obtained during model test measurements carried out by Andritz Hydro.

4.4 Computational aspect

4.4.1 Geometry and mesh description

The numerical study is performed on three test cases that include medium and high head Francis turbines in order to evaluate the capability of the proposed methodology. The high head Francis turbine comprises 20 stay vanes and guide vanes, 15 runner blades and draft tube. The medium head Francis turbine consists of 20 stay vanes and guide vanes, 13 runner blades and draft tube. The computational domain for all test cases encompasses a distributor channel (one stay vane, one wicket gate), a runner passage (hub, shroud, blade) and the draft tube as can be seen in Figure 4-1 for test case 1. The summary of turbine characteristics is shown in Table 4-2. Test cases 2 and 3 consist of the same geometries for all components except the runner blade.

Table 4-1: Test case specifications

	Runner type	Blades	Wicket gates	Stay vanes
Case 1	Medium head Francis turbine	1/13	1/20	1/20
Case 2	High head Francis turbine	1/15	1/20	1/20
Case 3	High head Francis turbine	1/15	1/20	1/20

The geometries and meshes of the components were generated using Andritz design tools. Multi-block-structured meshes for runner channel and draft tube, and hybrid mesh in a single channel for the wicket gate and stay vane were used[1]. For example, Figure 4-1 shows the computational mesh for each component for test case 1. The complete computational domain of test cases 1, 2 and 3 comprised 554k, 811k, and 813k mesh nodes respectively, as detailed in Table 4-2.

Table 4-2: Number of nodes for simulation domains

	Stay vane & wicket gate	Runner blade	Draft tube	
Mesh type	Hexahedra and prisms	Hexahedra	Hexahedra	Total
Case 1	167k	144k	243k	554k
Case 2	170k	435k	206k	811k
Case 3	170k	437k	206k	813k

[1] In this thesis, the first and second papers focused on the simulation of Francis turbine at no-load condition. Moreover, several cases have been studied to improve mesh and time step sensitivity analyses, which are documented in the second paper.

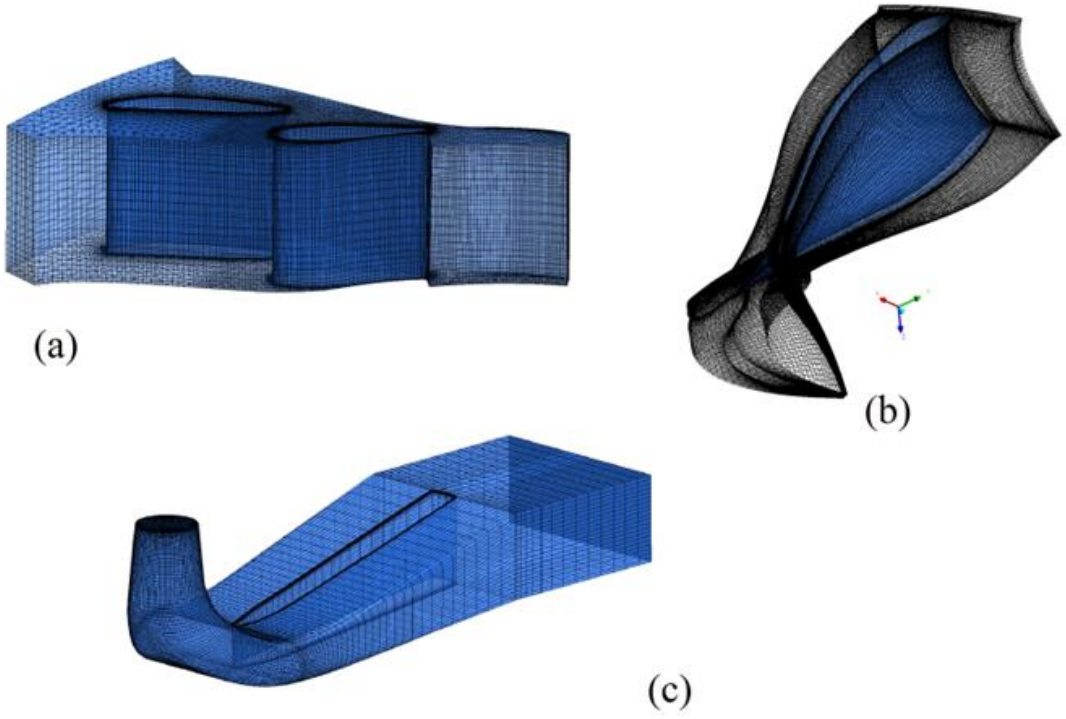

Figure 4-1: Mesh for components for test case 1: (a) distributor passage, stay vane and guide vane, (b) runner passage, (c) draft tube

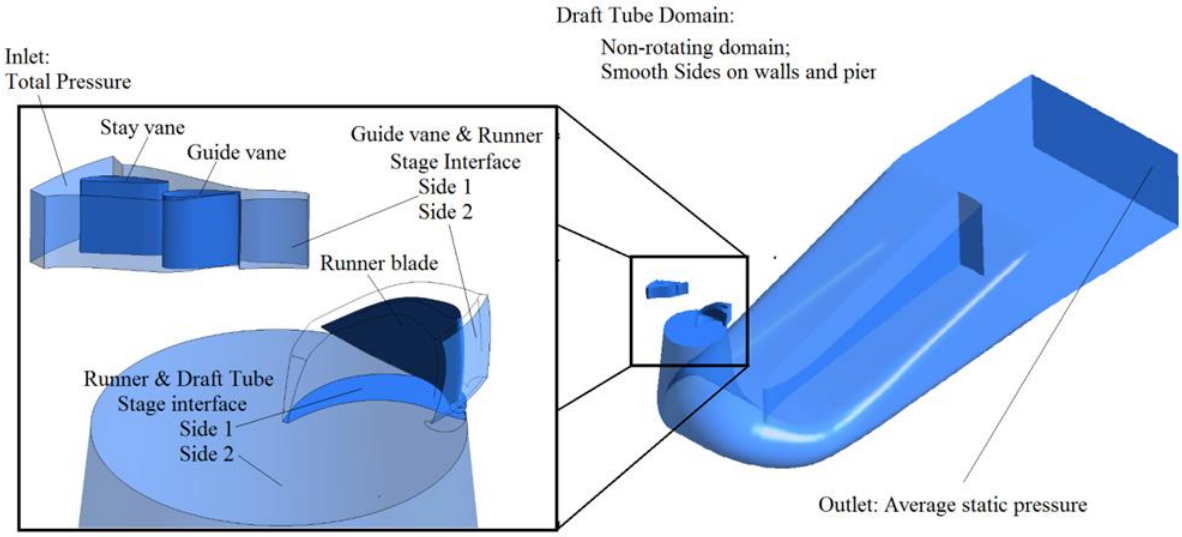

Figure 4-2[2]: Geometry and boundary conditions of computational domains (test case 1)

4.4.2 Numerical set-up

In the present study, the runaway speed is calculated by performing steady and unsteady Reynolds averaged Navier-Stokes 3D calculations at different operating conditions using Ansys-CFX 14 commercial solver. The Reynolds-averaged Navier-Stokes equations (RANS) are given by

$$\frac{\partial U_i}{\partial x_i} = 0 \tag{4-1}$$

$$\rho \frac{\partial U_i}{\partial t} + \rho \frac{\partial (U_j U_i)}{\partial x_j} = -\frac{\partial P}{\partial x_i} + f + \mu \left(\frac{\partial^2 U_i}{\partial x_j^2} \right) + \rho \frac{\partial}{\partial x_j} \overline{u_i' u_j'} \tag{4-2}$$

[2] Steady and unsteady simulations are performed in a single distributor, runner passage and complete turbine with boundary conditions, shown in Figure 4-2.

where U is time-average of velocity (m/s), ρ is the fluid density (kg/m^3), f is the body force per unit mass of fluid (N), μ is the dynamic viscosity of water (N.s/m^2), P is the average pressure (N/m^2), and $\rho\overline{u_i'u_j'}$ is the Reynolds shear stress (N/m^2), which can be written based on the Boussinesq hypothesis (Davidson, 2004) as:

$$\rho\overline{u_i'u_j'} = -\mu_t\left(\frac{\partial u_i}{\partial x_j}+\frac{\partial u_j}{\partial x_i}\right)+\frac{2}{3}\rho\delta_{ij}k \tag{4-3}$$

where $k=\frac{1}{2}\sqrt{\overline{u_i'u_i'}}$ is the turbulent kinetic energy, and δ_{ij} is the Kronecker delta, μ_t is the turbulent viscosity.

The standard k-ε turbulence model is applied for treating turbulence. The standard k-ε model is known as a reliable and robust turbulence model for simulating high Reynolds number flows in Francis turbines. Galvan's (Galvan S et al., 2011) investigation on the steady state swirling flow in a draft tube showed that the standard k-ε turbulence model demonstrates good balance between reliable performance and computational cost.

The standard k-ε model is based on two transport equations, one for turbulent kinetic energy k, and the other for the turbulent dissipation ε. The transport equations for turbulent kinetic energy, k, and its dissipation rate, ε, are written as:

$$\frac{\partial\rho k}{\partial t}+\frac{\partial(\rho U_j k)}{\partial x_j}=\frac{\partial}{\partial x_j}\left[\left(\mu+\frac{\mu_t}{\sigma_k}\right)\frac{\partial k}{\partial x_j}\right]+P_k-\rho\varepsilon \tag{4-4}$$

$$P_k=\rho\overline{u_i'u_j'}\frac{\partial\rho U_i}{\partial x_j} \tag{4-5}$$

$$\frac{\partial\rho\varepsilon}{\partial t}+\frac{\partial(\rho U_j\varepsilon)}{\partial x_j}=\frac{\partial}{\partial x_j}\left[\left(\mu+\frac{\mu_t}{\sigma_\varepsilon}\right)\frac{\partial\varepsilon}{\partial x_j}\right]+C_{\varepsilon1}P_k\frac{\varepsilon}{K}-\rho C_{\varepsilon2}\frac{\varepsilon^2}{K} \tag{4-6}$$

The standard k-ε model equations include the empirical constants σ_k=*1.0*, σ_ε=*1.3*,$C_{\varepsilon1}=1.44$, and $C_{\varepsilon2}$=*1.92*.

The turbulent viscosity is expressed by:

$$\mu_t = \rho C_\mu \frac{k^2}{\varepsilon} \tag{4-7}$$

where C_μ =0.09 is a constant number.

The momentum and turbulent advection equations have been discretized using the high-resolution scheme and first-order scheme, respectively. The steady stage simulations were performed using one distributor channel as a stationary component and a runner blade passage as a rotating component in order to improve the computation cost. A stage interface was used for connecting the runner and distributor channel, and also the runner and draft tube modeled in distinct frames of reference. Radial runner blade passage interfaces were connected through fully matching rotational periodicity model. The inlet boundary condition was set to the total pressure associated to the turbine net head[3]. The outlet boundary condition was specified as zero-averaged static pressure. No-slip boundary condition was imposed for all solid walls.

4.4.3 Methodologies

4.4.3.1 Steady state method

The steady state methodology is based on the hypothesis that the turbine torque is a smooth function of the speed factor. In order to find runaway and no-load speed, we have to find the zero of the function. A general pseudo-code of the proposed methodology is shown in Algorithm 4-1. The first step consists in generating meshes from parametric geometry descriptions of each component. Then the numerical set-up is implemented as described in the previous section for the selected wicket gate angle. In step 3, we initialize the simulations for two operating point speed factors[4], $N_{ed,1}$ and $N_{ed,2}$ with best efficiency point speed value and 1.3 times of the same value, respectively. Then steady stage computations are performed for those points. In step 5 the blade torques T_1, T_2, and power factor $P_{ed,2}$ are derived from the converged simulations. Then we initialize the loop control value to 2 and start to compute the no-load speed in an iterative way as follows.

---

[3] The inlet flow angle of 28° was set to the inlet boundary condition.

[4] For definition of N_{ed}, Q_{ed}, P_{ed}, see section 7.1.1.

At the beginning, when $n = 2$, there are only two known points, namely $(N_{ed,1}, T_1)$ and $(N_{ed,2}, T_2)$. If the two points have the same sign for the torque, we use the secant method that passes a line through two points, and takes where it intersects abscissa as next point. Otherwise, we use False position method (Wikipedia, 2016). If $n > 2$, there are many known points $(N_{ed,1}, T_1), \dots, (N_{ed,n}, T_n)$, which lead to more available methods to estimate $N_{ed,n+1}$ such that T_{n+1} would be equal to zero. The simplest method is to use the last two points $(N_{ed,n}, T_{n-1})$ and $(N_{ed,n}, T_n)$, and to compute $N_{ed,n+1}$ using again the secant method until two points of unlike torque sign are obtained. Afterward, the best choice is to use the false position method. This approach is proved to be efficient for calculating runaway speed.

Algorithm 4-1 : Steady state methodology algorithm for no-load speed computing

Input: Wicket gate angle Output: Runaway speed
1: Generate meshes
2: Numerical set-up
3: Initialize: Select speeds of two operating conditions $N_{ed,1}$, $N_{ed,2}$
4: Perform steady simulation for these two selected operating conditions
5: Compute torques T_1 , T_2, power factor $P_{ed,2}$ from steady simulation results
6: Set $n = 2$
7: While Iteration not converged do Steps 7.1-7.4
7.1: From previous points $(N_{ed,n}, T_n)$, $(N_{ed,n-1}, T_{n-1}), \dots$, compute the next operating condition at $N_{ed,n+1}$
7.2: Perform steady simulation at $N_{ed,n+1}$
7.3: Derive torque $T_{n+1}$and power coefficient $P_{ed,n+1}$
7.4: Set $n = n + 1$
8: $N_{ed,\ no-load} = N_{ed,n}$

In order to do fewer iterations of the main loop in algorithm 1, and to do fewer numerical simulations with Ansys CFX, some attempts were done to use more than the last two points, for example, by using a linear regression through the last three or four points or quadratic fitting of the last three points. These more complex approaches have not shown any significant advantage over the simple 2 point method.

The process is considered to have converged, and $N_{ed,n}$ is considered as the no-load speed if one of the following conditions is satisfied.

- $\frac{|N_{ed,n} - N_{ed,n-1}|}{N_{ed,n-1}} < 2\ \%$ for the two last points with different torque sign.
- The value of power factor $|P^*_{ed,n}|$ is less than 0.01.

Otherwise, we iterate, and compute the next operating condition, or stop if the loop control value n reaches the maximum value. Moreover, at each steady state simulation, the convergence tolerances of all main primitive variables were set to 10E-5 on the root mean square (RMS) residuals. Besides, the quantities of torque and inflow were tracked during simulation at monitoring points. Whenever their averaged values became steady, the simulation was considered to have converged.

4.4.3.2 Unsteady method

In this method, an unsteady simulation is carried out at specific operating points until the turbine reaches the no-load condition. For unsteady simulation, the operating points are calculated using the angular momentum equation for the rotating mass as follows:

$$T - T_g = I_z \frac{d\omega}{dt} \tag{4-8}$$

Here T denotes the torque of turbine hydraulic force (Nm), T_g is the torque of the electromagnet or payload torque (Nm), I_z is the moment of inertia of the runner (kgm^2), and ω is the runner angular speed (rad/s). When a load rejection event occurs within a hydropower plant, the electromagnetic torque instantaneously drops to zero ($T_g = 0$), and the angular speed of the runner starts to rise monotonically. However, the rate of increase in angular speed eventually decreases because of hydraulic losses in the hydraulic system. Finally, the turbine angular speed reaches a maximum value, called the no-load speed. Under such circumstances, the runner moment tends to zero because of the balance between hydraulic and drag forces acting on the turbine.

Algorithm 4-2 presents the unsteady methodology for estimating the runaway and no-load speed in Francis turbines. The steps from 1 to 4 are similar to the steady state methodology. We similarly generate meshes and implement the numerical set-up, but perform the steady stage simulation only at the speed factor of the best efficiency point $N_{ed,1}$. In step 5 the blade torque T_1

is derived from the converged simulations. Then we initialize the loop control value to 2 and start to perform an unsteady stage simulation during which the operating points $N_{ed,n}$, are updated by

$$\omega_n = \omega_{n-1} + \frac{T_n \Delta t}{I_z} \tag{4-9}$$

Equation (4-9) is derived from Eq. (4-8) by a first order explicit discretization. In Eq.(4-9), Δt represents a time step (s) that is adjusted automatically by Eq. (4-10) based on the runner angular speed variation during no-load simulations:

$$\Delta t = \frac{M}{\omega \cdot a} \tag{4-10}$$

where ω (rad/s) is the runner angular speed, a=57.2958 deg/rad is a constant number. Furthermore, M =4° is a constant number corresponding to the angular variation in degrees at each time step.

Algorithm 4-2 : Unsteady state methodology algorithm for no-load speed computing

Input: Wicket gate angle Output: Runaway speed, inlet flow rate, pressure magnitude on the blade
1: Generate meshes
2: Numerical set-up
3: Select speed of an operating conditions $N_{ed,1}$
4: Perform steady simulation for the selected operating condition
5: Compute torque T_1, from steady simulation results
6: Set $n = 2$
7: While Simulation not converged do Steps 7.1-7.4
7.1: From previous point $(N_{ed,n-1}, T_{n-1})$ compute the next operating condition at $N_{ed,n}$
7.2: Continue unsteady simulation at $N_{ed,n}$
7.3: Compute torque T_n and power factor $P_{ed,n}$
7.4: Set $n = n + 1$
8: $N_{ed,\ no-load} = N_{ed,n}$

All processes in Algorithm 4-2 are implemented using the commercial flow solver Ansys CFX. In simulations, the flow solver integrates a user subroutine written in Fortran 77 in order to compute and return the value of angular velocity, time step and friction torque.

For the unsteady computation to be considered converged at the no-load condition, the following conditions must be satisfied[5]:

- $\frac{|N_{ed,n} - N_{ed,n-1}|}{N_{ed,n-1}} < 2\ \%$
- $\left|\frac{\overline{P_{ed,n}}}{P_{ed,BEP}}\right| < 1\ \%$

Otherwise, we continue unsteady simulation for the next operating condition, or stop if the loop control value n reaches the maximum value.

4.4.3.3 Friction torque

In Eq. (4-8), the torque is calculated by

$$T = T_t(t) - T_{fr}(t) \tag{4-11}$$

where T_t, which is the turbine torque caused by pressure and viscous forces on the runner blade, is obtained from steady simulation results. The T_{fr} term, which is the friction torque on the turbine crown and band, is opposing the driving torque during no-load condition. The friction torque is calculated as follows:

$$T_{fr} = T_{fr,crown} + T_{fr,band}. \tag{4-12}$$

The friction torques $T_{fr,crown}$ and $T_{fr,band}$ have an impact on the crown and band sections, respectively. The friction torque impact on the crown surface is estimated using a model that was established based on the approximation of a smooth rotating disk in a housing with turbulent flow(Schlichting et al., 2000). The friction torque on the crown is estimated by

[5] For details of convergence criteria, see section 5.4.4.

$$T_{fr,crown} = \frac{C_m \rho \omega^2 r_{crown}^5}{2} \tag{4-13}$$

where ω is the runner angular velocity (rad/s), r_{crown} is the runner leading edge radius at the crown, ρ is the water density (kg/m^3), and C_m is the torque coefficient, defined as

$$C_m = 0.0311 \left(\frac{1}{Re^{0.2}}\right)\left(\frac{r_{crown}}{GAP_C}\right)^{0.1} \tag{4-14}$$

where GAP_C is the width of the runner crown clearance (m), and Re is the Reynolds number, which is equal to

$$Re = \frac{\omega \rho r_{crown}^2}{\mu} \tag{4-15}$$

In order to calculate the band torque, the band rotation was approximated by two concentric cylinders with the inner cylinder rotating with angular velocity ω, and the outer cylinder at rest. In the present work, Bilge's equation (Bilgen et al., 1973), which is an empirical relation of torque coefficient of coaxial cylinders, was applied for calculating the runner torque as follow:

$$T_{fr,band} = \frac{C_n \rho \pi \omega^2 \bar{r}_{band}^4 \cdot l_i}{2} \tag{4-16}$$

where l_i is the band seal length, and $\bar{r}_{band}$ is the average band radius. The moment coefficient for turbulent flow regimes with $Re > 10^4$ is defined as

$$C_n = 0.065\left(\frac{Gap}{\bar{r}_{band}}\right)^{0.3}(Re)^{-0.2} \tag{4-17}$$

where $Re = \frac{\rho \omega Gap \bar{r}_{band}}{\mu}$ is the Couette Reynolds number, Gap is the width of the runner band clearance, and $\bar{r}_{band}$ is the average radius of the band.

4.5 Results

4.5.1 Engineering parameters

The steady and unsteady approaches were applied on three test cases in order to assess the accuracy of the proposed methodologies. For each test case, we numerically calculated the dynamic parameters such as the speed factor N_{ed}, discharge factors $Q_{ed,}$ and power factor P_{ed}, defined by (IEC61364, 1999), at no-load condition for different opening angles. The numerical results were compared with experimental measurements.

Figure 4-3 (left) compares the experimental and numerical speed factors at no-load condition for different wicket gate angles. The unsteady approach led to more accurate estimates of the speed factor at wicket gate angles between 20 and 26 degrees. For instance, in case 2, the maximum discrepancies between CFD results and experiments were 3.42% and 3.95% in the unsteady and steady methods, respectively at the wicket angle of 26 degrees. Nevertheless, it is observed in Figure 4-3 that the steady method resulted in more accurate predictions at wicket gate angle of 15 degrees compared to unsteady. The maximum differences between numerical and experimental speed factors for all cases are shown in Table 4-3.

Furthermore, Figure 4-3 (right) shows the numerical and experimental results of the discharge factors at no-load condition. In Figure 4-3, for case 1, the steady and unsteady results agreed well with experimental data. In a similar manner to the speed factor results, the unsteady method generates more accurate discharge factors in the opening angle range from 20 to 26 degrees for cases 2 and 3(see Figure 4-3 right). For example, in case 2, the maximum discrepancies were 4.8% and 6% in the unsteady and steady methods for wicket angle of 26 degrees, respectively.

Figure 4-4 compares the no-load speed lines, which were computed from steady, unsteady and experimental methods. For all test cases, the no-load speed lines follow the same trend, but a little deviation is observed for higher speed factors. For case 1, the steady and unsteady lines are very close to each other. For case 2 and 3, the steady lines are closer to experiments.

The unsteady method was not as accurate as the steady method in its prediction for wicket gate angles below 20 degrees. In order to explain the prediction error for these angles, the flow physics, computed by the steady and unsteady simulations for one such operating condition, are analyzed and compared.

Figure 4-5 shows the distribution of normalized axial velocity, surface streamlines and velocity vectors in a plane section of the draft tube, computed through steady and unsteady simulations, at a wicket gate opening of 15 degrees for case 2. The same overall flow behavior is observed in the draft tube for both methods. In Figure 4-5, the turbine discharge enters near the draft tube cone wall. On the other hand, a mainly axial flow returns towards the runner in the cone center. Furthermore there is a flow moving towards the draft tube outlet. Comparison between simulations shows that the unsteady simulation calculated a backflow region with a higher velocity near the draft tube cone and an entering flow with a lower velocity near the cone wall compared to the steady simulation.

Table 4-3 : Maximum discrepancy between the numerical and experimental speed factors

Case	Wicket gate opening	Discrepancy	
		Steady state	Unsteady state
1	22°	5.65 %	5.99%
2	26°	3.95 %	3.42 %
3	26°	3.23 %	2.87 %

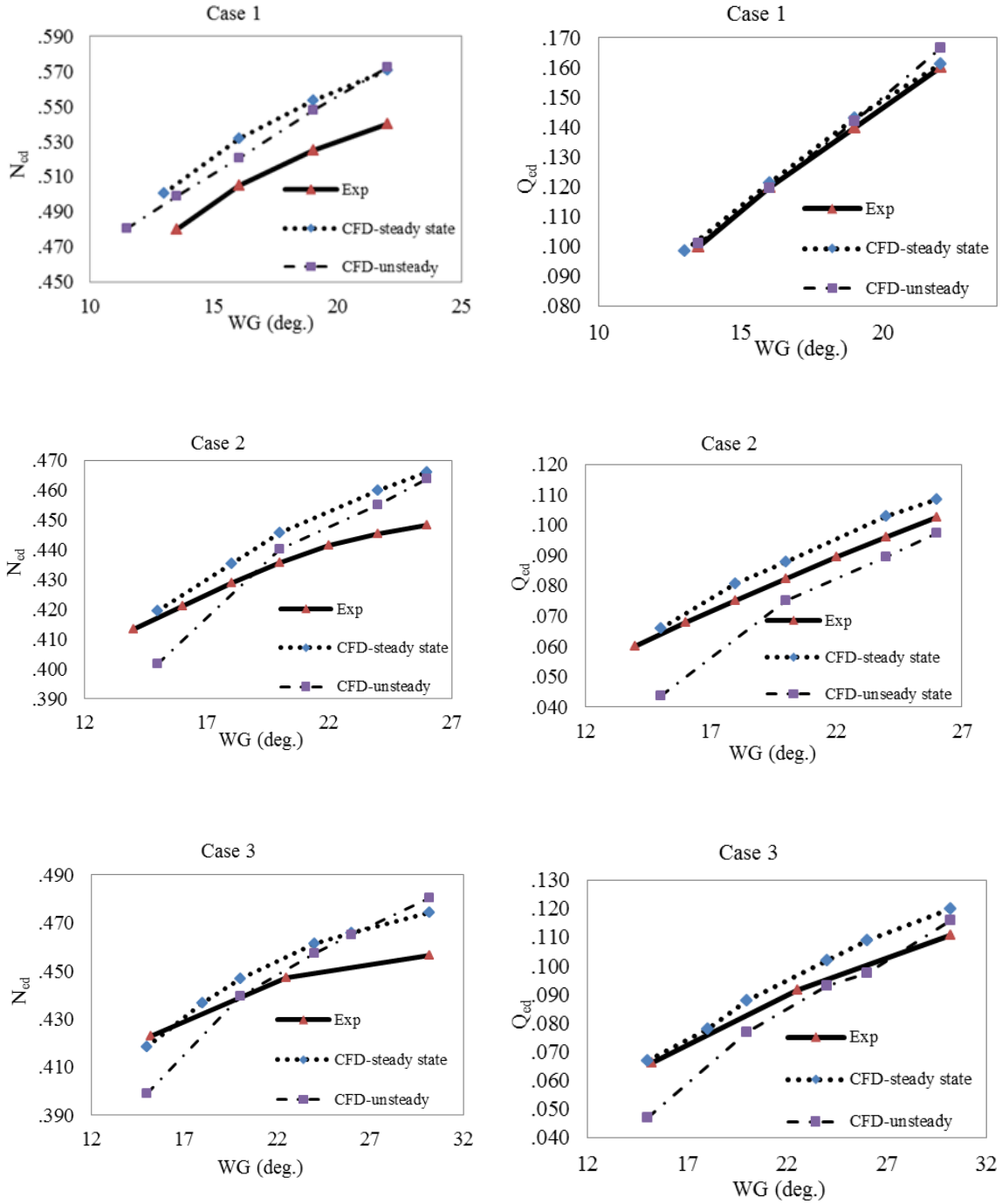

Figure 4-3 : Speed factor N_{ed} & discharge factor Q_{ed} vs. wicket gate angles (WG) from CFD and experiments at no-load speed

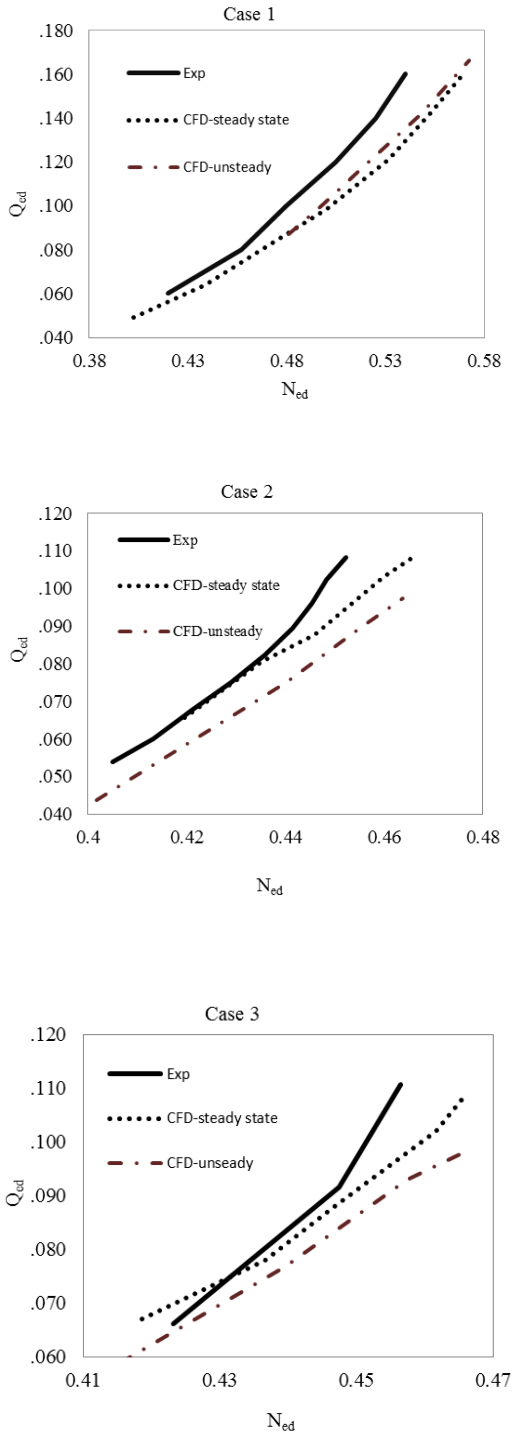

Figure 4-4: No-load speed line computed from CFD and experiments

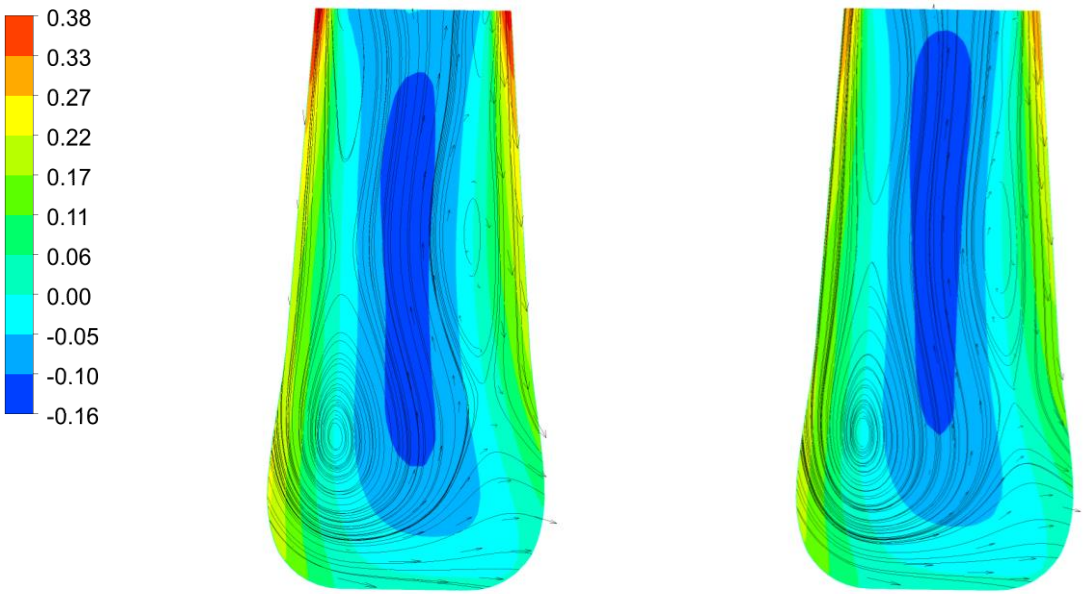

Figure 4-5 : Normalized axial velocity field, velocity vectors and streamlines on a section plane crossing the draft tube in steady (left) and unsteady (right) simulations at wicket gate angle of 15 degrees case 2

Figures 4-6 and 4-7 present the surface streamlines and the normalized velocity[6] contours, computed using steady and unsteady simulations, at 1 % and 50 % runner blade span, respectively for the same operating point. Figure 4-6 (left) shows that a high velocity flow passes the turbine passage at 1 % span in the steady simulation. On the other hand, the right part of Figure 4-6 shows that low velocity vortices have blocked a part of the turbine passage in the unsteady simulation. In Figure 4-7 both simulations calculated the same flow pattern at 50 % span. Figure 4-7 shows that strong axial vortices have blocked the largest part of the inlet runner passage.

[6] V^*: normalized velocity $(= V/\sqrt{gH})$.

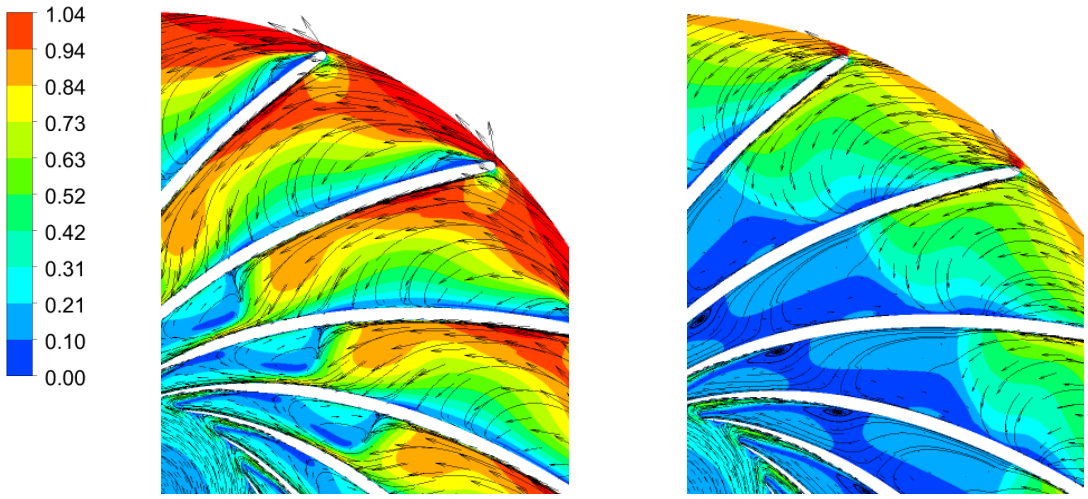

Figure 4-6 : Comparison time-averaged normalized velocity field and 2D streamlines between steady (left) and unsteady (right) simulations at wicket gate angle of 15 degrees at 1% span case 2

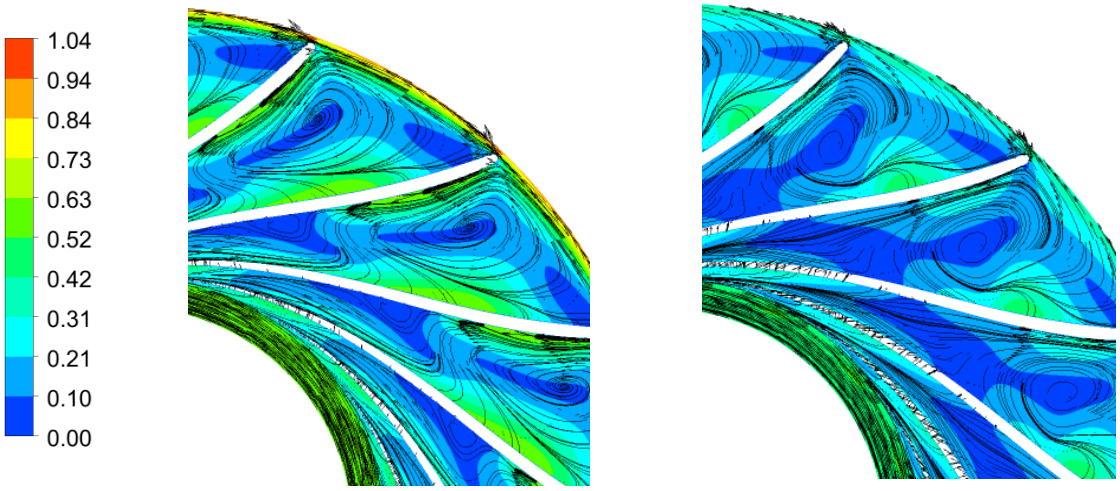

Figure 4-7 : Comparison time-averaged normalized velocity field and 2D streamlines between steady (left) and unsteady (right) simulations at wicket gate angle of 15 degrees at 50% span case 2

Overall, it can be noted that the unsteady simulation has over predicted the turbine blockage at 1 % span for a wicket gate opening angle of 15 degrees. This over prediction caused lower turbine discharge, and no-load speed compared to experimental and steady results. This over prediction may be caused by the presence of the stage averaging interface between the runner and draft-tube.

It is expected to obtain more accurate results by performing unsteady simulations in a fluid domain with a very fine meshes and smaller time steps and using a transient rotor-stator interface.

Generally, from the results, it appears that the no-load speed was well predicted through the proposed methodologies. Nevertheless, the engineering parameters, calculated by the steady method display more consistency than the unsteady results for the three different test cases at different operating conditions. Hence the steady method can be used as a reliable and precise tool for computing runaway and no-load speed in Francis turbines.

4.5.2 Accuracy and convergence analysis of the steady-state algorithm

In order to analyze the accuracy and convergence properties of the two proposed algorithms, the convergence behavior of the steady-state algorithm is further discussed. According to the proposed methodology, steady-state computations are performed at operating points that are selected based on the false position method. The computations are stopped when the turbine torque and efficiency become small enough. Figure 4-8 shows the evolution of the power factor P_{ed}, which corresponds to turbine torque and angular speed, for selected operating points. In Figure 4-8(left), the power factor decreases gradually when the speed factor increases in runaway speed computations. The points close to the Ned-axis are shown in Figure 4-8 (right). They show that when approaching runaway speed, a large drop of the power factor occurs for a small increase of the speed factor. For instance, the power factor decreases by 335% between E_1 and E_2, while the speed factor simultaneously increases only by 0.09%, as detailed in Table 4-4.

The sudden drop of the power factor near the horizontal axis illustrates the highly non-linear behavior of the flow near the no-load condition. This sharp deviation in the power factor reduces the capacity of the steady-state algorithm to precisely determine the speed coefficient at which torque becomes zero. This observation justifies the choice made in the present study, whereby results for the power factor are bounded within a range from -0.01 to 0.01 around zero, which was determined suitable for predicting the runaway speed with an adequate level of accuracy.

Table 4-4 : Maximum variation of dimensionless parameters near the N_{ed}-axis

Wicket gate opening	Points	N_{ed}	P_{ed}
15°	E_1-E_2	0.09 %	-335 %
18°	F_1-F_2	0.16 %	-193 %

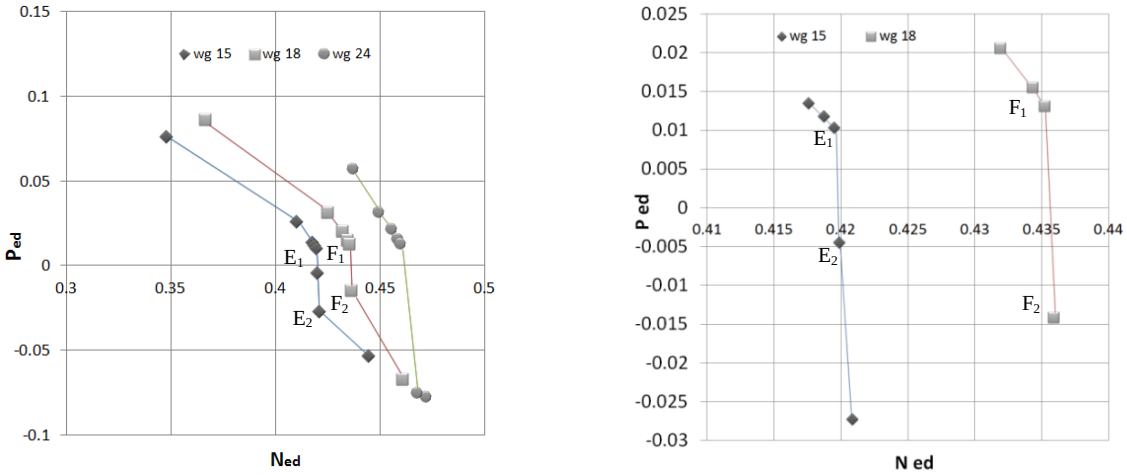

Figure 4-8 : Power factor P_{ed} vs. speed factor Ned for test case 2 in steady simulations

4.5.3 Convergence of the unsteady simulation algorithm

Contrary to the steady-state case, the algorithm used in the unsteady methodology does not require to accurately determine the condition for which torque becomes zero. The algorithm must, however, detect a stabilization of the speed factor. The flow behavior being highly unsteady, the level at which stabilization occurs may vary depending on the starting point of the simulation. To test the sensitivity of the unsteady solution to its starting point, two different simulations were performed with the different starting points on the second case at the opening angle of 15 degrees. The main goal was to evaluate the repeatability of the unsteady methodology. First unsteady

simulation started from a converged steady method solution, while the second unsteady simulation began from the best efficiency operating point.

Figure 4-9 shows the evolution of the speed factor during the first simulation. In Figure 4-9, the no-load speed was primarily calculated by steady method that started from point A (N_{ed} *=0.35*), and converged to point B (N_{ed}*=0.41*) through five steps. Afterward, an unsteady simulation started from point B, which finally converged to point C (N_{ed} *= 0.398*). The difference of 4.8 percent was found between speed factors calculated by steady and unsteady methods in Figure 4-9.

Figure 4-10 shows the evolution of speed factors during the second simulation. At the first step, a steady state simulation was performed at point D, the best efficiency operating point, in order to obtain an initial solution. After convergence of the steady simulation, the unsteady simulation is started from E with speed factor of best efficiency operating point. In Figure 4-10, the speed factor increased at the beginning of unsteady simulation due to load rejection. Eventually, it decreased and converged to point F (*Ned=0.399*). The discrepancy between speed factors in the first and second unsteady simulations was 0.25 %. This little discrepancy between unsteady simulations with different starting points shows that the applied unsteady methodology is fairly successful in reproducing the results.

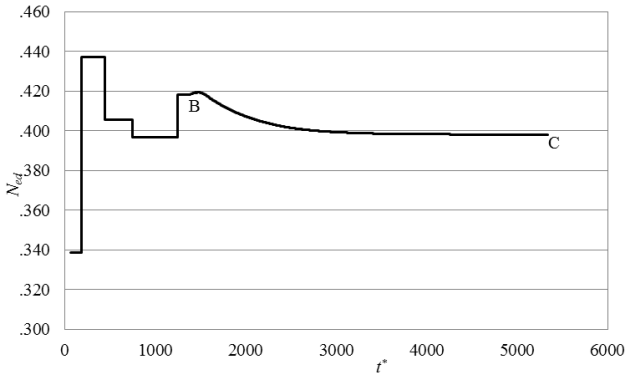

Figure 4-9 : Speed factor N_{ed} vs dimensionless accumulated time step t^* by steady and unsteady methods

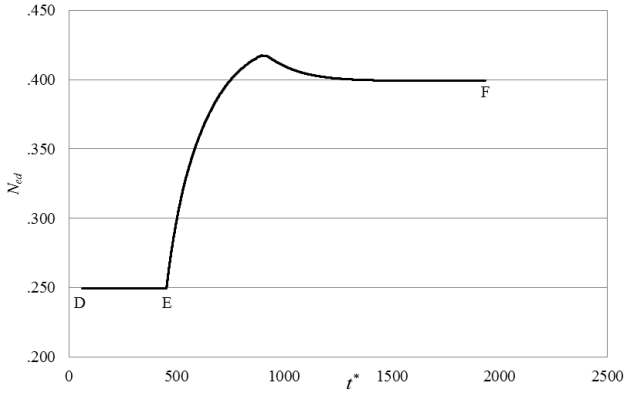

Figure 4-10 : Speed factor N_{ed} vs dimensionless accumulated time step t^* by unsteady method

4.6 Conclusion

In a runner design process, the accurate determination of runaway and no-load speed is important to ensure the safe operation of the hydropower plant. Hence this paper evaluated a steady and an unsteady method for computing the no-load speed of Francis turbine runners at different opening angles. The steady method was faster and simpler than the unsteady method because it used steady-state stage computations and a simple algorithm based on the smooth relation between torque and speed. The unsteady method relied on unsteady state computations in a CFD flow solver that integrated a user subroutine in order to retrieve the value of angular velocity during simulation. The unsteady simulations depended on significant computational effort to compute accurate values of runaway speed due to difficulties related to unsteady turbulent flow modelling and instabilities.

Two methods were assessed by calculating turbine dynamic parameters: speed factor, discharge factor and power factor during runaway speed for three test cases consisting of high and medium head Francis turbines. Overall, the numerical results agreed well with experimental data. The unsteady method provided more accurate results in the opening angle range from 20 to 26 degrees for all cases. However, the unsteady method was not successful for wicket gate angles lying outside this range. For instance, the study of flow simulation results showed that the unsteady

simulation over predicted the flow blockage in the turbine passage at a wicket gate opening angle of 15 degrees in case 2.

Furthermore, some parts of the error corresponded to the stage interface model, used for connecting the rotating and stationary parts in the steady and unsteady simulations. The stage interface model neglected some transient effects because of performing the circumferential averaging of the fluxes at the interface. A transient rotor-stator model, which simulates the relative motion between components on each side of the interfaces, may increase the no-load speed prediction accuracy.

Furthermore, in the present study very little discrepancy was found between unsteady simulations with different starting points for the same wicket gate angle in case 2. It showed the repeatability of the applied unsteady methodology in order to compute the no-load speed.

Generally, the steady results showed more consistency than unsteady results in the three different test cases at different operating conditions. In addition, there were difficulties related to the unsteady simulation convergence, which led to more expensive computational efforts compared to steady method. Hence the steady method can be applied by design engineers as a reliable tool in order to compute runaway speed in a wide range of operating conditions with an adequate level of accuracy.

4.7 Acknowledgments

The Authors are grateful to the ANDRITZ Hydro for technical support of the project, and would like to thank Dr. Julien Dompierre for providing his useful comments and valuable knowledge about the numerical analysis in this project.

CHAPTER 5 ARTICLE 2: A NUMERICAL STUDY OF FRANCIS TURBINE OPERATION AT NO-LOAD CONDITION

Hossein Hosseinimanesh[1], Christophe Devals[2], Bernd Nennemann[3], Marcelo Reggio[1] and François Guibault[2]

[1]Department of Mechanical Engineering, École Polytechnique de Montréal

CP 6079, succ. Centre-ville, Montréal, QC, H3C 3A7, Canada, hossein.hosseinimanesh@polymtl.ca

[2]Department of Computer Engineering, École Polytechnique de Montréal

CP 6079, succ. Centre-ville, Montréal, QC, H3C 3A7, Canada, christophe.devals@polymtl.ca, francois.guibault@polymtl.ca

[3]Andritz Hydro Canada Inc.

6100 Transcanadienne, Pointe-Claire, QC, H9R 1B9, Canada, bernd.nennemann@andritz.com

5.1 Presentation of the article

In the preceding chapters, the unsteady simulations of Francis turbine at no-load were performed for two geometric configurations: the complete turbine and a single runner/distributor passage using transient-rotor stator (TRS) and stage interface models, respectively. The unsteady simulations were compared in order to determine the influence of interface models on the accuracy of the results. The flow behavior inside Francis turbine at no load was investigated. This article has been submitted on October 2nd 2015 and the revised manuscript submitted March 23rd 2016 in revised form as:

Hosseinimanesh, H., Devals, C., Nennemann, B., Reggio, M., and Guibault, F., 2015, "A numerical study of Francis turbine operation at no-load condition," Journal of Fluids Engineering, under review.

5.2 Abstract

This paper presents a numerical methodology to study Francis turbines at no-load condition, an important operating condition regarding static and dynamic stresses. The proposed methodology uses unsteady Reynolds-averaged Navier–Stokes (RANS) simulations that have been integrated

with a user subroutine to compute and return the value of runner speed, time step and friction torque. The modelling tool is the commercial software Ansys-CFX 14. The main outcome of this research is the comparison of simulations performed using transient rotor-stator (TRS) and stage interface models and the validation of results through experiments over the full range of admissible guide vane angles. Both TRS and stage interface models yielded similar trends for all turbine runner parameters during the no-load process. Results show sizable differences in the average and maximum pressure on the blades between TRS and stage simulations. Analysis of the flow behavior in TRS simulation demonstrates complex flow phenomena involving a vortex breakdown within the draft tube, and strong vortices blocking the runner inlet, which dissipate the input energy into the turbine, and yield a near zero-torque at no-load condition.

5.3 Introduction

Intermittency of new energy sources such as solar and wind in the power generation mix are a cause of instability for traditional electrical grids. This has led to a rethinking of exploitation strategies of hydropower plants for stabilizing energy grids. In this regard, hydropower plants are deemed to generate energy in a more flexible manner, while they have traditionally been designed for a stable demand and continuously running conditions. Moreover, these plants are now subjected more frequently to transient processes, due to sudden variations on their operating conditions: machine shut-down or start-up, regime modification and even load rejection. These transient processes have a damaging effect on hydropower plants by shortening the runner's life, increasing cost of plant operation and inducing loss of power generation (Coutu et al., 2013; Trivedi, Gandhi, et al., 2013). Therefore, the hydropower industry needs to gain better knowledge of transient processes to ensure proper and reliable operation of the turbines.

One of the most harmful transient processes happens if the control system fails to rapidly close the guide vanes during a load rejection event and this failure leads to an instant rise of the runner's speed. The maximum speed attained by a runner is called runaway at full gate opening and no-load at other guide vane angles. Although runaway occurs far from standard turbine design operating conditions, this type of transient condition may occur also for other guide vane angles. The study of Francis turbines at no-load is necessary to ensure the structural integrity of turbine components and the safety of the hydropower plant.

In recent years, experimental and numerical research has been applied for analyzing the performance of hydraulic turbines in transient processes and off-design conditions. For instance, experimental approaches have been applied to investigate the dynamic behavior of hydraulic turbines under load variation, start-stop and load rejection. Hasmatuchi et al. (Hasmatuchi et al., 2011) performed an experimental study in a reduced scale model of a pump-turbine in order to analyze the flow unsteadiness under runaway transient and low flow conditions. At runaway, a stall cell rotating with the impeller was predicted in the vaneless gap between the impeller and guide vane, which led to hydraulic unbalance and strong structural vibrations. Trivedi et al. (Trivedi et al., 2015; Trivedi et al., 2014; Trivedi et al., 2014; Trivedi et al., 2014) performed transient pressure measurements in a high head Francis turbine during start-up, shut-down, load variations, load rejections, and spin-no-load covering the entire range of the prototype turbine operation. Pressure measurements showed that appropriate gate closure may reduce large pressure amplitudes during transient processes. Trivedi et al. (Trivedi et al., 2014) also indicated that the maximum amplitudes of the unsteady pressure fluctuations in a high head model Francis turbine at runaway condition were 2.1 and 2.6 times that of the pressure loading at the best efficiency operating point in vaneless space and runner, respectively. Pressure measurements during spin-no-load showed that the instantaneous amplitude of unsteady loads was similar to that computed for the critical transient conditions such as load variation, start-stop, emergency shut-down, and total load rejection (Trivedi et al., 2015) .

Houde et al. (Houde et al., 2012) experimentally studied the pressure fluctuations on a propeller turbine runner blade during a runaway test. The data post-processing showed that the main source of pressure fluctuations in the runner is associated with instabilities in the draft tube flow. As experimental methods are expensive and time-consuming in the context of transient process investigations, it is therefore gainful to develop alternative methods for investigating turbine transients.

Hydro acoustic models are fast and robust, and allow simulating the dynamic behavior of the complete hydropower plant during transient processes. These solve a hyperbolic system of equations for compressible mass flow and momentum conservation, which describes the dynamic behavior of a flow in the hydropower plant. However, these models depend on experimental results, and cannot predict unsteady 3-D flow features such as vortices, cavitation, and recirculation inside a hydro turbine. Nicolet et al. (Nicolet, 2007) used a 1D hydro acoustic

impedance method for modeling the hydraulic components of a hydropower plant in both transient and steady modes. This 1D modeling approach allowed simulating the evolution of turbine dynamic parameters such as rotational speed, pressure and discharge during a load rejection event.

Over the past two decades, increase in the computational capacity and advancements in numerical techniques have allowed to solve challenging engineering problems using computational fluid dynamics (CFD). In hydro turbines, 3D unsteady CFD simulations have been used for analyzing strongly turbulent flows at off-design conditions. The results have shown the existence of unsteady flow phenomena such as vortex break down, rotor-stator interaction and vortex shedding inside flow passages (Hosseinimanesh et al., 2014; Levchenya et al., 2010; Melot et al., 2014; Nennemann et al., 2005; Albert Ruprecht et al., 2002; Trivedi, Cervantes, et al., 2013).

Furthermore, 3D unsteady simulations have been successfully applied to analyze the flow behavior during transient processes for different types of hydro turbines. Nevertheless, the validations have only been partial due to the lack of experimental data for transient processes. Among these, Liu et al. (S. Liu et al., 2010) conducted 3D unsteady flow simulations for analyzing the flow inside a Kaplan turbine at runaway condition. The runaway transient process was characterized by investigating the time histories of rotational speed, flow rate, torque, axial force and pressure in the turbine. Moreover, pressure fluctuations have been reported in the draft tube due to the vortex rope precession. Kolšek et al. (Kolšek et al., 2006) calculated the engineering quantities of a bulb turbine during shut-down using unsteady flow simulations with standard k-ε turbulence model. The runner rotational speed and axial force acting on the runner agreed well with experiments during transient simulation with less than 5% deviation. Fortin et al. (Fortin et al., 2014) performed unsteady simulations on a model propeller turbine using URANS equations and transient rotor-stator interface model in order to study flow dynamics during a runaway event. For the runaway simulation, inlet boundary condition and runner rotation speed were changed according to the experimental data at each time step. The comparison of results showed that the numerical torque decreases more slowly than the experimental one in runaway. Furthermore, the numerical transient pressure signals showed a trend similar to the experimental data. However, the simulation underestimated the fluctuation amplitude.

Recently, transient processes in pump-turbines have been studied numerically by means of 3D unsteady flow simulations. For example, Liu et al. (J. T. Liu et al., 2012) showed the development of a vortex rope in the draft tube of a prototype pump-turbine running at no-load condition. Yan et al. (Yan et al., 2012) reported flow instabilities when the pump-turbine is brought from regular operating condition to runaway. Moreover, the rotating stall phenomenon was predicted at runaway condition due to rotating flow separation developing in several impeller channels. Yan applied frozen rotor-stator and transient rotor-stator interface models for the steady state and unsteady simulations, respectively. In addition, Widmer et al. (Widmer et al., 2011) and Casartelli et al. (Casartelli et al., 2014) performed unsteady simulations of a reversible pump-turbines including full spiral casing, distributor, runner, draft tube around the no-load condition. In these studies, the main goal was to investigate and predict the characteristic instability in the S-shaped region of the characteristic curve and as well the radial force imbalance on the machine caused by rotating stall.

Nicolle et al. (Nicolle et al., 2012) simulated a low head Francis turbine during the start-up phase using unsteady CFD simulations that included guide vane motion and an angular speed variation algorithm. The fluid domain included one distributor passage coupled with one runner passage using a transient rotor-stator interface model. These simulations showed a pumping flow motion that developed in the upper part of the runner passage at synchronization condition.

Coté et al. (Côté et al., 2014) assumed a “frozen” hydraulic condition in order to simulate the load rejection event of a Francis turbine. Unsteady RANS simulations were performed with fixed boundary conditions corresponding to a certain operation point on the runaway hill chart. Flow behavior analysis during load rejection showed the existence of a reversed flow (pumping flow) within the runner and a downward tangential flow near the shroud and draft tube cone wall.

Cherny et al. (Cherny et al., 2010) studied the transient behavior of a Francis turbine during runaway. He developed an approach consisting of a one-dimensional water hammer calculation for the penstock and 3D unsteady periodic stage simulation for the turbine. He applied a mixing plane boundary condition on the guide vane-runner and runner-draft tube interfaces with circumferential averaging of flow variables. He reported high-frequency pressure oscillations at a point of the draft tube surface, which were related to high frequency water hammer waves.

Li et al. (J Li et al., 2010) simulated the speed-no load condition at 9 guide vane angles for a Francis turbine with the k-ε- RNG turbulence model. However, very few details have been given about the results and numerical methods used. He reported the presence of intense swirling flow at the draft tube inlet, and secondary and transverse flows in the runner.

Nennemann et al. (B Nennemann et al., 2014) applied a combination of computational fluid dynamic and finite element analysis (FEA) in order to investigate the effect of unsteady loads on the fatigue life of a Francis turbine runner during no-load operation. The computational domain consisted of the distributor, the runner and the draft tube in the first simulation setup, and also included the complete spiral casing in the second setup. The transient rotor stator interface model was used for connecting rotating and stationary parts. The CFD simulations with a SAS (Scale-Adaptive Simulation) turbulence model predicted the stochastic behavior of pressure loads on the runner. The pressure loads were converted to dynamic stresses using FEA approaches. Experimental validation of no-load simulations showed that the approach was successful for predicting significant aspects of the flow behavior such as the maximum pressure and stress ranges, as well as the general stochastic nature of the flow.

Hosseinimanesh et al. (Hosseinimanesh, Devals, Nennemann, & Guibault, 2015) compared steady and unsteady methodologies using a stage interface model in order to calculate the no-load speed for Francis turbines. Overall, the numerical results agreed well with experimental data. The steady method showed more consistency than the unsteady method for predicting no-load speed for three different test cases at different operating conditions.

In the present investigation an unsteady methodology using transient rotor-stator interface model will be used in order to study a Francis turbine at no-load condition. The results will be evaluated and compared with experiments and unsteady stage simulations for high and medium head Francis turbines. The unstable characteristics due to the formation of the time-dependent phenomena will be described based on the unsteady CFD simulation of a complete Francis turbine.

This paper is organized in four sections. Following the present introduction, section 2 presents the studied cases, numerical setup and rotor-stator interface models. The main methodology, turbulence model and equations, employed in the no-load simulation are also introduced in this section. The validation of no-load simulations is addressed by comparing turbine engineering

quantities with experiments over the full range of admissible guide vane angles in section 3. The complex flow physics inside the turbine at no-load is discussed in this section. Section 3 also addresses the effect of interface models for computing the pressure on the blade sides, the flow behavior in the turbine domain, and engineering quantities at no-load condition. Section 4 presents some conclusions and closing remarks.

5.4 Computational aspects

5.4.1 Studied cases

The proposed methodology is evaluated by performing unsteady simulations on two types of Francis turbines, medium and high head, and two geometric configurations, a complete turbine and a single passage per blade row, using periodic boundary conditions.

For the complete turbine, the computational domain involves the full distributor, including 20 stay vanes and guide vanes, the entire turbine runner and the draft tube, as shown in Figure 5-1. The transient rotor-stator interface model (TRS) is used for connecting rotating and stationary components (see section 5.4.3 for a description of interface models).

In simulations involving a single passage per blade row, computations were performed on a reduced geometry involving one distributor channel (one stay vane and one guide vane), a single runner channel and the full draft tube, as shown in Figure 5-2. The stage interface model is used for connecting the runner and distributor channel, and the runner and draft tube, modeled in distinct frames of reference. The summary of turbine characteristics, as well as mesh information used for unsteady simulations is shown in Table 5-1. In the present paper, unsteady simulations using transient rotor-stator and stage interface models are called TRS and stage, respectively.

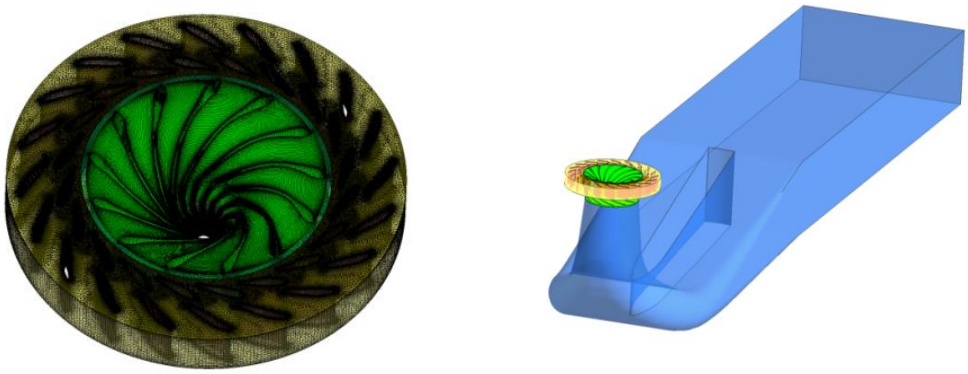

Figure 5-1 : Mesh for Francis turbine & distributor (left), computational domain of complete turbine in medium head-TRS simulation (right)

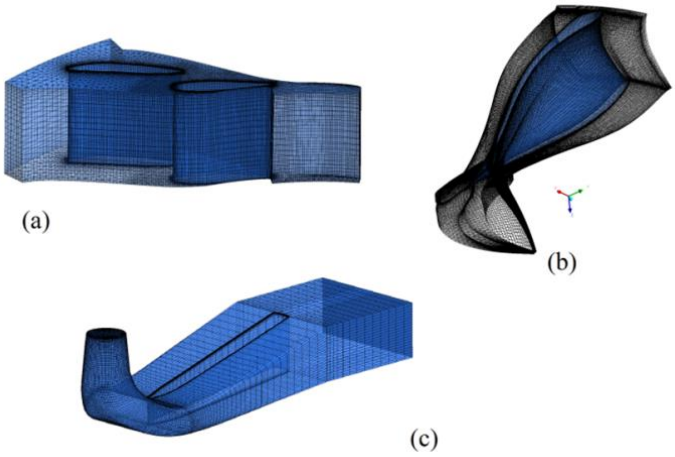

Figure 5-2 : Mesh for components in medium head-stage simulation: (a) distributor passage, stay vane and guide vane, (b) runner passage, (c) draft tube

Table 5-1 : Turbine geometry and mesh specifications used in no-load simulations

						Number of nodes			
	Type		Number of components			Stay vane & guide vane	Runner blade	Draft tube	
	Francis Turbine	Interface model	Stay vane	Guide vane	Runner blade	Hexahedra & prisms	Hexahedra	Hexahedra	Total
1	Medium head	stage	1/20	1/20	1/13	170k	144k	300k	614k
2	Medium head	stage	1/20	1/20	1/13	170k	140k	1300k	1610k
3	Medium head	stage	1/20	1/20	1/13	170k	1000k	1900k	3070k
4	Medium head	stage	1/20	1/20	1/13	500k	1100k	2700k	4300
5	Medium head	stage	1/20	1/20	1/13	700k	1645k	4100k	6445k
6	Medium head	TRS	20	20	13	3400k	1820k	1300k	6520k
7	High head	stage	1/20	1/20	1/15	200k	400k	200k	800k
8	High head	stage	1/20	1/20	1/15	600k	900k	1600k	3100k
9	High head	TRS	20	20	15	2300k	1300k	3400k	7000k

The meshes of all components were generated using mesh generation tools developed jointly by Andritz and Polytechnique. Multi-block-structured meshes for runner channel and draft tube, and hybrid meshes in a single domain for the guide vane and stay vane channels were used.

Table 5-1 also shows the details of the meshes and interface models used in the simulations for different cases. In this table, cases 1 to 5 are meshes of the medium head Francis turbine constructed using five distinct levels of mesh refinement for the single blade passage configuration. Case 2 for the single blade passage and case 6 for the complete turbine are equivalent in terms of mesh density, as they use the same mesh size per blade channel and identical meshes in the draft-tube. Figure 5-3 presents histograms for three mesh quality parameters computed on the mesh of case 2. As shown by these histograms, element volume and maximum edge length ratio are very well controlled in the meshes for all components (Figures 5-3a and 5-3c). The distribution of minimum angle is also very well controlled in the distributor

and draft-tube (Figure 5-3b). Structured mesh generation in the runner is more difficult, as illustrated by the distribution of minimum angle for that component. The smallest angles are however still in an acceptable range (> 10 degrees) for that component also.

A sensitivity study taking into account five levels of mesh refinement was carried out to evaluate the influence of the mesh density on the unsteady simulation results at the no-load condition. Figures 5-4 and 5-5 present the medium head turbine speed factor N_{ed} and discharge factor Q_{ed}, computed at no-load conditions for the different mesh densities at a gva of 16°. The speed and discharge factors are calculated using the formulation in (IEC61364, 1999). The details of computations will be described in section 5.4.4.

The results which were validated by experimental values (N_{ed}= 0.505, Q_{ed}= 0.12), show that all cases predict N_{ed} with nearly the same accuracy of around 3.4% error. Prediction of the discharge factor Q_{ed} was closest to the experimental value for mesh level 3 (3070k). When the mesh density increases from 3070k (level 3) to 4300k and 6445k (level 4 and 5), the accuracy of the speed factor N_{ed} at no-load condition improves slightly (by 0.22% for mesh level 5), while the accuracy of the discharge factor Q_{ed} decreases by almost 1.5% for the finest mesh. In order to reach a compromise between accuracy and computational cost, and since the accuracy of the speed factor, which constitutes the parameter that best quantifies the turbine behavior at the no-load condition, is well predicted using a mesh density corresponding to level 3 (3070k), this density was selected for stage simulations of the medium head Francis turbine. In the next section, the case 3 and 6 are called medium head-stage and medium-head TRS, respectively. Similarly, case 8 and 9 are called high head-stage and high head-TRS.

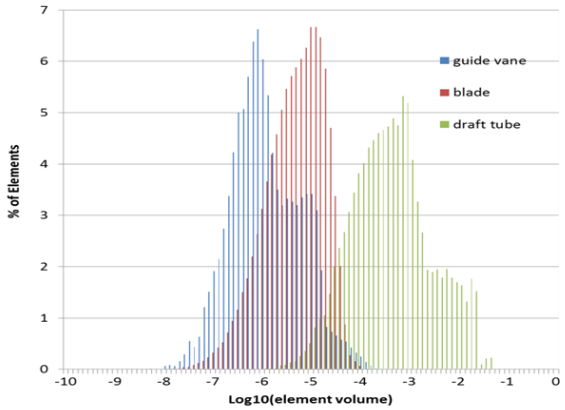

(a)

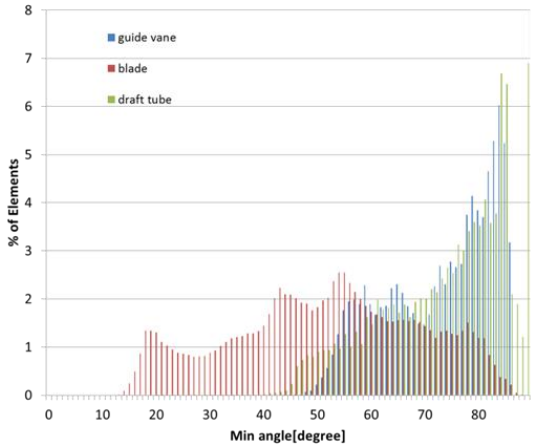

(b)

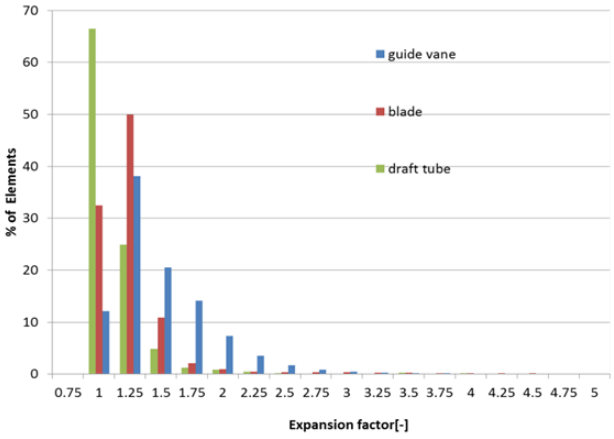

(c)

Figure 5-3 : Mesh quality histograms (a) Element volume (log value) distribution, (b) Minimum angle distribution,(c) Expansion factor distribution

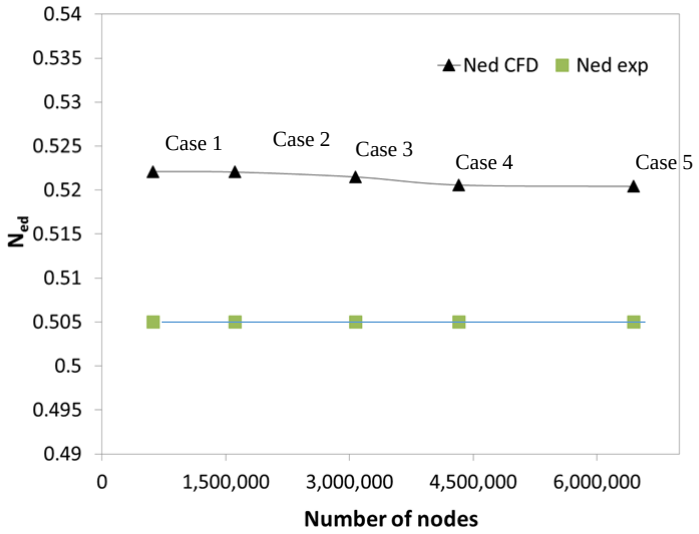

Figure 5-4 : Comparison of simulated and experimental speed factor N_{ed} at no-load condition for different mesh densities

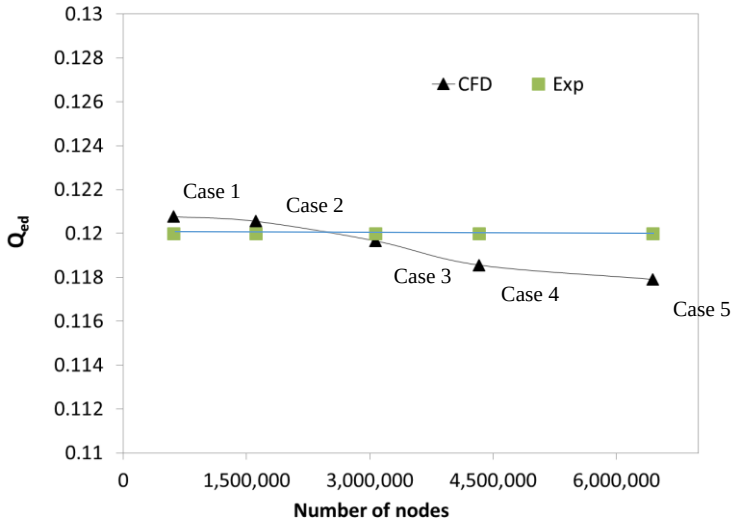

Figure 5-5 : Comparison of simulated and experimental discharge factor Q_{ed} at no-load condition for different mesh densities

5.4.2 Numerical set up

In the present study, the no-load and runaway transient processes are simulated by applying unsteady Reynolds averaged Navier-Stokes 3D calculations at different operating conditions using the Ansys-CFX 14 commercial solver.

The standard *k-ε* turbulence model is used for treating turbulence. While several turbulence models were available to carry out these simulations, the choice of the standard *k-ε* model was based on a number of studies which have shown that this model is reliable, robust and economical for simulating high Reynolds number flows (Thi C. Vu, Devals, Zhang, Nennemann, & Guibault, 2011). For example, Galvan's investigation (Galvan et al., 2011) on the steady state swirling flow in a draft tube showed that the standard *k-ε* turbulence model demonstrates good balance between reliable performance and computational cost. Other models, such as SST, have shown improved precision, but require more refined meshes to achieve adequate precision and numerical stability (Maruzewski et al., 2010). A goal of this study being to compare stage and TRS simulations for several difficult off-design flow conditions, computational cost and numerical stability were key criteria in selecting the turbulence model.

The momentum equations and turbulent advection equations have been discretized using the high-resolution scheme and first-order scheme respectively, with convergence tolerances of all main primitive variables set to 1E-05 on the root mean square (RMS) residuals. Besides, the quantities of torque, runner angular speed and inflow are tracked during simulation at monitoring points. Whenever their time-averaged values become steady, the solution is considered to have converged. Unsteady simulations are performed using the second order backward Euler scheme to approximate the transient term in the Navier-Stokes equations.

The standard k-ε model uses the scalable wall function approach to improve accuracy and robustness near the wall. Table 5-2 shows the minimum, average and maximum value of Y^+ for the four cases. Figure 5-6 illustrates the distribution of Y^+ on solid boundaries of each turbine component for simulations at the no-load condition for a gva of 16^o. As shown in the figures, the Y^+ distribution on component walls is overall very well controlled, apart from local regions near the leading edge on both sides of the runner blade, where the flow becomes highly swirling and detached, as will be shown in section 3.

Table 5-2 : Average Y+ for simulation domains

	Guide vane			Runner blade			Draft tube wall		
case	min	ave	max	Min	ave	max	min	ave	max
Medium head-TRS	61	225	756	73	461	1767	14	313	2221
Medium head-stage	21	237	477	9	297	1010	1	215	794
High head-TRS	15	267	1053	84	537	2991	15	250	1859
High head-stage	3	108	437	10	390	1620	2	307	696

For all simulations, the inlet boundary condition is set to the total pressure associated with the turbine net head. The outlet boundary condition is specified as zero-averaged static pressure. No-slip boundary conditions are imposed on all solid walls. Figure 5-7 presents the geometry and boundary conditions for medium head-stage simulations.

5.4.3 Modeling rotor-stator interfaces

In the proposed methodology, two interface models are used: transient rotor-stator (TRS) and stage models. Both are applied to capture the interaction between rotating and stationary components during transient process simulations. The TRS model simulates the transient relative motion between components on each side of the interface. For this purpose, the interface position is updated at each time step as the relative position of grids on each side of the surface changes. This approach preserves all interaction effects between components that are in relative motion with each other. Hence, TRS simulations require large computer resources in terms of simulation time, memory and quantitative post processing of data. On the contrary, the stage model allows for a simpler and faster solution process compared to the TRS. The stage model performs circumferential averaging of the fluxes at the interface, and therefore neglects some transient effects. Assuming cyclic periodicity among blade channels in a row, the stage averaging process

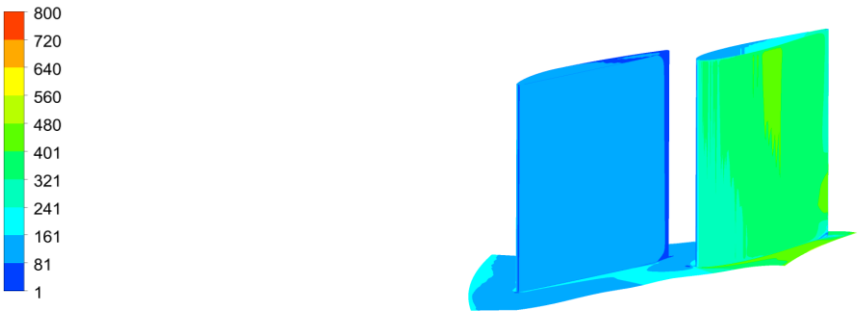

(a) Stay vane and guide vane

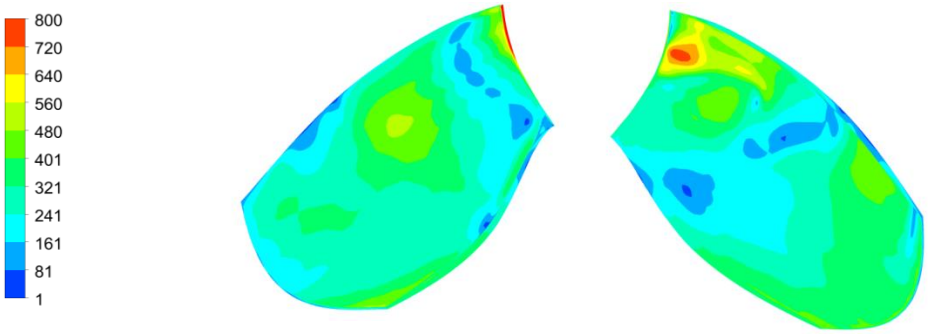

(b) Runner blade pressure side (left) and suction side(right)

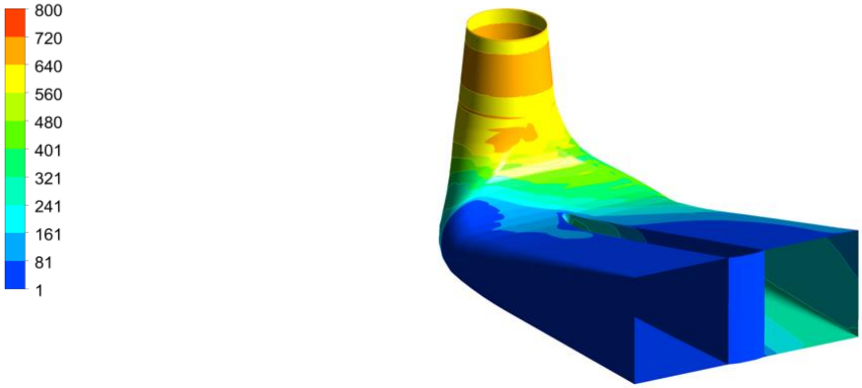

(c) Draft tube

Figure 5-6 : Distribution of Y^+ at no-load on medium head Francis turbine components (gva 16°)

allows simplifying the computational domain geometry by considering a single blade channel in each row. Typically, by reducing the size of the domain, computational time is reduced by a factor in the order of 6 for stage simulations, compared to TRS. Comparison between simulation results with TRS and stage interface models allows evaluating the proposed methodology in terms of efficiency and reliability for application in an industrial design processes.

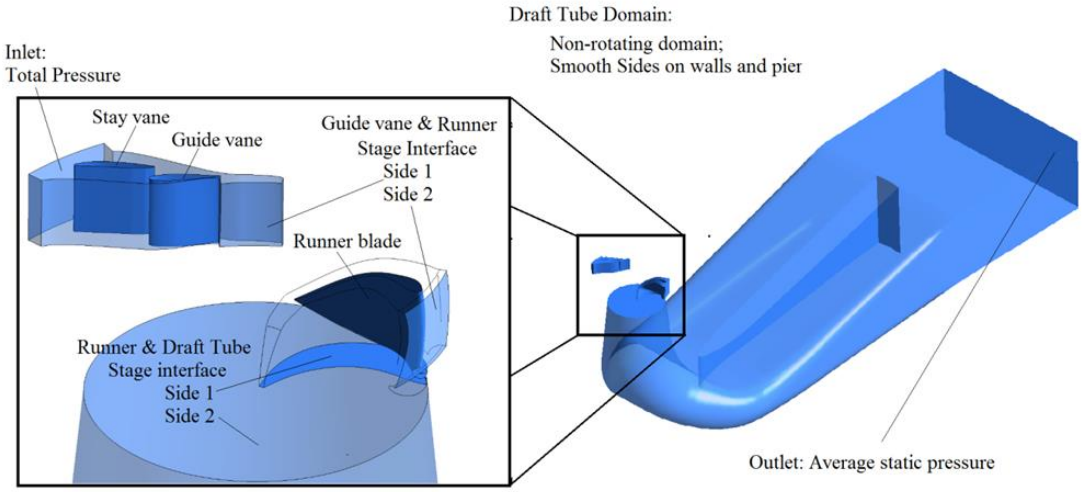

Figure 5-7 : Geometry and boundary conditions of computational domains in medium head-stage simulation

5.4.4 No-load simulation methodology

The proposed methodology uses the angular momentum equation for the rotating mass to estimate the runner torque during runaway and no load conditions. The unbalanced torque between the runner and generator changes as follows:

$$T - T_g = I_z \frac{d\omega}{dt} \tag{5-1}$$

Here T denotes the runner hydraulic torque (Nm), T_g is the generator or payload torque (Nm), I_z is the moment of inertia of the complete runner and generator assembly (kg m^2), and ω is the runner angular speed (rad/s). When a load rejection event without guide vane closing occurs within a hydropower plant, the electromagnetic torque instantaneously drops to zero ($T_g = 0$), and the angular speed of the runner starts to rise monotonically. However, the rate of increase in

angular speed eventually decreases because of hydraulic losses in the hydraulic system. Finally, the runner angular speed reaches a maximum value, called the runaway speed. Under such circumstances, the runner moment tends to zero.

Algorithm 5-1 presents the proposed methodology for simulating runaway and no-load conditions. The first step consists in generating meshes from parametric geometry descriptions of each component. The numerical setup is implemented as described in the previous section for the selected guide vane angle. Then, a steady stage simulation is performed at the speed factor of the best efficiency point $N_{ed,1}$ in order to initialize the CFD model for the next step. In step 5, the blade torque T_1 is derived from the converged simulation. Then, a single unsteady simulation is performed during which the angular speed is updated at each iteration by

$$\omega_n = \omega_{n-1} + \frac{T_n \Delta t}{I_z} \tag{5-2}$$

Equation 5-2 is derived from Equation 5-1 by a first order explicit discretization. In Equation 5-2, Δt represents a time step (s) that is adjusted automatically based on the runner angular speed variation during the transient process. In the simulations performed here, the time step was computed to meet a 4° angular variation of the runner at each iteration. Preliminary evaluation of the influence of the time step for values of 1° to 8° per time step have shown that speed and discharge coefficients were minimally affected for time steps in the range of 1° to 4°. The value of 4° was therefore chosen to minimize overall computational time. Equation 5-2 shows that the runner torque and the inertia of the unit have a significant impact on the angular speed change.

In Algorithm 5-1, for the process to be considered converged at no-load, the following conditions must both be satisfied:

- $\frac{|N_{ed,n} - N_{ed,n-1}|}{N_{ed,n-1}} < 2\ \%$
- $\left|\frac{\overline{P_{ed,n}}}{P_{ed,BEP}}\right| < 1\ \%$

Otherwise, the unsteady simulation continues or stops if the loop control value *n* reaches a preset maximum value. The criterion based on the power coefficient is the one which controls the iteration process for most simulations. Theoretically, at the no-load condition, the power coefficient should reach a value of zero. In practice however, significant fluctuations are present

in the flow which prevent the power coefficient from stabilizing at a very small value. For that reason, an average of the power coefficient is taken over five fluctuation cycles, and compared to the value at best efficiency. The choice of the threshold at 1% is based on the amplitude of fluctuations that were observed over a large number of simulations. The criterion on the speed coefficient was added to prevent simulations from stopping prematurely while the runner is still accelerating.

Algorithm 5-1 Unsteady no-load computation

Input: Guide vane angle **Output:** Runaway speed, inlet flow rate, pressure magnitude on the blade
1: Generate meshes
2: Numerical setup
3: Select speed of an operating conditions $N_{ed,1}$
4: Perform steady simulation for the selected operating condition
5: Compute torque T_1, from steady simulation results
6: Set $n = 2$
7: **While** unsteady simulation not converged **do** Steps 7.1-7.4
7.1: From previous point $(N_{ed,n-1}, T_{n-1})$ compute the next operating condition at $N_{ed,n}$
7.2: Continue unsteady simulation at $N_{ed,n}$
7.3: Compute torque T_n and power factor $P_{ed,n}$
7.4: Set $n = n + 1$
8: $N_{ed,no-load} = N_{ed,n}$

All processes in Algorithm 5-1 are implemented using the commercial flow solver Ansys CFX. This is used in conjunction with a user subroutine, which computes and returns values of angular velocity, time step and friction torque.

In Equation 5-2, the friction torque has been considered when estimating the runner total torque, in order to have a more reliable representation (see (Hosseinimanesh, Devals, Nennemann, & Guibault, 2015) for details). The friction torque included the mechanical losses caused by operation of water in the shroud and hub. However, bearing, shaft friction was ignored.

5.5 Results

The evolution of engineering quantities is studied during no-load simulations. In the full range of admissible guide vane angles, the no-load speed value is computed and compared with experimental results in order to validate the proposed methodology. Furthermore, the flow physics inside the turbine, computed in medium head-TRS simulations, is analyzed and compared with medium head-stage simulation results to show the effect of interface models on the simulation accuracy.

5.5.1 Engineering parameters

Figure 5-8 shows the evolution of three normalized runner parameters, the angular speed ω^* (ω/ω_{BEP}), the runner torque T^* (T/T_{BEP}) and discharge Q^* (Q/Q_{BEP}) during medium head-TRS and stage simulations, for a gva 16°. Both no-load simulations started from the best efficiency operating point (BEP). It is noted that TRS and stage simulations show similar trends for all runner parameters during the no-load process.

Figure 5-8a shows the variation of normalized angular speed ω^* during no-load transient. In Figure 5-8a, the runner accelerates sharply at the start of the no-load simulation. After 5 seconds, the speed growth rate decreases. Finally, it converges to nearly 170 percent of the synchronous speed in about 15 seconds. It can be observed that the runner acceleration at the start of no-load is associated with a sharp drop of the runner torque which finally approaches a near zero value.

Fluctuations are observed in the torque for both types of interfaces, which shows the unstable characteristics of the no-load condition. The runner torque starts to oscillate after 9 and 18 seconds in the TRS and stage simulations, respectively. Therefore, TRS predicts more dynamic properties of no-load condition. Comparison of Figure 5-8b and 8c shows that the oscillation amplitude is higher for the stage than the TRS approach. The unsteady behavior of the torque induces large dynamic loads on the runner blades, which is discussed in the next section.

Moreover, Figure 5-8 indicates that the flow rate decreases by 30% during runaway in both stage and TRS simulations, while the guide vane angle is kept fixed. The reduction of flow rate is caused by the occurrence of a flow blockage in the runner inlet region. The flow physics during this process is highly complex and is investigated in detail in section 5.5.3.

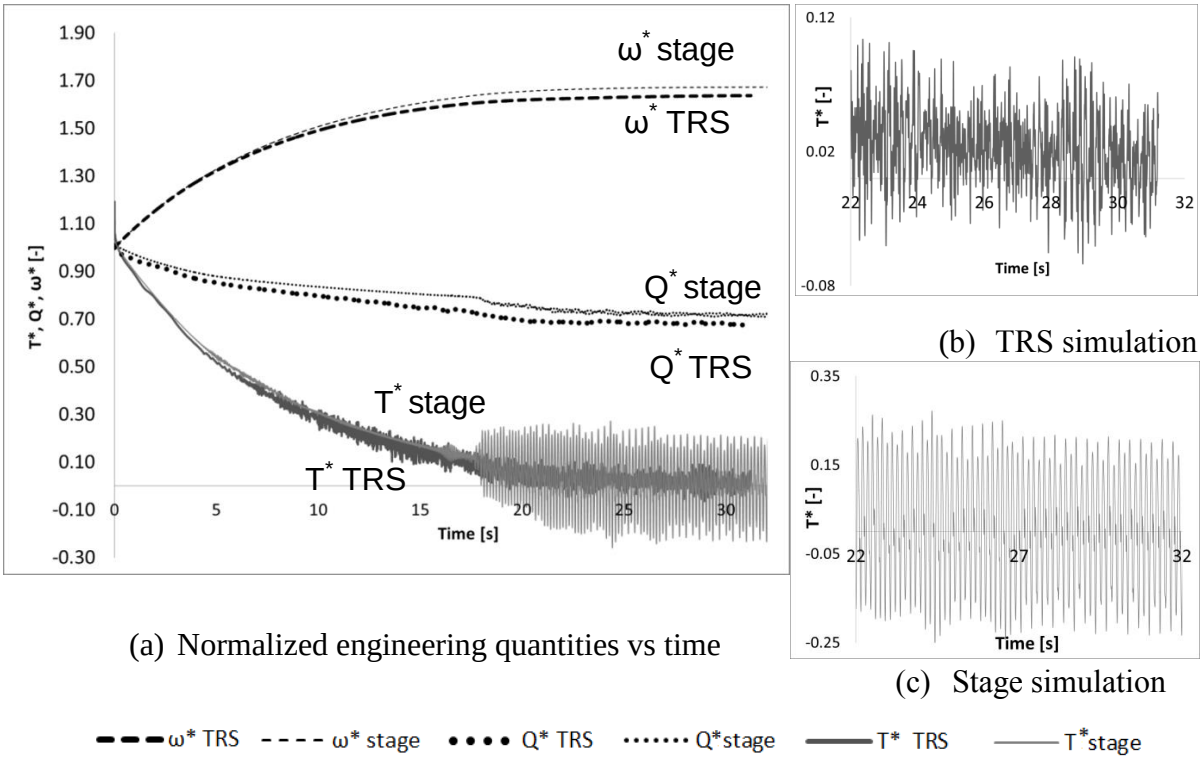

(a) Normalized engineering quantities vs time

(b) TRS simulation

(c) Stage simulation

Figure 5-8 : Variation of the normalized runner angular speed, flow rate, torque in medium head-TRS & stage simulations for a gva 16°

The unsteady methodology is validated by comparing speed factors N_{ed} and discharge factor Q_{ed} at the no-load condition with experimental data in Figures 5-9 and 5-10. Figure 5-9(left) compares the speed factors computed for the medium head-TRS and stage simulations with experiments, and Figure 5-9(right) compares the computed speed factors for the high head test cases with experiments. For the high head Francis turbine, the two methodologies predict similar speed factors in the gva range between 20° and 26°, while the relative error decreases by 2.46% using the TRS simulation at gva of 15°. For the medium head Francis turbine, the TRS simulation

results are more accurate than the stage simulations in the gva range from 11.5° to 22°. The maximum error is calculated as 5.98% for a gva 22° in the stage simulation, as shown in Table 5-3.

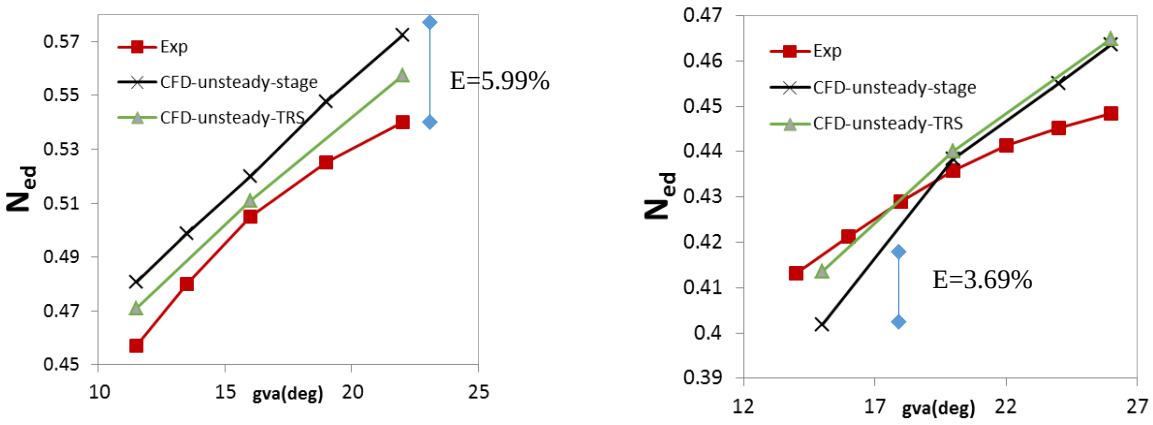

(a) Medium head Francis turbine

(b) High head Francis turbine

Figure 5-9 : Comparison between CFD predictions and experimental measurements (ANDRITZ Hydro, 2014) of speed coefficients Ned at no-load conditions (E=Error bar[7])

Moreover, the TRS and stage simulation are validated for computing the discharge factor Q_{ed} at no-load condition in Figure 5-10. For the high head Francis turbine, the stage simulations predict slightly more accurate discharge factors in gva range 20° and 26°. For instance, the stage simulations computed the discharge factor 2% and 3% more accurately compared to TRS simulations at guide vane angles 20° and 26°, respectively. A maximum error of 15.8% was calculated at the gva of 15° for the TRS simulation. This discrepancy between experiment and CFD in the prediction of the discharge factor may be attributed to a number of limits in the CFD approach, including the choice of the turbulence model, and limited spatial and temporal resolution. For the medium head Francis turbine, the stage simulations are more accurate in the gva range of 13.5° to 22°. The relative error reaches a maximum value of 8.9% using stage simulation at gva 11.5°.

[7] Error bar presents the discrepancy between CFD and experimental data.

Table 5-3 : Maximum discrepancy between the numerical and experimental speed factors N_{ed} and discharge factors Q_{ed} at no-load condition

Case	Max discrepancy (%)(Guide vane angle (deg))	
	N_{ed}	Q_{ed}
Medium head-TRS	3.22% (22^o)	6.89% (16^o)
Medium head-stage	5.99% (22^o)	8.9% (11.5^o)
High head-TRS	3.66% (26^o)	15.8% (15^o)
High head-stage	3.69% (15^o)	26.7% (15^o)

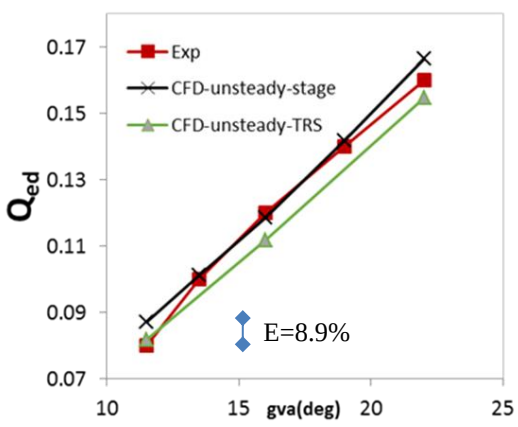

(a) Medium head Francis turbine

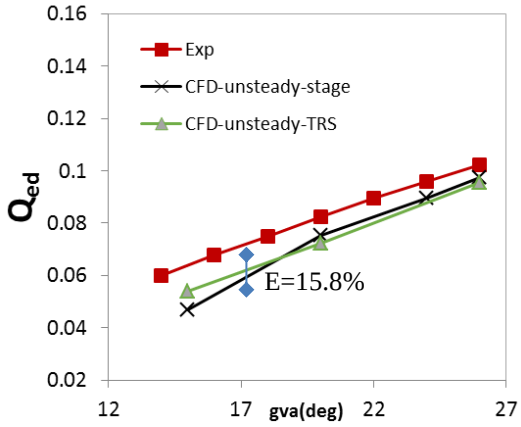

(b) High head Francis turbine

Figure 5-10 : Comparison between CFD predictions and experimental measurements (ANDRITZ Hydro, 2014) of flow coefficients Qed at no-load conditions (E= Error bar)

5.5.2 Pressure

Figure 5-12 shows the evolution of normalized pressure[8] signals at no-load for medium head TRS and stage simulations at gva 16°. The pressure signals are captured at monitoring points PS and

[8] $P*$: normalized pressure ($= P/\rho g H$).

SS, which are located on the pressure and suction sides of the runner blade, respectively (see Figure 5-11). The average pressure increases on both sides under no-load conditions, but a larger growth is seen at SS for both simulations. Table 5-4 compares the average of captured pressure signals between no-load and BEP conditions. At no-load, the average pressure at SS rises by 139% and 160% for TRS and stage simulations, respectively. While the average pressure at PS increases 4% and 12% for TRS and stage, respectively.

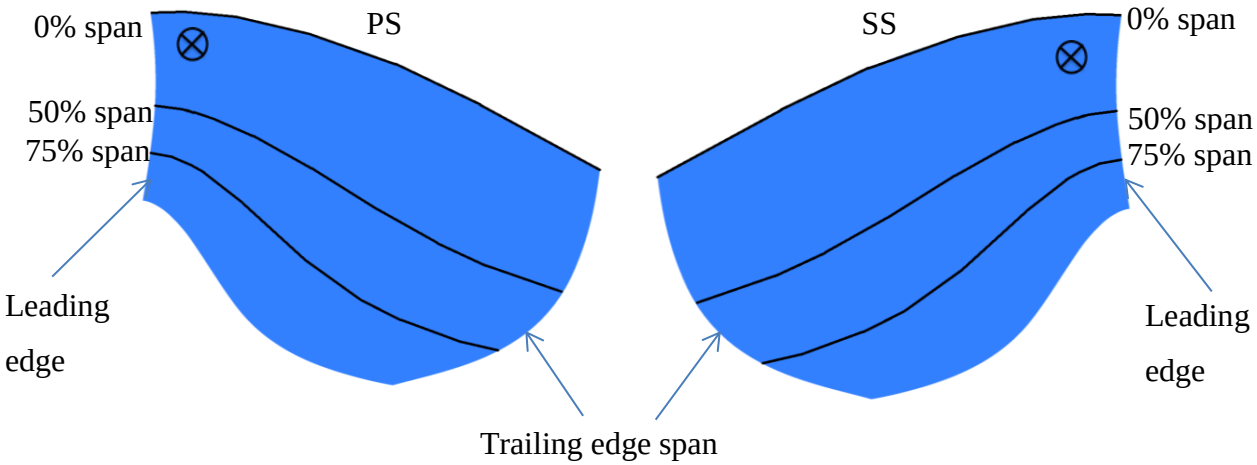

Figure 5-11 : Monitoring points on pressure (PS) and suction (SS) sides of blade in medium head-TRS & stage simulations

Table 5-4 : Comparison of normalized averaged pressure fluctuations in BEP and no-load condition for medium head-TRS & stage simulations at gva 16°.(PS: blade pressure side, SS: blade suction side)

	BEP		No-load	
	PS	SS	PS	SS
Medium head-TRS	0.38	0.12	0.40	0.29
Medium head-stage	0.39	0.11	0.43	0.29

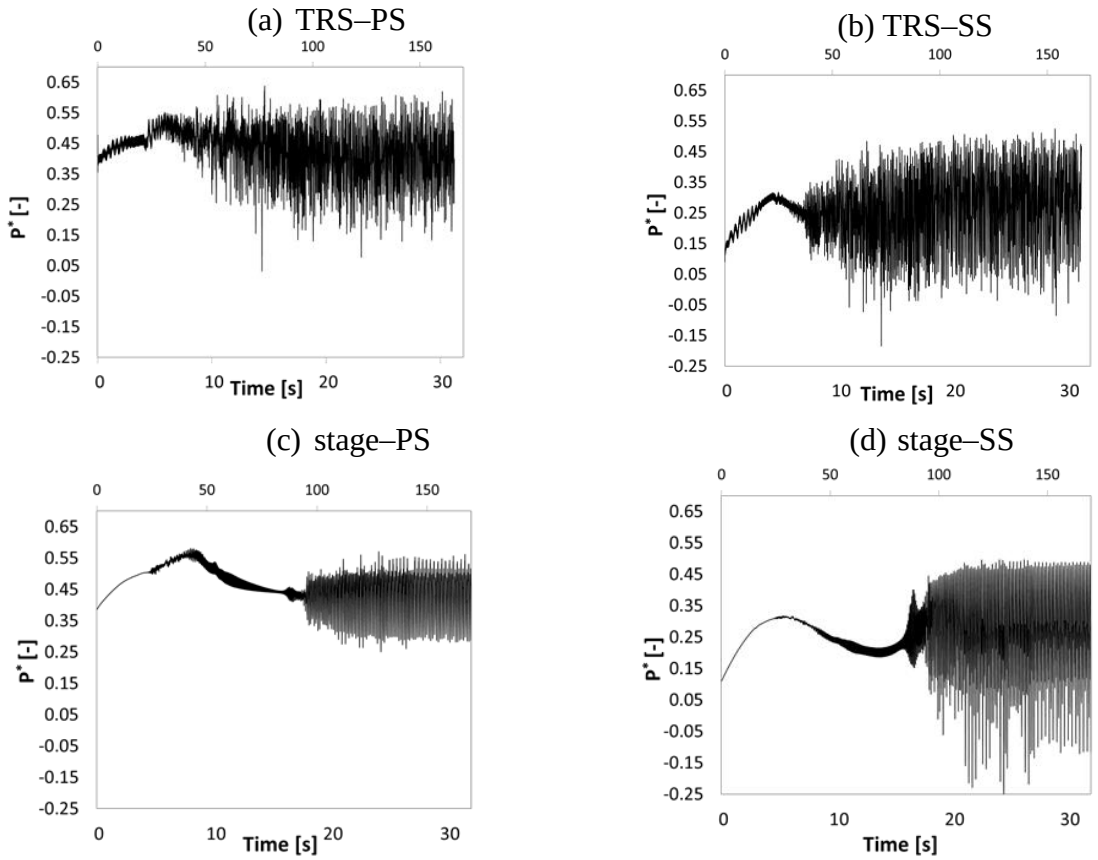

Figure 5-12 : Time history of normalized pressure fluctuation at PS and SS in medium head-TRS & stage simulations for a gva 16°

Furthermore, the pressure signals start to oscillate after 9 s and 18 s for unsteady TRS and stage simulations. The pressure oscillations are induced by unsteady phenomena such as vortex rope break down inside the runner and draft tube, described in the next section. Figure 5-13 shows a Fourier analysis of pressure fluctuations at PS and SS. The normalized peak amplitude and corresponding frequency at PS and SS for TRS and stage simulations are shown. The peak amplitudes occur at SS for both simulations. The value of peak amplitude predicted by the unsteady stage method is 2.33 times larger than that predicted by unsteady-TRS method. It can be observed that the dominant normalized frequencies are very similar for TRS and stage simulations.

Figure 5-14 compares the normalized time-averaged pressure distribution on the blade at no-load conditions and BEP for medium head TRS simulation at gva 16°. A significant pressure drop

occurs close to the trailing edge and hub on both sides during the no-load process. This low-pressure zone expands further along the hub on the suction side compared to the pressure side. Moreover, the pressure doubled up near the leading edge on the suction side. This pressure increase may be attributed to the vortical flow near the runner inlet, which is described in the next section.

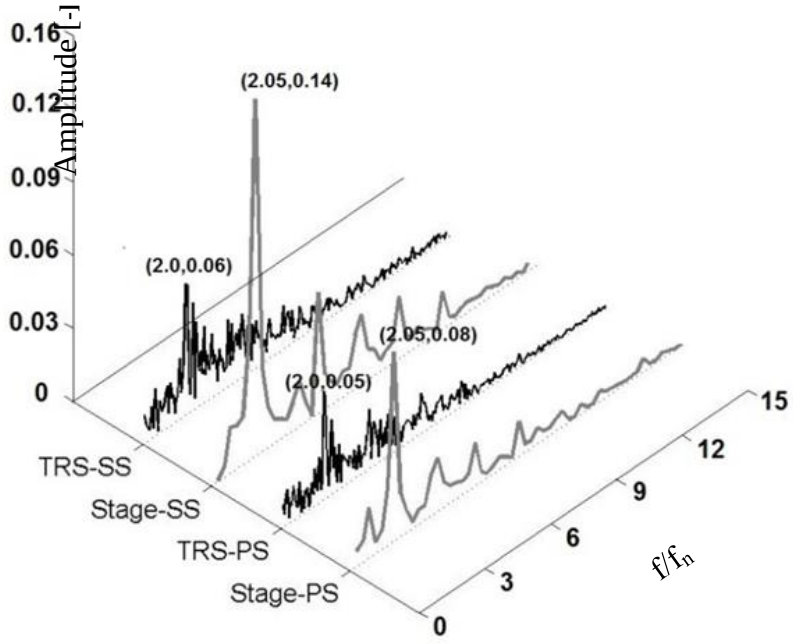

Figure 5-13 : Spectral analysis of normalized pressure fluctuations at SS & PS at no-load from medium head-TRS & stage simulations for a gva 16°

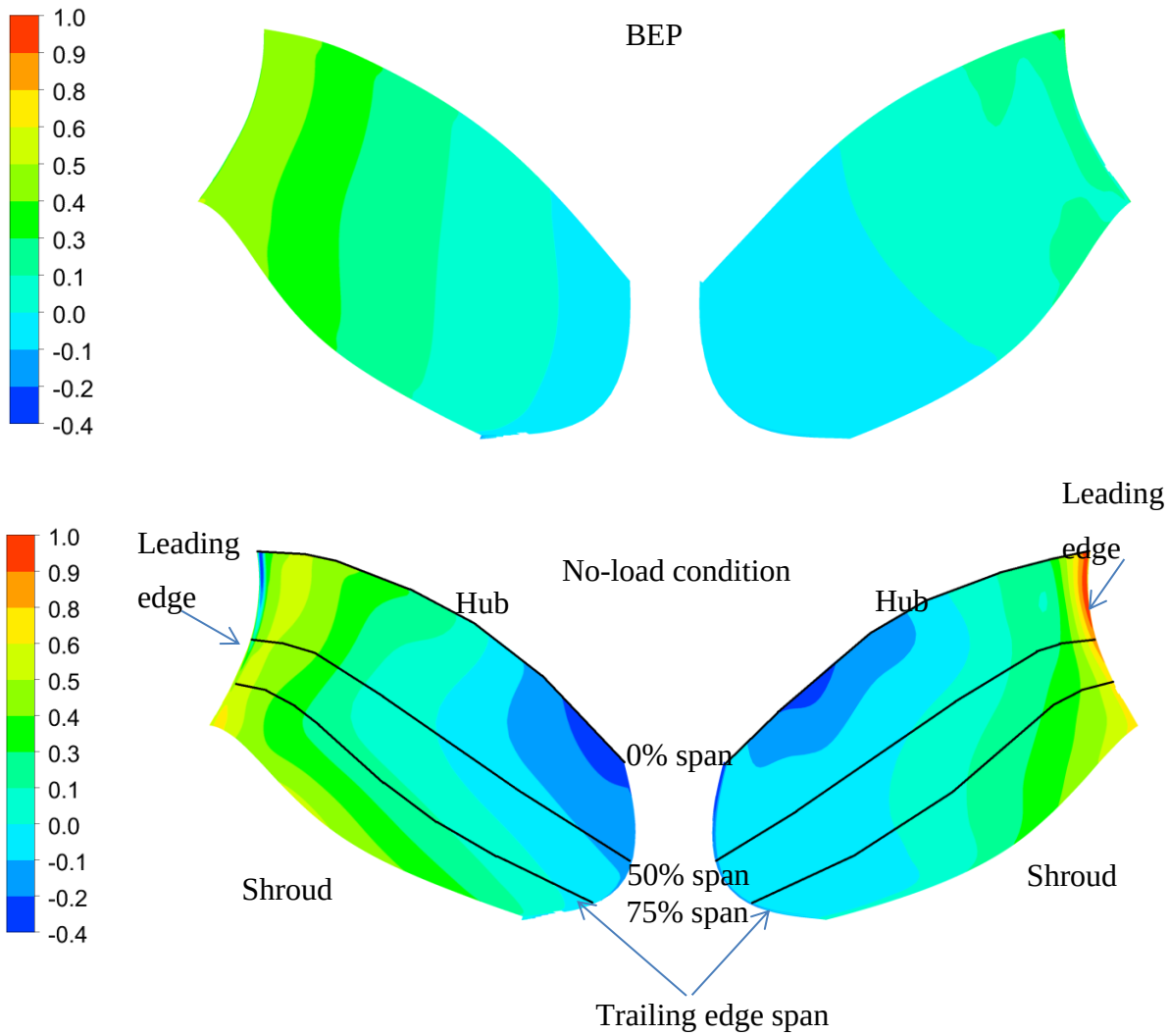

Figure 5-14 : Normalized time-averaged pressure distribution on the blade pressure (left) and suction (right) sides at BEP (top) and no-load (bottom) from medium head-TRS simulation for a gva 16°

5.5.3 Flow physics of no-load condition for medium head TRS simulation

This section studies in greater details the unsteady flow features computed during the no-load process by examining the results of medium head TRS simulations for a gva 16°. Figure 5-15 illustrates 3D streamlines of the flow within the runner at no-load. Overall, the flow involves three main flow phenomena that dissipate the input energy in the runner, and cause the zero-torque at no-load. It can be observed that vortices with a tangentially-oriented axis are spanning between the pressure and suction sides in the middle of the blade near the leading edge in Figure

5-15. A strong downward tangential flow concentrates near the leading edge and shroud and a mainly rotating reversed flow is moving towards the hub.

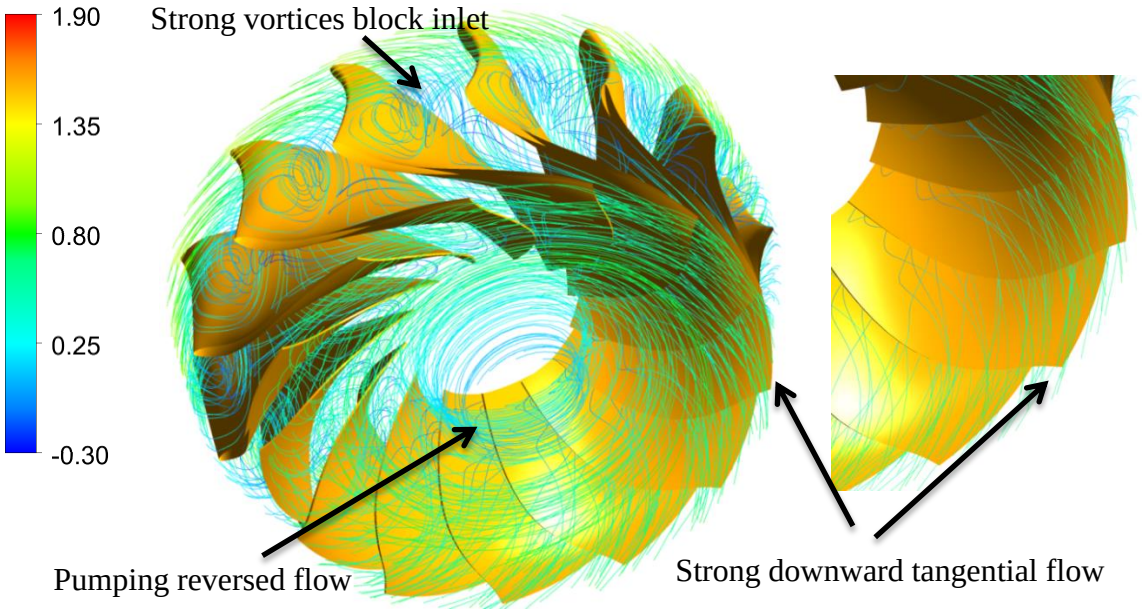

Figure 5-15 : 3D Streamlines of normalized time-averaged velocity within runner at no-load in medium head-TRS simulation for a gva 16°

Figure 5-16 illustrates the distribution of time-averaged axial vorticity at 1 % and 50 % span positions. In Figure 5-16(left), a strong vorticity is observed close to the trailing edge on the suction side at 1% span near the hub. It is created by the rotating reversed flow (pumping flow) in the runner center. Figure 5-16(right) illustrates the distribution of time-averaged axial vorticity at 50 % span (mid of runner) at no-load. Moreover, a region with high axial vorticity is observed near the suction side and leading edge. It shows that the strong vortices, already depicted at 1% span near the hub and trailing edges, have changed position in the blade channel approaching the leading edge.

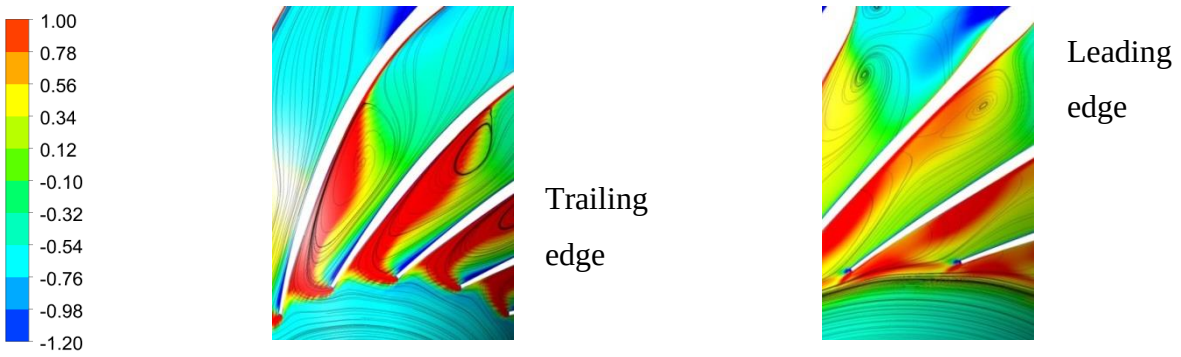

Figure 5-16 : Normalized time-averaged axial vorticity at 1% span (left) and 50% span (right) runner at no-load from medium head-TRS simulation for a gva 16°

Figure 5-17 presents surface streamlines and the time-averaged vorticity field in the mid of the blade channel. From this representation it can be appreciated that strong tangential vortices with a tangentially oriented axis have blocked the largest part of the inlet runner passage. Consequently, the discharge entering the runner is reduced by 30 percent, as mentioned in section 5.5.1. Figure 5-17 also describes the flow direction inside the blade channel. It is observed that the runner discharge is separated into two main flow directions. The main flow is concentrated near the shroud before entering the draft tube. The rest of the flow is deflected towards the hub after interaction with reversed flow.

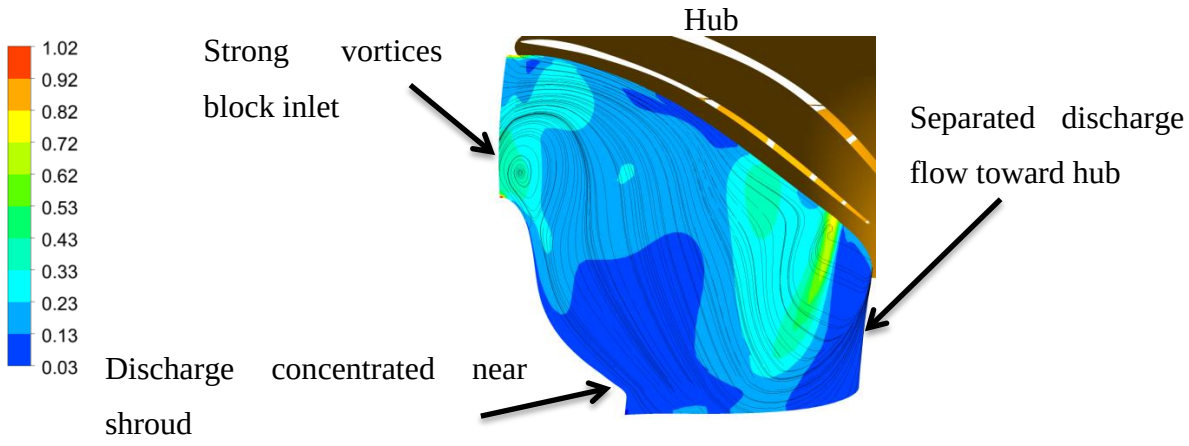

Figure 5-17 : Normalized time-averaged velocity streamlines & vorticity magnitude at mid surface in blade channel at no-load condition from medium head-TRS simulation for a gva 16°

The distribution of normalized time-averaged tangential velocities and axial velocities in a plane section of the draft tube are shown in Figure 5-18. Figure 5-18 (right) shows that the runner

discharge enters near the draft tube cone's wall. On the other hand, a mainly axial flow returns to the runner in the cone center. Figure 5-18 (left) shows that runner discharge flow is strongly tangential near the cone wall.

Overall, the high tangential flow at the runner outlet leads to a displacement of the flow towards the draft tube periphery. Consequently, a low pressure region is generated in the center of the draft tube which sucks in flow from downstream, thus creating reversed flow. On the interface between the axial reversed and the tangential peripheral flow, a strong shear layer exists, which becomes unstable, leading to vortex breakdown. The rapid change in the vortex flow structure in the conical section of the draft-tube induces pressure fluctuations that propagate upstream to the turbine runner blade, as indicated in Figure 5-12.

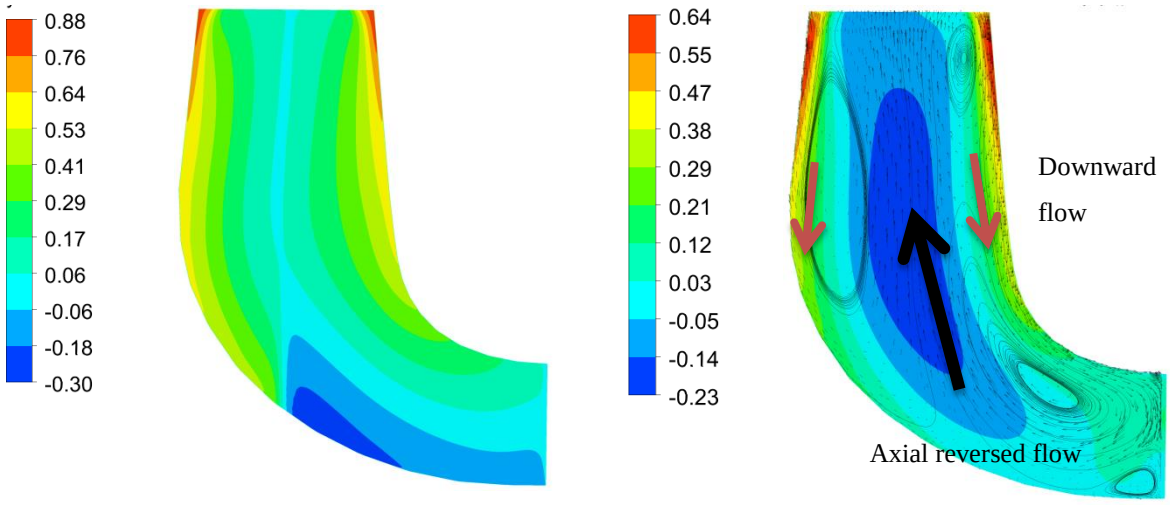

Figure 5-18 : Normalized time-averaged tangential velocity (left) and axial velocity field (right) on a plane section through the draft tube at no-load from medium head-TRS simulation for a gva 16°

5.5.4 Comparison of flow physics inside the runner and draft tube between medium head TRS and stage simulations

Medium head TRS and stage simulations for a gva 16° are also used to predict the pressure coefficient Cp at three different locations along the runner blade. The pressure coefficient definition is based on the numerical time-averaged pressure, normalized by dynamic pressure at

the runner outlet. Figure 5-19 shows a comparison of Cp curves between TRS and stage simulations. Both simulations present a similar trend of Cp at different span positions. Furthermore, the maximum Cp is observed close to the leading edge at 0%, 50% and 75% span. There is a larger Cp difference between suction and pressure sides at 0 % span (near the hub) compared to other spans.

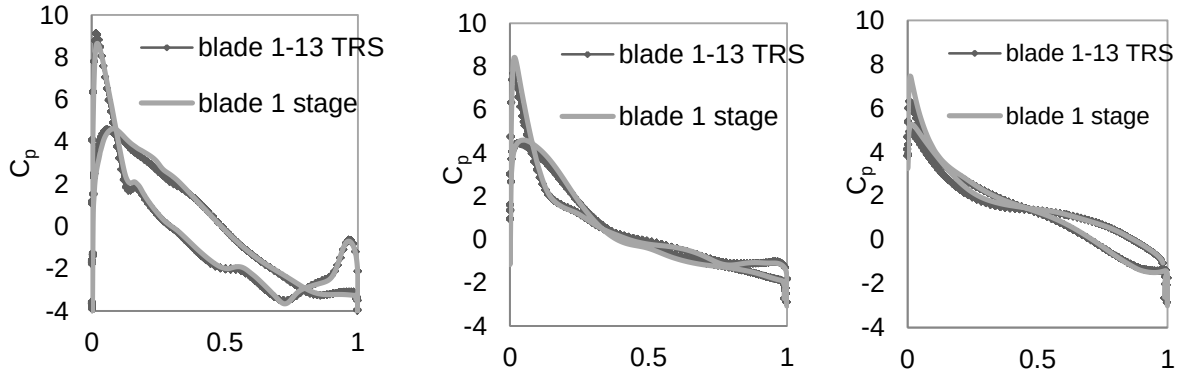

Streamwise (0-1) Streamwise (0-1) Streamwise (0-1)

(a) 0 % span (b) 50 % span (c) 75 % span

Figure 5-19 : Comparison of time-average pressure coefficient C_p at no-load from medium head-TRS & stage simulations for a gva 16° at different spans

Figure 5-20 shows the normalized velocity streamlines and contours in the plane z/L = -0.4. In Figure 5-20, for both simulations, a uniform high-velocity flow enters the runner region. Inside the runner passage, the streamline patterns indicate a recirculation zone, which dominates the flow near the leading edge, for all simulations. Moreover, Figure 5-20 shows that a low velocity region appears in the middle of the passage, close to the suction side. It corresponds to a region with high axial vorticity, shown in Figure 5-16(right). In the stage simulation, the velocity field in the runner passage shows a weak velocity zone near the leading edge and a high velocity zone close to the trailing edge.

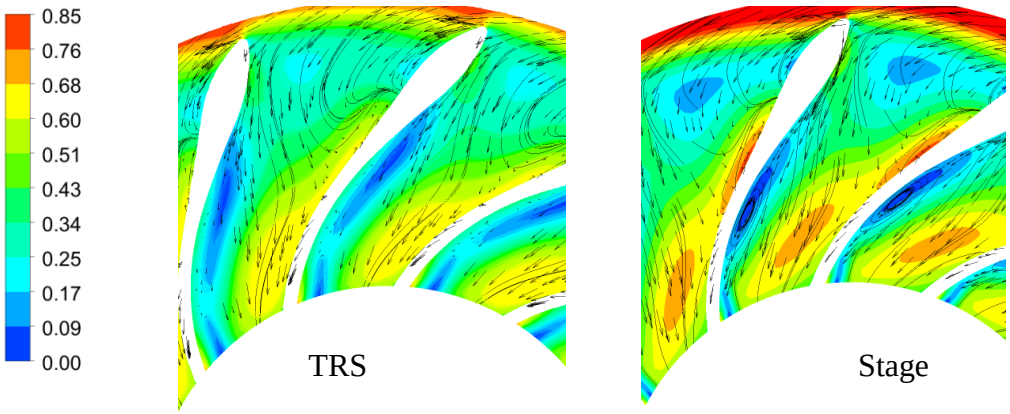

Figure 5-20 : Comparison of normalized time-averaged velocity field and 2D velocity streamlines at no-load condition between medium head-TRS (left) and medium head-stage (right) simulations for a gva 16° on the plane z/L = -0.4 crossing the runner

Figures 5-21 and 22 compare time-averaged pressure distribution on both sides of a blade between unsteady TRS and stage simulations. It can be appreciated that the same pattern of pressure has been predicted on both sides of the blade for both simulations. Table 5-5 compares the maximum and time-average pressure on both sides of the blade. It can be observed that the maximum pressure occurs on the suction side. Additionally, this table shows considerable pressure differences between TRS and stage simulations, which can be attributed to the difference in the velocity field in the runner passage. For instance, the stage simulation predicts a maximum pressure which is 18% larger than the TRS prediction. Furthermore, for stage simulations, the average pressure on pressure and suction sides are 39 % and 27% less than that in the TRS simulation, respectively.

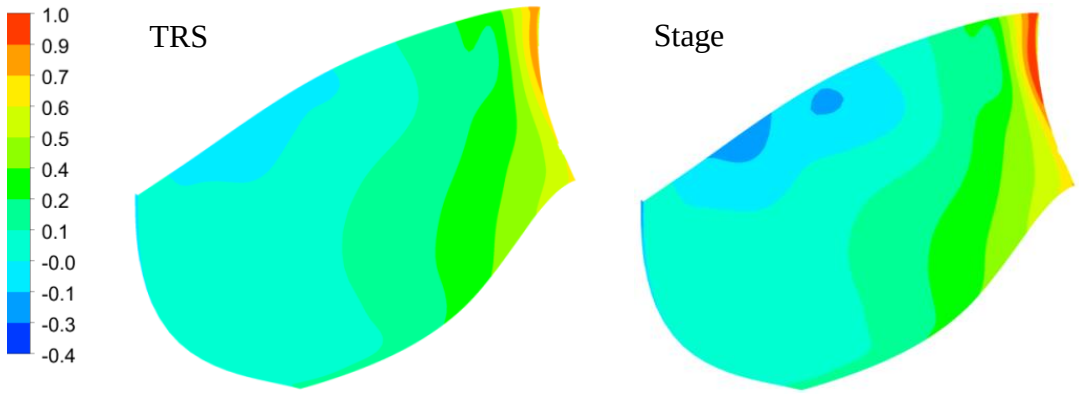

Figure 5-21 : Comparison of normalized time-averaged pressure distribution on the blade suction side at no-load condition between medium head-TRS (left) and medium head-stage (right) simulations for a gva 16°

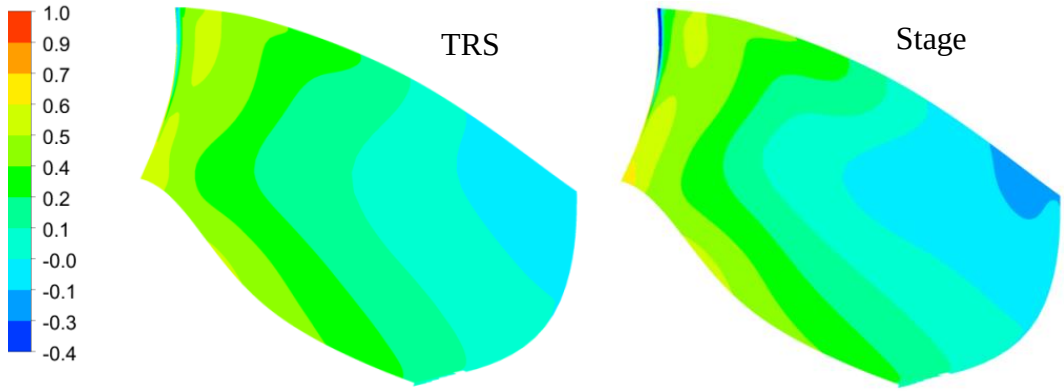

Figure 5-22 : Comparison of normalized time-averaged pressure distribution on the blade pressure side at no-load condition between medium head-TRS (left) and medium head-stage (right) simulations for a gva 16°

Table 5-5 : Comparison of averaged and maximum pressure at no-load between medium head-TRS & stage simulations for a gva 16°

	Average pressure		Maximum pressure	
	Suction side	Pressure side	Suction side	Pressure side
Medium head- stage	0.05	0.07	1.17	1.00
Medium head-TRS	0.06	0.12	0.99	0.82
Discrepancy (%)	-27	-39	18	22

Figure 5-23 illustrates the time-average velocity contours and surface streamlines in the plane section of the draft tube. In Figure 5-23, both simulations predict a major rear-corner vortex. This vortex corresponds to a strong separation of the discharge flow inside the draft tube, shown in Figure 5-18(right). In general, TRS and stage display similar flow patterns in the draft tube at no-load condition.

Analysis of the flow behavior shows that both simulations mostly give a similar prediction in the computational domain. However, there are differences in the velocity fields in the runner passages that cause large discrepancies in the average and maximum pressure on the blade between TRS and stage simulations. Unfortunately, these simulation results of pressure fluctuations could not be validated through comparison with experimental observations, for lack of available experimental data.

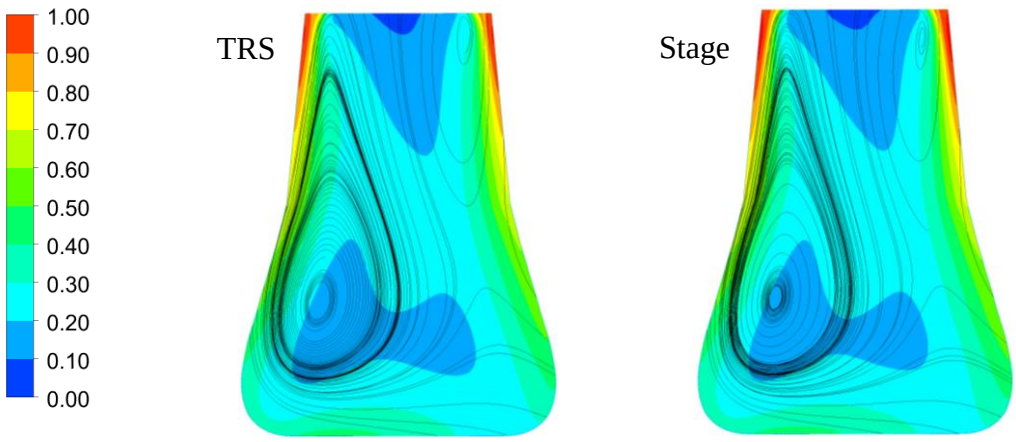

Figure 5-23 : Comparison of normalized time-averaged velocity field and 2D velocity streamlines at no-load condition between medium head-TRS (left) and medium head-stage (right) simulations for a gva 16° at a plane crossing the draft tube

5.6 Conclusion

Two unsteady flow simulation methodologies have been applied to simulate the operation of Francis turbines at no-load conditions. In the calculations, the flow solver was integrated with a user subroutine for computing and returning the value of angular velocity, time step and friction torque.

An important outcome of the present study was the comparison of unsteady no-load simulations using stage and transient rotor-stator interface models (TRS). These simulations were performed to predict the variation of engineering quantities, no-load curves, flow physics and unsteady pressure on runner blades during no-load condition.

Unsteady TRS and stage simulations showed similar trends for all runner parameters during the no-load process. Medium and high head stage and TRS simulations for a gva 16° predicted that the runner speed reaches about 170% of the synchronous speed in about 15 seconds. Furthermore, these showed that torque sharply drops and approaches near zero value, while oscillating. TRS simulations predict more oscillation during the transient process.

In addition, TRS and stage simulations were evaluated and validated by computing the engineering quantities at different gva. The comparison between CFD results and experiments showed that TRS and stage predicted similar speed factors in the gva range 20° to 26° for a high

head Francis turbine. The maximum error was 3.69% in stage simulation gva 15°. For the medium head Francis turbine, the TRS simulation results were more accurate than stage simulations in the gva range 11.5° to 22°. The maximum error was calculated as 5.98% for a gva 22° using stage simulations.

The stage simulations predicted the discharge factors more accurately than the TRS simulations at gva from 20° to 26° for the high head turbine. The maximum error was observed at the gva 15° for both TRS and stage simulations. For the medium head Francis turbine, the stage simulations are more accurate in gva range from 13.5° to 22°. The maximum error of 8.9% in the computation of the discharge factor was obtained at gva 11.5° using the stage simulation.

The unsteady TRS simulations required high computational effort to reach a solution, which constitutes a major challenge in a design process. For instance, TRS simulations for the medium head Francis required 6 times more simulation time than the stage calculations to converge at guide vane angle of 16° on the same computer cluster and same number of CPU cores.

A second outcome of this work was the analysis the flow behavior inside a Francis turbine at no-load. Both unsteady methods successfully predicted the evolution of engineering quantities such as runner torque, discharge and angular speed. These simulations revealed the presence of complex flow physics inside the runner at no-load. For instance, strong vortices near the leading edge block the runner inlet flow. Also, strong tangential flow at the runner outlet and axial reversed flow in the draft tube cone center leads to a vortex breakdown.

Analysis of flow in the runner domain shows that TRS and stage simulations yielded observable differences in the velocity fields in the runner passages. There were, for instance, sizeable differences in the average and maximum pressure on the blade between TRS and stage simulations. In the medium head-stage simulation for a gva 16°, the maximum and average pressure magnitudes were 18% larger on the suction side and -39% less on the pressure side than that in TRS simulation, respectively.

Fourier analyses of pressure fluctuations on the blade showed that the peak amplitude occurs on the suction side for both TRS and stage simulations. The value of the peak amplitude predicted by the stage method was, however, 2.33 times larger than that predicted by the TRS method. In general, simulations indicated considerable difference between TRS and stage in calculating the

pressure fluctuation on the blades. Unfortunately, no experimental measurements were available to validate these simulation results.

In summary, the proposed methodologies using transient rotor-stator and stage interface models successfully predicted the evolution of the rotational speed during the no-load condition which could contribute to improve runner design by allowing considering transient behavior. Moreover, better insight of complex phenomena inside the runner was obtained during runaway and no-load conditions. It has been observed that the unsteady simulations with a stage interface were not capable of predicting several details pertaining to flow physics, and pressure fluctuations during transient processes. Moreover, a sizeable difference was computed in the average and maximum pressure on the blades. Nevertheless, the main challenge of unsteady simulations with the TRS model was its significantly higher computational costs. While simulation results have demonstrated consistency in the prediction of the speed coefficient at no-load, important discrepancies remain in the prediction of the flow discharge coefficient. Further research involving significantly finer meshes and time steps, and considering more advanced turbulence models would be in order in trying to close this prediction gap.

ACKNOWLEDGMENT

The authors would like to thank the National Science and Engineering Research Council of Canada (NSERC) for its support of this research, under project RDCPJ 441752-12.

CHAPTER 6 ARTICLE 3: UNSTEADY SIMULATION FOR FRANCIS TURBINE DURING LOAD REJECTION EVENTS

Hossein Hosseinimanesh[1], Christophe Devals[2], Bernd Nennemann[3], Marcelo Reggio[1] and François Guibault[2]

[1]Department of Mechanical Engineering, École Polytechnique de Montréal

CP 6079, succ. Centre-ville, Montréal, QC, H3C 3A7, Canada, hossein.hosseinimanesh@polymtl.ca

[2]Department of Computer Engineering, École Polytechnique de Montréal

CP 6079, succ. Centre-ville, Montréal, QC, H3C 3A7, Canada, christophe.devals@polymtl.ca, francois.guibault@polymtl.ca

[3]Andritz Hydro Canada Inc.

6100 Transcanadienne, Pointe-Claire, QC, H9R 1B9, Canada, bernd.nennemann@andritz.com

6.1 Presentation of the article

In this chapter, the unsteady simulation of the no load condition is extended for modelling of the load rejection. To reach this objective, the runner acceleration, and closing of guide vanes were modelled simultaneously. These simulations allowed computing the evolution of engineering quantities such as turbine angular speed, flow physics and unsteady load on blades during the load rejection. This article was accepted to publish in the ASME 2016 FEDSM Fluid Engineering Division Summer Meeting on March 21st 2016 as:

Hosseinimanesh, H., Devals, C., Nennemann, B., Reggio, M., and Guibault, F., 2016, "Unsteady simulation for Francis turbine during load rejection events," Proc. Fluids Engineering Division Summer Meeting, ASME.

6.2 Abstract

This paper presents an automated tool chain for simulating Francis turbine behavior during the transient processes induced by a load rejection event. The proposed methodology combines a commercial CFD solver and a user function and scripts to address the simulation challenges caused by the wicket gate motion and runner speed variation during emergency shutdown. Mesh deformation and re-meshing techniques are used to simulate the large displacement of the wicket gates. The runner speed variation is computed using an angular momentum equation implemented in a user defined function. The proposed methodology was developed and validated by performing 2D unsteady simulations on a high head model Francis turbine used in the Francis-99 workshop, followed by a 3D unsteady simulations on a medium head Francis turbine. These simulations allow computing the evolution of engineering quantities such as turbine angular speed, flow physics and unsteady load on blades during the process. The validation of CFD results with experiments showed 9% discrepancy in the prediction of runaway speed. The investigation of flow physics reveals the presence of complex flow structures such as reversed flow (pumping flow) near the draft tube cone center and a downward tangential flow near the cone wall of the draft tube. Pressure fluctuations are captured when the Francis turbine operating point moves through conditions of zero and negative torque. The proposed methodology was encouraging in terms of providing a qualitative analysis of the flow physics and the turbine behavior during load rejection.

6.3 Introduction

Integration of intermittent renewable energy sources such as photovoltaic cells and wind turbines leads to increased instability of traditional electrical grids. Therefore, hydropower plants are nowadays operated in more flexible ways in order to ensure the stability of the electrical grids. In addition, hydropower plants are now exposed more frequently to transient processes: machine shutdown, start-up and regime modification. Irregular transient processes such as load rejection and runaway may also occur. Transient processes produce complex vortical flow structures inside turbines which induce pressure fluctuations and dynamic stresses. These conditions may influence the mechanical safety of hydraulic machines. In this context, further research is

required to improve turbomachinery designs to reduce the impact of off-design conditions and transient processes.

In hydropower plants, load rejection is a harmful transient processes that happens when the generator is disconnected from the network because grid parameters change beyond the generators prescribed range (Trivedi, 2014). If mismanaged, such an event may lead to serious damage to the hydraulic turbine. During the event, the governor system of the turbine rapidly takes actions to prevent the runner rotational speed from reaching an excessive value, by closing the wicket gates. Nevertheless, the rapid closing of the wicket gates may lead to pressure waves, which move forward and backward through the entire water passage. An emergency closure sequence must therefore be defined in order to shut down the machine with minimal damage.

In recent years, transient measurements have been performed to analyze the performance of hydraulic turbines on sites or in labs with prototypes and model test turbines, respectively. For instance, Trivedi et al. (Trivedi et al., 2015; Trivedi et al., 2014; Trivedi et al., 2014; Trivedi et al., 2014) performed transient pressure measurements in a high head turbine during start-up, shut-down, load variations, load rejections, and spin-no-load covering the entire range of the prototype turbine operation. These experimental measurements of transient processes on full-scale turbines may be damaging and expensive since they induce strong unsteady loads on turbine components. In addition, the model testing techniques may result in large scaling errors when the pressure fluctuations are transformed from model tests to prototypes over the extended operating range (Trivedi, 2014).

Over the past decade, increase in the computational capacity and advancements in numerical techniques have allowed to simulate hydraulic turbines during transient processes using computational fluid dynamics (CFD). In contrast to experiments, CFD simulations have demonstrated more flexibility and capacity in modeling complex 3D geometries with various boundary conditions (Hosseinimanesh, Devals, Nennemann, & Guibault, 2015). Nevertheless, the majority of CFD simulations have focused on pump-turbines in order to predict the characteristic instability in the S-shaped region of the characteristic curve as well as the radial force imbalance on the turbine due to rotating stall, for instance see (Staubli et al., 2008; Widmer et al., 2011). Limited studies have been devoted to investigating Francis turbines during load rejection events. Nennemann et al. (B. Nennemann et al., 2014) mention that no studies have so far been published

on the prediction of the stochastic loads acting on the blades or other parts of radial turbines during part load or no load operations.

The modeling of wicket gate closing during load rejection simulations constitutes an important challenge due to the complex geometry to mesh and physics to represent. In order to develop an efficient, low cost computational methodology, fixed boundary conditions, based on the hypothesis of frozen hydraulic conditions, were used for the simulation of load rejection events by Côté et al. (Côté et al., 2014). In their work, the authors did not provide a detailed analysis of results such as unsteady loads on blades.

In addition, some research involved the use of the dynamic mesh (Huang et al., 2012; J Li et al., 2010). However, few details have been given about the results and numerical methods. Generally, no comprehensive study has studied the performance of the Francis turbine during load rejection by modeling the movement of guide vanes. Developing a new efficient and robust algorithm to simulate Francis turbine during load rejection events will provide much new needed insight into this complex phenomenon.

In the present paper, an unsteady methodology, applied for simulating Francis turbines during runaway transient (Hosseinimanesh, Devals, Nennemann, & Guibault, 2015) is extended in order to model load rejection events. In this regard, the movement of the wicket gates is modeled during the transient process in addition to the runner's acceleration. The proposed method is developed and verified by 2D unsteady simulations. Moreover, 3D simulations are applied for the validation of the method.

This paper is organized in three sections. Section 1 presents the studied cases, numerical set up, and the turbulence model. In addition, the main methodology and equations employed in the load rejection simulation are also introduced in this section. In section 2, the results of 3D simulations of a medium head Francis turbine are presented and compared with experiments. Section 2 also investigates pressure loads on blades and the complex flow physics inside the turbine. Finally, section 3 presents some conclusions and closing remarks.

6.4 Computational aspect

6.4.1 Studied cases

The proposed methodology is developed and verified by performing 2D unsteady simulations on a high head model Francis turbine used in the Francis-99 workshop followed by 3D unsteady simulations on a medium head Francis turbine, respectively. Table 6-1 shows the summary of turbine features, as well as the mesh information used for unsteady simulations.

In Table 6-1, the high head Francis turbine includes a distributor with 14 stay vanes and 28 wicket gates, and a runner with 30 blades. The medium head Francis turbine is integrated with a runner having 13 blades, a distributor with 20 stay vanes and 20 wicket gates, and an elbow-type draft tube.

For the first case, the computational domain involves one distributor passage, including one-stay vane (1/14) and two wicket gates (2/28), and one runner passage (1/30), as shown in Figure 6-1. In the second case, 3D unsteady simulations are performed in a domain involving one stay vane (1/20), one wicket gate (1/20), a single runner channel (1/13) and the full draft tube, as shown in Figure 6-2. In the present paper, the unsteady simulations of the first and second cases are called Francis-99 and 3D-medium head simulations, respectively.

Meshes of the components are generated using mesh generation tools developed jointly by Andritz and Polytechnique Montréal for different wicket gate angles. For 2D simulations, Multi-block-structured meshes are used for all components. For 3D simulations, Multi-block-structured meshes are used for the runner passage and draft tube, and hybrid meshes in a single domain are used for the wicket gate and stay vane passage. Mesh quality was successfully verified in several steady-state and unsteady simulations in (Hosseinimanesh et al., 2014) for no-load speed and runaway simulations.

Figure 6-1: Computational domain of high head model Francis turbine (Francis-99) in 2D unsteady simulations

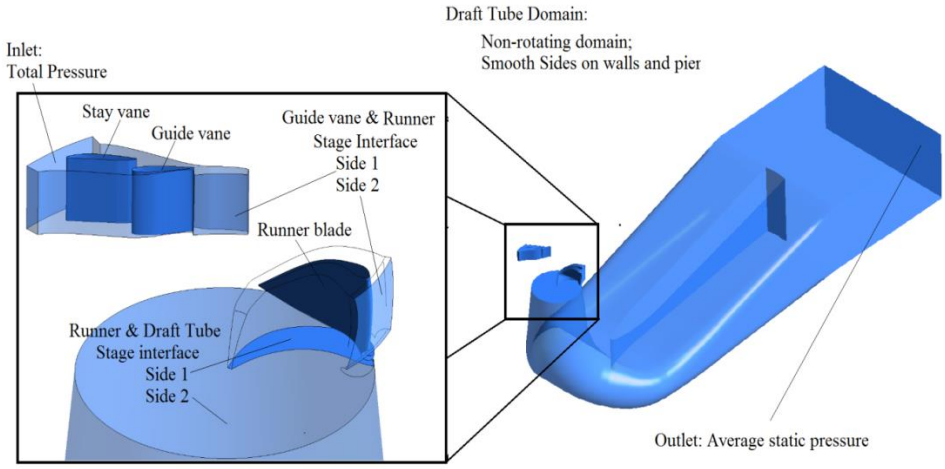

Figure 6-2: Geometry and boundary conditions of computational domains in 3D-medium head simulation

Table 6-1: Turbine specifications at load rejection simulations

								Number of nodes			
Case	Type				Number of components			Stay vane & wicket gate	Runner blade	Draft tube	
	Francis Turbine	Wicket gate movement		Interface model	blade	wicket gate	stay vane	Hexahedra & prisms		Hexahedra	Total nodes
1	High head model	4°-24°	2D model	stage	1/30	2/28	1/14	19k	29k (Hexahedra & prisms)	---	48k
2	Medium head prototype	3°-30°	3D prototype	stage	1/13	1/20	1/20	166k	144k (Hexahedra)	1300k	1610k

6.4.2 Numerical set up

In the present study, a load rejection event is simulated by solving the unsteady Reynolds averaged Navier-Stokes equation for incompressible flow at different operating conditions using the Ansys-CFX 16.1 commercial solver. The standard *k-ε* turbulence model is used for handling turbulence. The momentum equations and turbulent advection equations have been discretized using the high-resolution scheme and first-order scheme respectively, with convergence tolerances of all main primitive variables set to 1E-05 on the root mean square (RMS) residuals. Besides, the quantities of torque, runner angular speed and inlet flow rate are followed during simulation. Unsteady simulations are performed using the second-order backward Euler scheme to approximate the transient term in the Navier-Stokes equations.

The standard *k-ε* model uses the scalable wall function approach to improve the accuracy and robustness near the wall. The value of y^+ was assessed by the authors in (Hosseinimanesh, Devals, Nennemann, Reggio, et al., 2015) for similar unsteady simulations. For all simulations, the inlet boundary condition is set to the total pressure associated with the turbine net head. The outlet boundary condition is specified as zero-averaged static pressure. No-slip boundary conditions are imposed on all solid walls. Figure 6-2 presents the geometry and boundary conditions for the 3D medium head simulations. Moreover, both cases use the stage interface model for connecting the runner and distributor passage, and the runner and draft tube, modeled in distinct frames of reference. The stage model performs circumferential averaging of the fluxes at the interface ("ANSYS CFX-User manual,").

6.4.3 Load rejection simulation methodology

The runner acceleration and closing of wicket gates have been modeled simultaneously to simulate Francis turbine operation during load rejection.

6.4.3.1 Runner acceleration

The runner acceleration has been calculated during the load rejection simulation based on the method described in (Hosseinimanesh, Devals, Nennemann, & Guibault, 2015). The proposed methodology uses the angular momentum equation for the rotating mass to estimate the turbine

speed during the process. At each time step, the angular speed of the turbine is updated using equation (6.1).

$$\omega_{R,n} = \omega_{R,n-1} + \frac{T_n \Delta t}{I_z} \tag{6-1}$$

where T denotes the turbine torque (Nm), I_z is the moment of inertia of the runner (kg.m^2), and $\omega_{R,n}$ is the runner angular speed (rad/s) at time position n. In Eq.(6-1), Δt represents a time step that is adjusted automatically due to the runner angular speed variation during the transient process. In the simulations performed here, the time step was computed to correspond to a 4° angular variation of the turbine at each iteration. Further details on the simulation of runner acceleration have been mentioned in (Hosseinimanesh, Devals, Nennemann, & Guibault, 2015).

6.4.3.2 Wicket gate movement

Mesh deformation and re-meshing techniques were used to simulate the wicket gate closing. Figure 6-3 shows a closing scenario of the medium head Francis turbine. The wicket gate displacement was 30° in almost 10 sec.

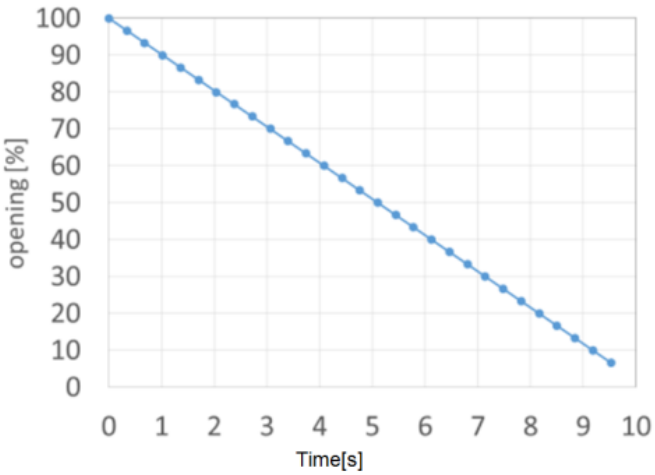

Figure 6-3 : Wicket gate closing scenario for 3D medium head Francis simulations

In the present study, we aimed to simulate the entire movement of the wicket gates using mesh deformation. Nonetheless, mesh deformation greater than 1° led to fatal error conditions and

simulation termination due to the degradation of mesh quality. Therefore, we also used re-meshing techniques in addition to the mesh deformation of 1°.

In this way, the displacement which is known beforehand, shown in Figure 6-3, is split up into regions where the wicket gate motion is specified as a movement less than 1°. Then, sequences of key-frame meshes corresponding to these regions are generated. Afterward, a re-meshing loop was integrated into the general simulation workflow to update the current simulation mesh using key-frame meshes. Figure 6-4 shows a schematic illustration of the methodology developed.

In Figure 6-4 , the wicket gate movement is performed automatically by execution of two scripts. At first, script 1 generates key-frame meshes placed in a location that is accessible during the analysis execution by the re-meshing loop. Then script 2 starts the re-meshing loop.

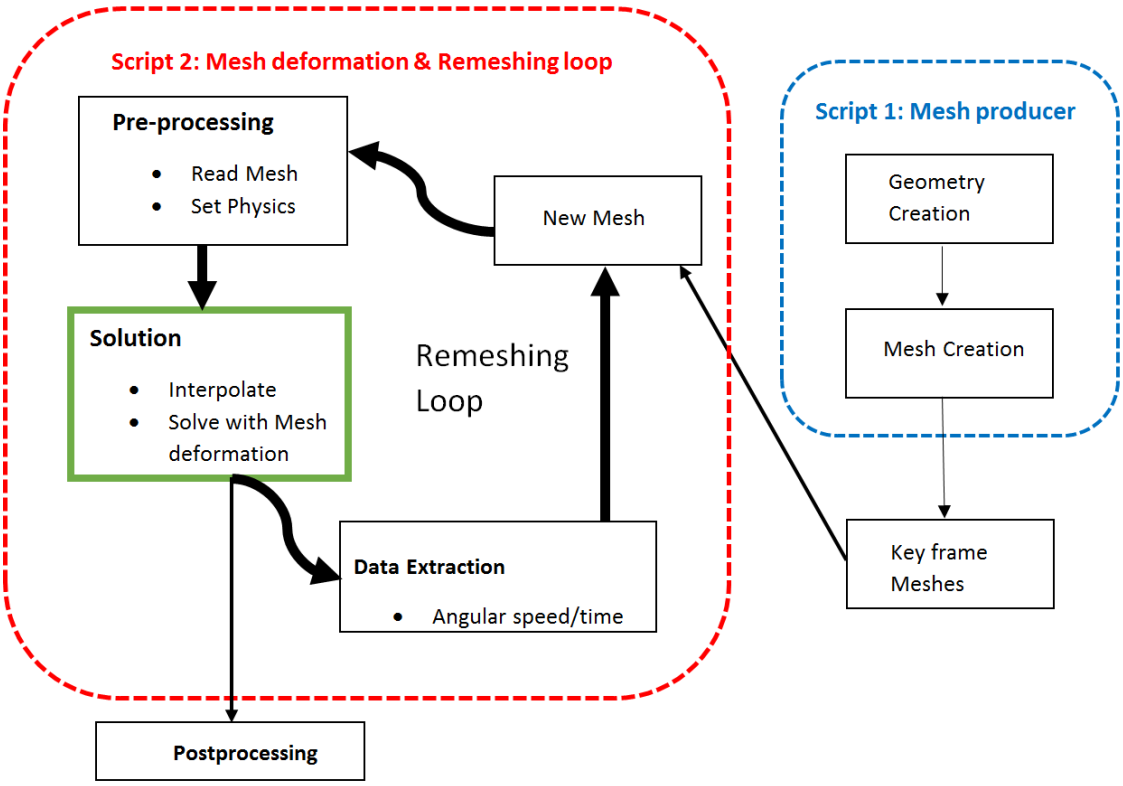

Figure 6-4 : Schematic illustration of the wicket gate closing simulation

The re-meshing loop involves two steps: data extraction and mesh modification, in addition to the standard simulation workflow with 1° mesh deformation. In this way, the data, needed to guide the geometry modification and update the mesh is extracted from the most recent analysis results

and monitoring point values. Next, the new mesh that corresponds to the time step, is imported to update the mesh from the file of key-frame meshes. Then the new mesh is inserted into the analysis definition, and produces an updated CFD-input file. In the next step, the previously generated analysis results are interpolated onto the new mesh and the solution process is continued.

6.4.3.2.1 Mesh motion modeling

As described in the previous section, an important component of the simulation of the closing wicket gates is the mesh deformation. This is imposed on the nodes on the boundaries and sub-regions of the mesh in the distributor channel during the solution process. Figure 6-5 shows the mesh motion options that were set on the subdomains and boundary regions, respectively.

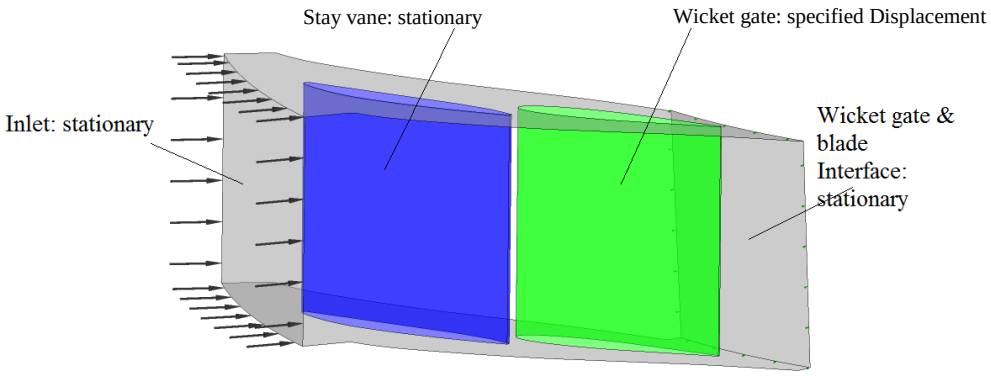

Figure 6-5 : Mesh motion conditions of the wicket gate passage

In Figure 6-5, the inlet, stay vane and interface between the distributor and runner are set as stationary. Furthermore, conservative interface flux and specified displacement are used on one-to-one periodic interfaces and wicket gates, respectively. The motion on nodes of the wicket gate region is determined by the following equation in a CEL[9]

$$L_{WG} = \omega \, t \, r_{axis} \tag{6-2}$$

[9] CFX Expression Language.

Where L_{WG} shows the arc length (m), ω is the angular speed (rad/sec), t is the simulation time (s), and r_{axis} is the radius about the local rotation axis (m) of the wicket gate.

In addition, the motion of all remaining nodes is determined by the mesh motion model ("ANSYS CFX-User manual,") which is the displacement diffusion. The model diffuses the displacement applied on domain boundaries or subdomains to other points by solving the equation:

$$\nabla.\left(\Gamma_{disp}\nabla\delta\right) = 0 \tag{6-3}.$$

Where δ denotes the displacement related to the previous mesh locations and Γ_{disp} indicates the mesh stiffness, which controls the degree to which areas of nodes move together. Equation (6-3) is solved at the start of each time step for transient simulations. In addition, Γ_{disp} is determined to increase near certain boundaries (wall, inlet, and outlet) to preserve the mesh distribution and quality using the following equation ("ANSYS CFX-User manual,"):

$$\Gamma_{disp} = \left(\frac{L_{ref}}{d}\right)^{C_{stiff}} \tag{6-4}.$$

In Eq. (6-4), d indicates the distance from the nearest boundary, L_{ref} the reference length, which is set to 1 (m), and C_{stiff} , the stiffness model exponent that controls how quickly this increase happens, which is set to 12.

6.5 Results

In this section, the 3D simulation results are presented and compared to the experimental data. The 2D simulations were used only for developing purpose since they represent a crude approximation of the real flow physics.

6.5.1 Engineering parameters

In Figure 6-6, the normalized angular speed, computed for the 3D medium head simulations, is validated by comparison with experiments. It is noted that simulations and experiments show similar trends of the variation of the runner speed during the transient process. In Figure 6-6, it can be seen that the runner accelerates sharply at the beginning of the simulation due to the load rejection. The speed growth rate decreases at 6 sec, when the wicket gate is closed by 60%.

Finally, the runner speed starts to decrease. In Figure 6-6, points D_1 and D_2 indicate the maximum speed attained by turbine during the load rejection in the measurement and CFD simulation. The discrepancy between the measurement and CFD simulation is 9% at the prediction of the maximum speed.

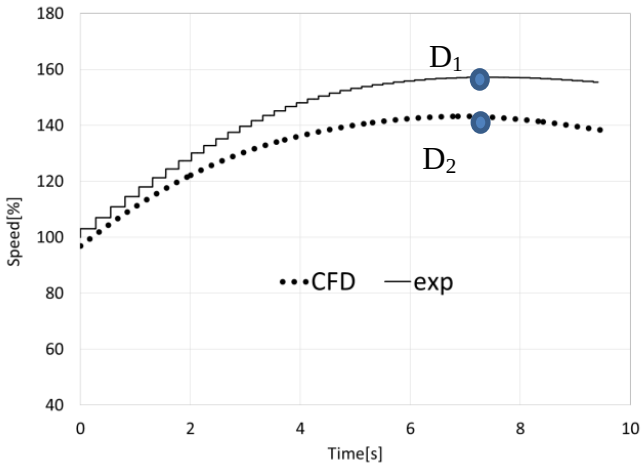

Figure 6-6 : Variation of the normalized runner angular speed in 3D medium head simulations and experiment

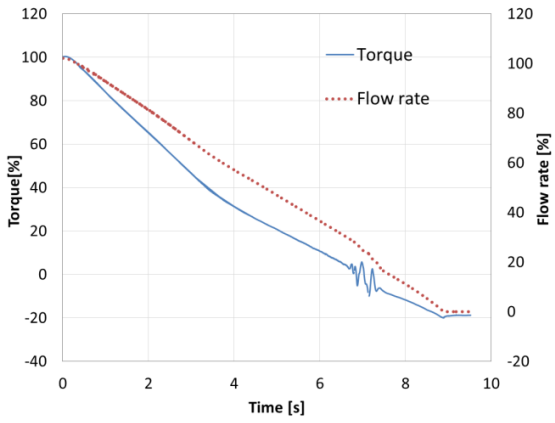

Figure 6-7 : Variation of the normalized runner torque and flow rate during load rejection in 3D medium head simulation

Figure 6-7 presents the evolution of two normalized turbine parameters, the turbine torque T^* (T/T_1) and flow rate Q^* (Q/Q_1) during load-rejection for the 3D medium head simulation. T_1 and

Q_1 indicate the value of torque and discharge at the simulation start, respectively. Figure 6-7 shows that the torque and flow rate decrease and converge to -20% and 0%, respectively. The closure of wicket gates reduces the inlet flow rate and the turbine torque. The rate of torque decrease is higher at the start of the simulation for the first 4 sec. Figure 6-7 shows that the turbine enters a condition of zero or negative torque at around 7 sec. while torque fluctuations may be observed. The fluctuations are induced by the unsteady flow physics inside the runner and draft tube.

6.5.2 Pressure

Pressure is obtained by CFD simulations at six monitoring points which are located on the middle of the pressure and suction sides of the runner blade, shown in Figure 6-8. Figures 6-9 and 6-10 show the evolution of the normalized pressure signals (P/P^*) during the load rejection event for the 3D medium head simulation. P^* is calculated by:

$$P^* = \rho g H \qquad (6\text{-}5).$$

Where, ρ is the water density (kg/m^3), g is standard gravity (m/s^2), and H is the turbine net head (m).

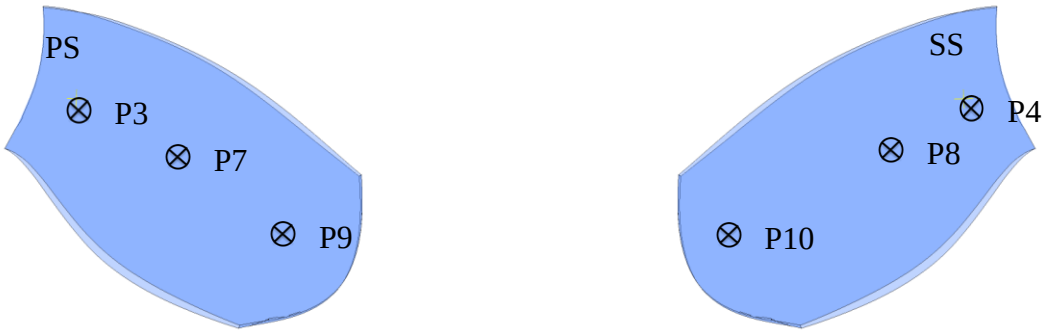

Figure 6-8: Monitoring points on pressure (PS) and suction (SS) sides of blade in medium head-TRS & stage simulations

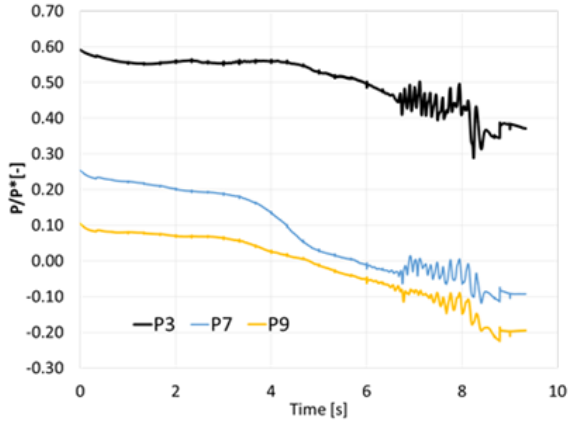

Figure 6-9: Time history of normalized pressure at monitoring points on the pressure side

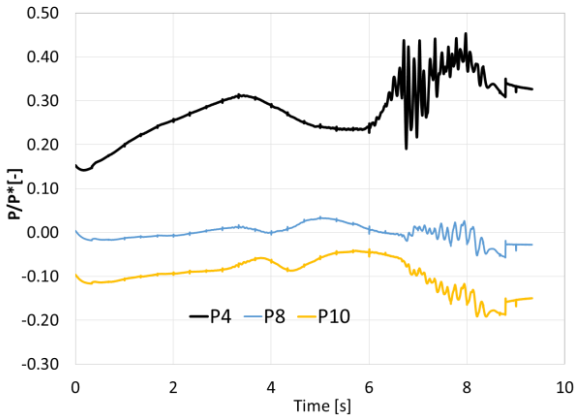

Figure 6-10: Time history of normalized pressure at monitoring points on the suction side

Figure 6-9 shows that pressure signals experience similar drops at P3, P7 and P9, which are located on the leading edge, middle and trailing edge on the pressure side.

On the suction side in Figure 6-10, the pressure at P4, located near the leading edge, increases while the pressure at P8 and P10 are almost constant. In Figures 9 and 10, strong pressure fluctuations with large amplitude are observed on both the pressure and suction sides between 6 sec. and 8.5 sec. Fluctuations start when the turbine moves through conditions of zero and negative torque, shown in Figure 6-7.

The fast Fourier transforms of pressure signals at P3, P4, P9, and P10 obtained from CFD simulations and experimental measurements between 6 sec and 8.5 sec are shown in Figures 6-11 and 6-12. The pressure sensors in the experimental measurements have the same locations as the monitoring points on the runner, shown in Figure 6-8. Fourier transforms show that the strong pressure signals are present at the leading edge. The comparison of frequency and amplitude of

the peak signals A and B at the leading edge, shown in Figures 6-11 and 6-12, indicates a discrepancy between CFD and experiments. In addition, the CFD method is not consistent for the prediction of the amplitudes of peak signals. For instance, on the pressure side, the amplitude of peak signal of CFD A is greater than the peak signal of measurements B and vice versa on the suction side. In Figures 6-11 and 6-12, The CFD simulations predict fluctuations in a much lower frequency range than measurements.

The uncertainty of CFD results for the prediction of the pressure fluctuations may be related to the influence of the stage interface and standard k-ε turbulence models. The stage model neglects some transient effects because it performs a circumferential averaging of the fluxes at the interface between the runner and the wicket gate. Moreover, the standard *k-ε* turbulence model is not able to predict all aspects of the flow at no-load conditions with full accuracy (B. Nennemann et al., 2014). Nevertheless, in the interest of developing a fast and simple method, these models appear to be appropriate and time economical.

Figure 6-13 illustrates the evolution of normalized pressure distribution on both sides of a blade during load rejection for the 3D medium head simulation. In Figure 6-13 there is a fast decrease of the pressure on the pressure side, starting near the trailing edge. At the same time, the pressure on the suction side increases near the leading edge. At 6.5 sec, the pressure distribution on pressure and suction sides has approximately the same pattern that results in the balance of average pressure forces. Therefore, average turbine torque becomes almost zero, as shown in Figure 6-7. Then the pressure decreases further on the pressure side near the trailing edge and hub. In addition, the pressure increases on the entire suction side, except in the area near the trailing edge and hub. This pressure, larger on the suction side than on the pressure side, causes a negative turbine torque between 6.5 sec and the end of the simulation.

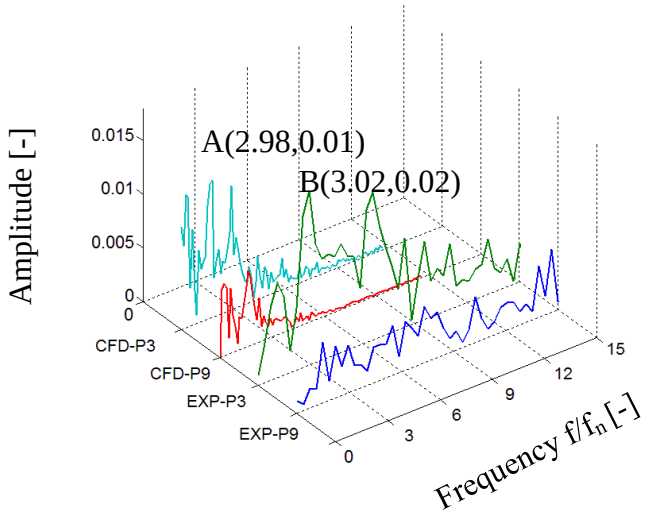

Figure 6-11: Spectral analysis of normalized pressure fluctuation at monitoring points on the pressure side (f_n: frequency of runner rotation at best efficiency operating point)

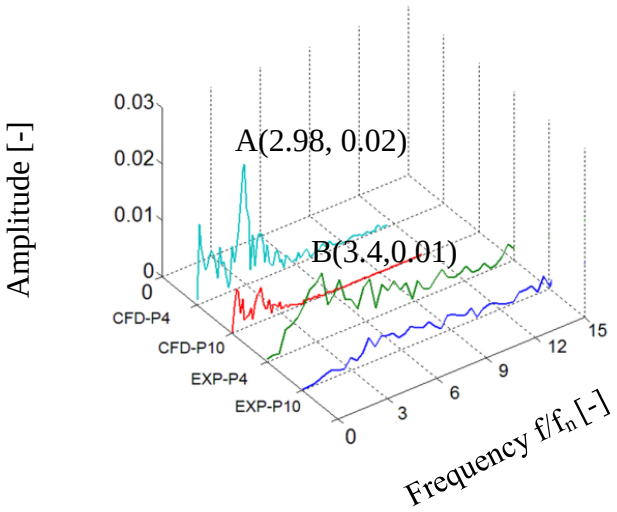

Figure 6-12: Spectral analysis of normalized pressure fluctuation at monitoring points on the suction side (f_n: frequency of runner rotation at best efficiency operating point)

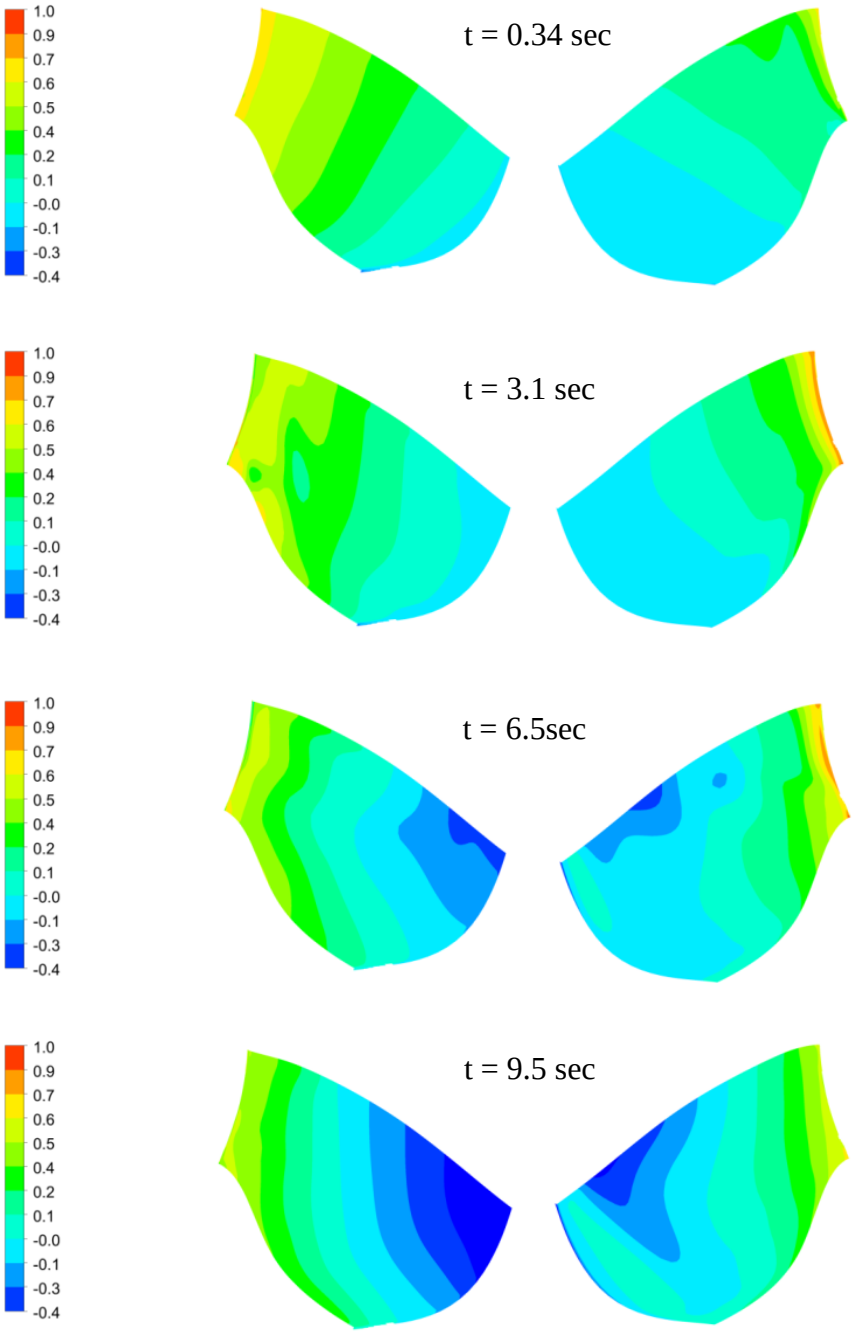

Figure 6-13: Evolution of normalized pressure distribution on the blade pressure (left) and suction (right) sides during load rejection from 3D medium head simulation

6.5.3 Flow physics during load rejection

Figure 6-14 shows the evolution of flow swirl S during load rejection at the draft tube inlet. Swirl is calculated by the following equation (Anand et al., 1993)

$$S = \frac{\int_0^{R_o} \rho UWrdr}{R_0 \int_0^{R_o} U^2 rdr} \quad (6\text{-}6).$$

Where U and W indicate tangential and axial velocity profiles along the draft tube inlet, respectively, R_0 denotes the maximum radius at the outlet, while r indicates the radius. In Figure 6-14, the swirl value increases sharply at the start of the simulation, and finally decreases slightly, and becomes flat after 6 sec. It is important to note that the swirl grows by 8 times its initial value during load rejection, which indicates a significant rise of angular momentum to axial momentum at draft tube inlet due to the closure of the wicket gates.

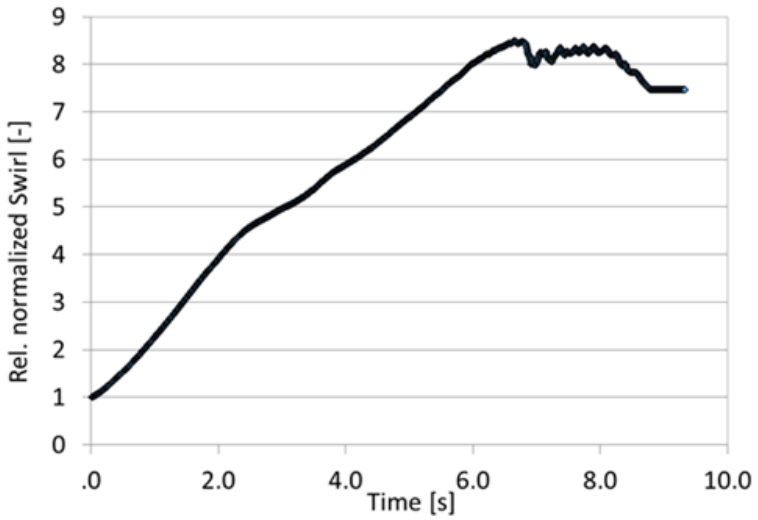

Figure 6-14 : Evolution of normalized swirl at draft tube inlet during load rejection simulation

Figures 6-15 and 6-16 display the distribution of normalized tangential and axial velocity in a plane section of the draft tube through the load rejection event. Figure 6-15a shows a low tangential flow in the draft tube cone at the start of the simulation. In contrast, Figure 6-15b and 15c show that the tangential flow increase near the cone wall after 5 sec. The 3D simulation

shows that the closing of wicket gates induces a low turbine inflow with high circumferential velocity. Consequently, it leads to a strong tangential flow at the draft tube cone wall.

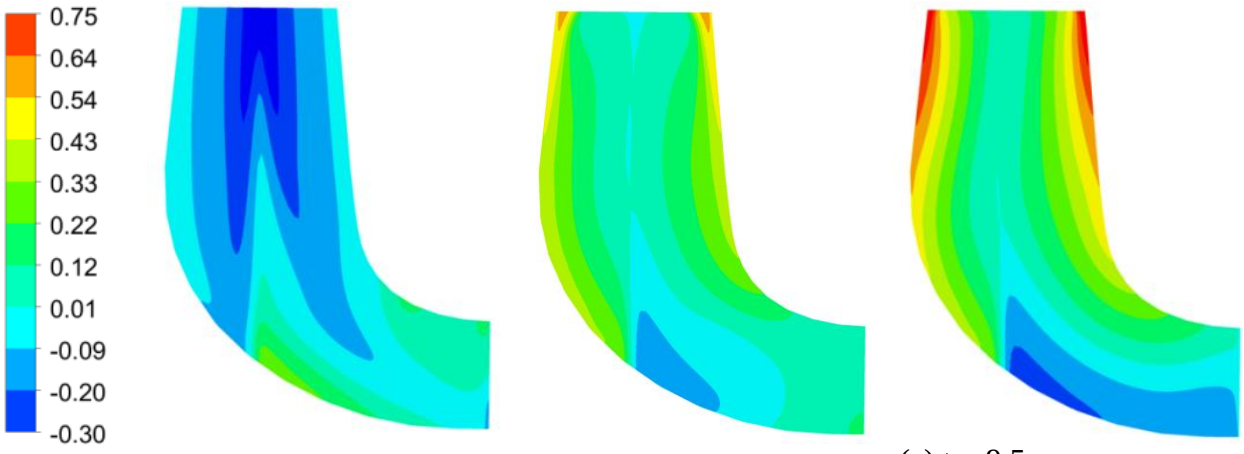

(a) t = 0.34 sec (b) t = 5.1 sec (c) t = 9.5 sec

Figure 6-15: Normalized tangential velocity field on a cross section through the draft tube during load-rejection from 3D medium head simulation

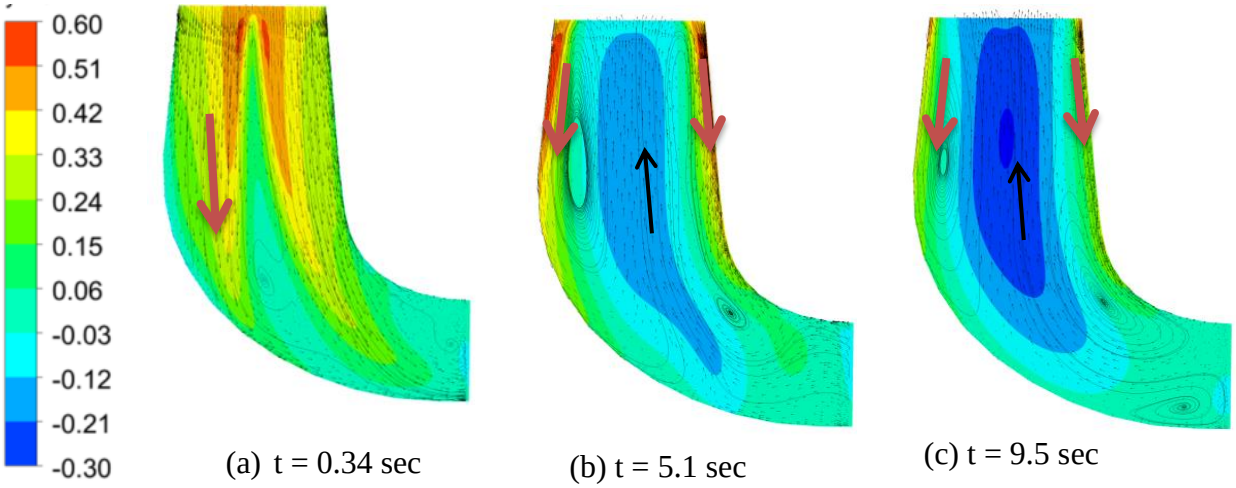

(a) t = 0.34 sec (b) t = 5.1 sec (c) t = 9.5 sec

Figure 6-16: Normalized axial velocity field on a cross section through the draft tube at no-load from 3D medium head simulation

Figure 6-16 shows that the overall flow still moves toward the draft tube outlet at the start of the load rejection simulation. During the process, the inflow inside the draft tube is separated into two concentric flow areas. As shown in Figures 6-16b and 16c the fluid moves downstream in the outer region near the wall. The high tangential flow at the runner outlet leads to a displacement of the flow towards the draft tube periphery. Consequently, a low pressure region is generated in the

center of the draft tube which drags the flow from the downstream creating the reversed flow. Figure 6-16b and 16c show a stagnation zone in the inner region which moves upstream toward the runner hub.

Overall, a major structural variation of the flow happens in the turbine and draft tube to dissipate the input hydraulic energy due to load rejection. The separation of the strong swirling flow inside the draft tube produces large-scale vortex structures as shown in Figure 6-16. Then, vortices may decay successively, and create a continuous range of smaller eddies that induce the pressure pulsation with higher frequencies. To predict more details of vortical flow and pressure fluctuations, 3D unsteady simulations on the complete turbine with more advanced turbulence models and finer mesh may be required.

6.6 Conclusion

The performance of Francis turbines during harmful transient conditions such as load rejection must be investigated to ensure the mechanical safety of hydraulic machines. In this respect, a methodology has been developed and validated by performing 2D and 3D unsteady CFD simulations. The main challenge was the modeling of the wicket gate closing due to the complex geometry, mesh and physics issues.

In the present paper, the detailed analysis of 3D CFD simulations provided more understanding and insight into the complex phenomenon inside the turbine during the load rejection. The CFD results show that the swirling flow increases 8 times at the draft tube inlet after 6 sec. Consequently, the strong swirling flow separates inside the draft tube, which produces large-scale vortex structures. Furthermore, CFD simulations predicted partial pumping in the cone center of draft tube. The complex flow structure induced the pressure fluctuations with a fairly wide range of frequencies.

The normalized pressure signals on the pressure and suction sides of the blade were evaluated during the load rejection. CFD results showed that all pressure signals experience a similar drop at monitoring points located on the leading edge, middle and trailing edge of pressure side. On the suction side, the pressure signals increased near the leading edge, but did not experience significant changes at the trailing edge and the middle of the blade.

Fourier transform of pressure fluctuations were compared with experimental measurements. The strong pressure signals are present at the leading edge for CFD and experiment. Nevertheless, there was a discrepancy between CFD simulations and experiments for the prediction of frequencies and amplitudes. The CFD simulations predict fluctuations in a much lower frequency range than measurements.

Furthermore, the evolution of engineering quantities during the process, such as torque, runner speed and inlet flow rate, were investigated. The torque and flow rate decreased and converged to -20% and 0%, respectively while the runner speed increased to 140% during load rejection. The validation of CFD results with experiments showed 9% discrepancy at the prediction of the maximum speed during load rejection.

The uncertainty of CFD results for the prediction of the pressure fluctuations may be related to the influence of the stage interface and the standard k-ε turbulence model and mesh quality. The stage model neglects some transient effects because it performs a circumferential averaging of the fluxes at the interface between the runner and the wicket gate. Moreover, the standard k-ε turbulence model, which is a RANS model, is not able to predict all aspects of the flow at no-load conditions with full accuracy (B. Nennemann et al., 2014).

Generally the proposed methodology was encouraging in terms of providing a qualitative analysis of the flow physics and the turbine behavior during load rejection. It appears that if the main interest is to develop a fast and simple method, these models are appropriate and time economical. Nevertheless, to predict more details of vortical flow and pressure fluctuations, 3D simulations on the complete turbine with more advanced turbulence models and very fine mesh may be required.

6.7 Acknowledgments

The authors would like to thank the National Science and Engineering Research Council of Canada (NSERC) for its support of this research, under project RDCPJ 441752-12.

CHAPTER 7 GENERAL DISCUSSION

The contribution of this thesis consists in the development and evaluation of methodologies for analyzing Francis turbine behavior during runaway and no-load conditions. The research presented the analysis of techniques for the calculation of the runaway speed and no-load speeds, which are important performance factors for the safe operation of hydropower systems, using steady and unsteady simulations. In addition, the no-load simulation methodology was extended to model Francis turbines during load rejection. This chapter aims to provide further evaluations on the most important outcomes of the study, and main challenges encountered in this thesis.

7.1 Comparison between steady and unsteady simulations of Francis turbines at no-load condition

The steady and unsteady simulations of no-load conditions are compared with regards to the calculation of engineering parameters, the flow behavior inside the turbine, unsteady pressure loads on the runner blades and computational costs. All steady simulations were performed on a single runner/distributor passage. The unsteady simulations were performed for two geometric configurations: the complete turbine, and a single runner/distributor passage. The transient-rotor stator (TRS) model was used for connecting the runner and distributor, and the runner and draft tube in the complete turbine. The stage interface model was used for connecting the runner and distributor passages, and the runner passage and draft tube. Finally, the load rejection simulation methodology is evaluated and compared with the no-load simulation methodology.

7.1.1 Engineering parameters: Speed factor and discharge factor

The no-load simulations have been performed and assessed on a medium and a high head Francis turbine for calculating the speed factor and discharge factor at no-load condition, as shown in Figures 4-3, 5-9 and 5-10. The speed, discharge and power factors were calculated using the formulation defined in (IEC60193, 1999-2011) as follows, respectively:

$$N_{ed} = \frac{ND_{th}}{60\sqrt{gH}} \quad (7\text{-}1).$$

$$Q_{ed} = \frac{Q}{{D_{th}}^2\sqrt{gH}} \quad (7\text{-}2).$$

$$P_{ed} = \frac{2\pi TN}{60g^{1.5}H^{1.5}\rho{D_{th}}^2} \quad (7\text{-}3).$$

with:

D_{th}: runner throat diameter [m];

g: gravitational acceleration, [m/s^2];

H: turbine net head, [m];

N: turbine rotational speed, [rpm];

Q: discharge, [m^3/s];

T: hydraulic force torque, [N.m];

ρ: fluid density, [kg/m^3]

For the medium head Francis turbine, the unsteady TRS simulation computed more accurate speed factors than steady and unsteady stage simulations for guide vane angles from 11.5° to 22°. The maximum discrepancy between CFD results and experimental data was computed as 5.98% and 5.65% for the steady and unsteady stage simulations, respectively at guide vane angle (gva) 22°. The unsteady TRS simulation result was nearly 2.5% more accurate compared to other simulation results at gva 22°.

Comparison of CFD results and experiments in the gva range between 20° and 26° of the high head Francis turbine showed that the unsteady stage and TRS simulations predicted similar speed factors. The maximum computed error was 3.42% and 3.65% for unsteady TRS and stage simulations, respectively, at gva 26°. In this range, the unsteady simulation results were nearly 1% more accurate compared to the steady simulations. At gva 15°, the steady simulation result was nearly 0.3% and 3% more accurate than unsteady TRS and stage simulations, respectively.

Unsteady TRS simulations were found to be more accurate than steady and unsteady stage simulations for computing the speed factor at many opening angles, except at a gva 15° of the high head Francis turbine.

No-load simulations were also validated by means of the discharge factor. For the medium head Francis turbine, the unsteady stage simulation results were nearly 6% and 0.5% more accurate than the unsteady TRS and steady simulation results for gva range 13.5° to 20°. At gva 11.5°, the unsteady TRS simulation computed the discharge factor nearly 6.6% better than the unsteady stage simulation. For the medium head Francis turbine, the unsteady stage simulation showed to be more accurate in the gva range of 13.5° to 20° for calculating the discharge factor, compared to other simulations.

For the high head Francis turbine, the unsteady stage simulations computed the discharge factor 2% and 3% more accurately compared to unsteady TRS simulations at guide vane angles 20° and 26°, respectively. The unsteady stage simulation result is 2% less accurate and 1.2% more accurate compared to steady simulations at guide vane angles 20° and 26°, respectively for calculating the discharge factor. Validation of simulation results shows that the unsteady stage and steady simulations are more accurate than unsteady TRS simulations for calculating the discharge factor at gva range 20° to 26° of the high head Francis turbine.

The maximum errors of 15.8% and 26.7% were obtained at gva 15° of the high head Francis turbine for computing of the discharge factor using unsteady TRS and stage simulations. The steady simulation predicted the discharge factor with 2.7% error at gva 15°. Generally, the simulations show less consistency in calculating the discharge factor compared to the speed factor. The discrepancy between experiments and CFD results in the prediction of the discharge factor may correspond to a number of limits in the CFD approach, including the choice of the turbulence model, time step and mesh resolution.

7.1.2 Computational cost

The additional steady and unsteady simulations of a high head Francis turbine at no-load condition were performed with different mesh densities and computational domains, on the same high performance computer (HPC) platform and the same number of CPU cores, shown in Table 7-1. In Table 7-1, the steady simulation is the fastest method for the computation of the no-load

speed. It could have been faster if the first operating point had been selected near the no-load speed curve. Thus, it is essential to develop an algorithm to select the starting point in the calculation. In general, the steady simulations provide a compromise between accuracy, and the computational effort required to calculate the no-load speed.

The unsteady TRS simulation required 6 times more simulation time than the unsteady stage calculation to converge on the same computer cluster and same number of CPU cores, as was shown in Table 7-1. Therefore, the main challenge of unsteady TRS simulations is dependency on more expensive computational costs.

Table 7-1 : Comparison of typical no-load simulations of a high head Francis turbine launched on a high performance computer (HPC) platform

case	Method	Interface model	Processes	Run mode	total number of nodes	Wall time
1	Steady	Stage	24	MPI	800k	6hr
2	Unsteady	Stage	24	MPI	800k	1day 18hr
3	Unsteady	Stage	24	MPI	1700k	4days
4	Unsteady	Transient rotor stator (TRS)	24	MPI	7000k	24days

7.1.3 Evolution of turbine flow behavior

One of the objectives of the simulations was to gain more insight into the flow behavior, pressure fluctuations in the turbine and draft tube at no-load condition. Numerical flow simulations in this regime were challenging to perform, because the flow is irregular and unstable, with large flow separation, vortex formations, and large amplitude pressure oscillations in the turbine and draft tube. In this regard, the steady simulations are obviously not able to capture the unsteady phenomena. Thus, the unsteady method was needed to study the flow physics, and pressure fluctuations at no-load condition.

The unsteady stage and TRS simulations predicted similar flow behavior inside the turbine at no-load condition of a medium head Francis turbine at gva 16º. Unsteady simulations revealed strong vortices near the leading edge, which block the runner inlet. In the draft tube, the strong tangential flow moves downward near the cone wall, and axial reversed flow moves upstream toward the runner hub close to the cone center.

Moreover, unsteady simulations showed a similar trend in runner speed and torque, as shown in Figure 7-1. Nevertheless, the torque fluctuations were under-predicted at the start and over-predicted at the end of the unsteady stage simulation, compared to unsteady TRS simulation. This discrepancy may be due to the averaging of the flux, applied by the stage model at the interface.

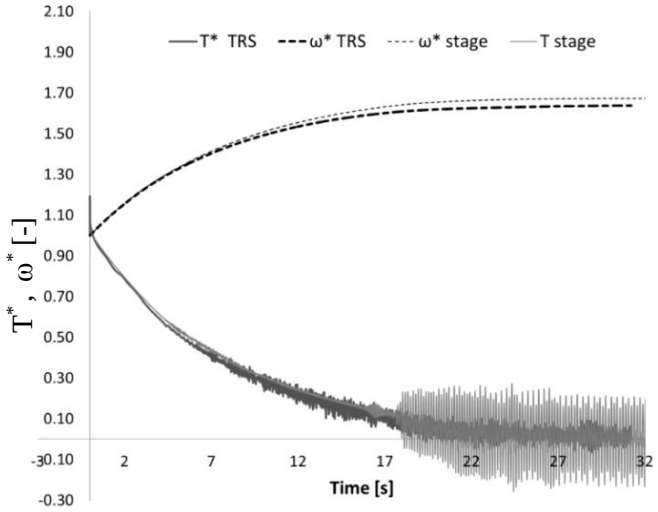

Figure 7-1: Evolution of dimensionless speed and torque during no-load simulation of a medium head Francis turbine at gva 16º

There are differences between unsteady TRS and stage simulations in computing the pressure on the blades. For instance, in the no-load simulation of a medium head Francis turbine, the unsteady stage simulation computed the maximum pressure on the suction side and average pressure on the pressure side 18% larger, and -39% less compared to unsteady TRS simulations, respectively.

The pressure signals on the blade, obtained in the unsteady simulations, were investigated using the fast Fourier Transform. The comparison of simulation results shows that the value of the peak amplitude predicted by unsteady stage simulation is 2.33 times larger than that predicted by the unsteady TRS simulation. The dominant normalized frequencies are almost the same.

7.2 Friction torque computation

The friction torque was calculated when estimating the total turbine torque during no-load and load-rejection simulations. The friction torque included the mechanical losses caused by operation of water in the hub and shroud. However, bearing shaft friction was ignored. The

impact of this quantity has not been discussed in similar investigations. Figure 7-2 compares the value of friction and turbine torque during convergence of a typical unsteady simulation of a medium head Francis turbine. It can be seen that the turbine torque oscillates with high amplitude, owing to the instability of the flow physics in the runner and the draft tube. It was found that during convergence, the average turbine torque accounts for 42% of the friction turbine torque. Thus, the computation of the friction torque leads to a more reliable representation of total torque during the transient process.

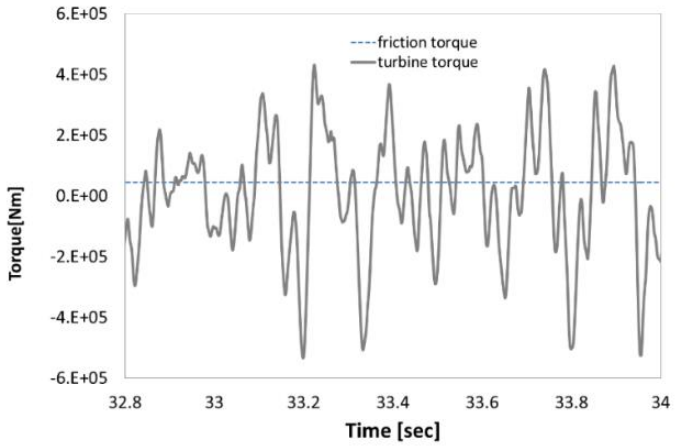

Figure 7-2 : Evolution of friction and turbine torque at the end of the runaway simulation for the medium head Francis turbine

7.3 Load rejection simulation

In this research work, the unsteady stage simulation of the no load condition is extended for modelling of load rejection. To reach this objective, the runner acceleration, and closing of guide vanes have been modelled simultaneously. The runner acceleration was computed using the equation of angular momentum for the rotating mass, stated in the second article.

In order to model the movement of guide vanes, mesh deformation was imposed on the nodes at the boundaries, and sub-regions of the mesh in the distributor channel during the solution process. The first objective was to model the entire guide vane movement using mesh deformation. However, deformations greater than 1° led to fatal error conditions because the displacement degraded the mesh quality during simulations. Thus, the mesh deformation of 1° was combined

with an external re-meshing loop. As described in the third article, a script code updated the mesh around the wicket gates using key-frame meshes based on the prescribed closing scenario by a re-meshing loop. This process was done in addition to the standard simulation workflow with the 1° mesh deformation.

The methodology was developed and validated by performing 3D unsteady simulations on a medium head Francis turbine. To limit the computational effort, the computational domain consisted of one distributor passage, a single runner channel, and the full draft tube. The stage interface model was used to connect the stationary and rotating parts. The simulation was completed in a computational time of 22 hours, on a high performance computer (HPC) platform with 24 CPU nodes. In the simulation, the movement of gva from 30° to 3° was performed. The unsteady simulation failed at gva less than 3° due to the poor quality of the mesh.

7.3.1 Comparison between unsteady simulations of load rejection and no-load condition

Unsteady stage simulations of the load rejection and no-load condition (gva 16°) at a medium head Francis turbine were compared concerning the computation of the flow field, pressure fluctuations and engineering quantities. Relatively similar flow behavior was observed during load rejection and no-load simulations. The simulation results revealed a strong swirling flow at the runner outlet, which caused flow separation and axial reversed flow in the draft tube cone center. These unsteady flow phenomena induced high pressure fluctuations in a fairly wide range of frequencies in the runner.

Figure 7-3 compares the pressure signals obtained by unsteady simulations of load rejection and no-load condition. The pressure signals were captured at monitoring points, located in the middle of the suction and pressure sides near the leading edge. It can be observed that the average pressure increases on the suction side during unsteady simulations. On the pressure side, the average pressure experienced a drop during load rejection, increasing slightly at no-load condition.

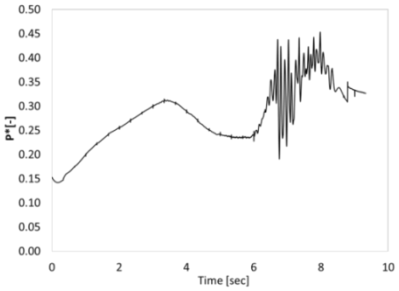

(a) Load rejection, suction side

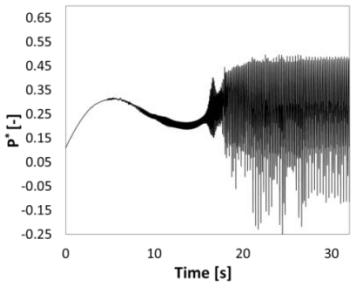

(b) No load condition(gva 16°), suction side

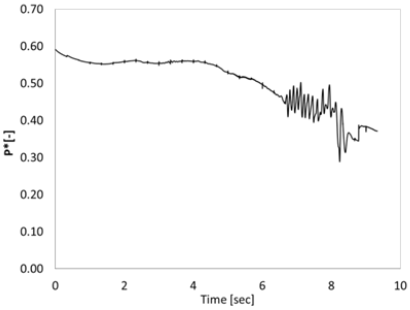

(c) Load rejection, pressure side

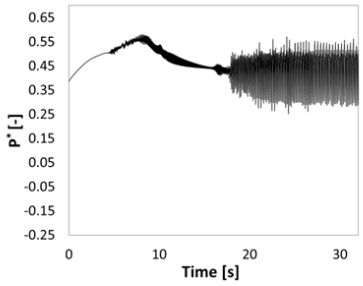

(d) No load condition(gva 16°), pressure side

Figure 7-3 : Time history of normalized pressure fluctuation in medium head-Francis turbine during load-rejection (left) and at no-load condition (right)

Strong pressure fluctuations were predicted at the end of the simulations. As mentioned in the second and third articles, the fluctuations occur when the turbine moves through conditions between zero and negative torque. At the no-load condition, the pressure fluctuates with larger amplitudes than during load rejection. This occurs because more hydraulic energy enters the turbine at no load condition with the fixed guide vanes. Consequently, a more complex flow is induced to dissipate hydraulic energy. The fast Fourier transform of pressure signals shows that the frequency of peak signals at load rejection is 1.45 times larger than that at no-load condition. The validation of load rejection results shows the unsteady simulations predicted pressure fluctuations at a much lower frequency range than experiments.

The evaluation of engineering parameters such as turbine angular speed was investigated during load rejection. Figure 7-4 compares the trend of the runner's speed during load rejection and no-load simulations (gva 16°) of a medium head Francis turbine. It was observed that the runner

accelerates at the start of both types of simulations. At the no-load condition, the speed growth rate decreases, and finally converges to nearly 170 percent of the synchronous speed, which is the maximum runner speed or no-load speed. During load rejection, the speed growth rate decreases and the runner reaches a maximum speed of 140 percent of the synchronous speed. Contrary to the no load simulation, the runner speed drops at the end of the load rejection simulation due to the closing of the guide vanes.

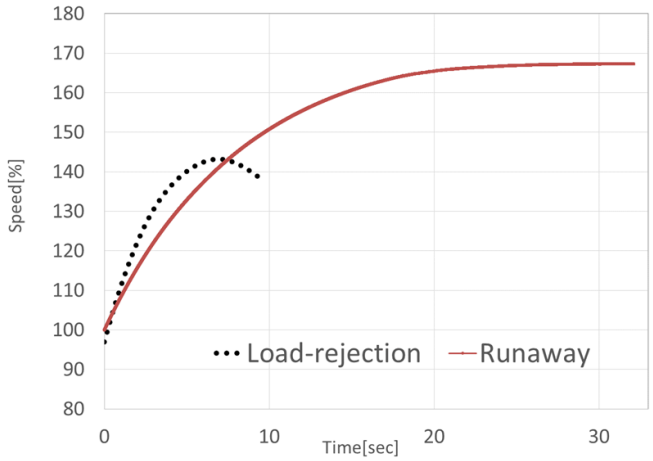

Figure 7-4 : Evolution of the runner's speed during load rejection and no-load simulations at the medium head turbine

The difference between simulation results and experimental measurements for the prediction of the maximum speed was 9% and 5.98% at the load rejection and no load condition (gva 16°), respectively. The no load simulations predict the maximum speed more accurately than load rejection simulations. This difference is attributed to the uncertainty in the modelling of the movement of guide vanes. During the load rejection simulations, the interpolation of the previous results to the new mesh in the re-meshing loop may cause some error. To decrease the uncertainty during the load rejection simulation, the mesh deformation must be performed on a large-scale movement of the guide vanes, as well as a reduction in the number of re-meshing loops. This improvement is highly dependent on the usage of higher quality meshes in terms of volume ratio, minimum angle, skewness, and aspect ratio.

7.3.2 Mesh quality during load rejection

Figure 7-5 illustrates the evolution of the meshes inside the guide vane channel during mesh deformation modeling in a load rejection simulation of a medium head Francis turbine. Figure 7-6 presents histograms for three mesh quality parameters computed on the mesh. As shown by these histograms, the distributions of these important parameters for guide vane slightly change during mesh deformation.

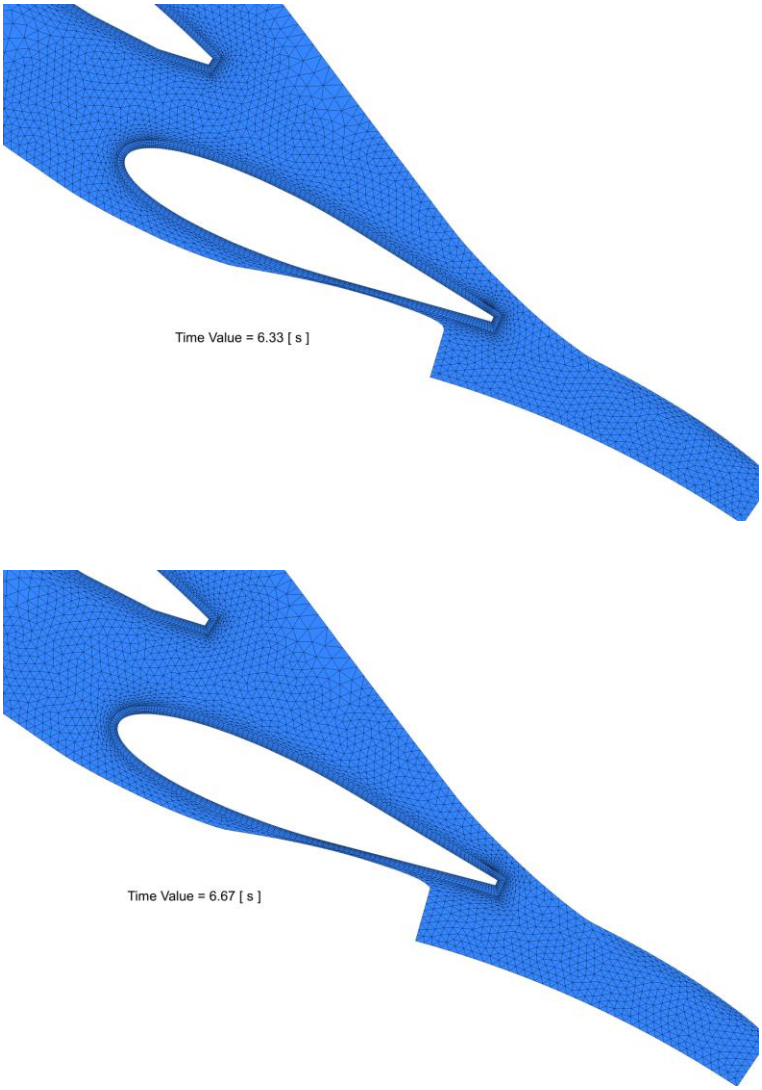

Figure 7-5 : Evolution of meshes in the guide vane channel during a load rejection simulation between t=6.33 s to 6.67 s

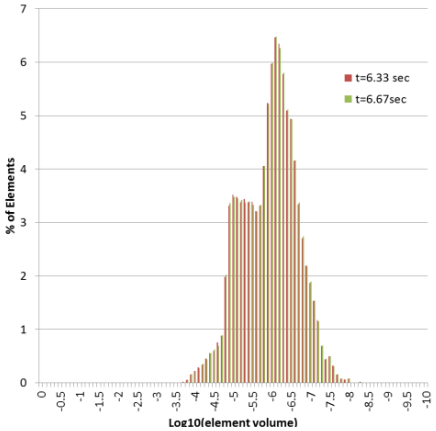

(a)

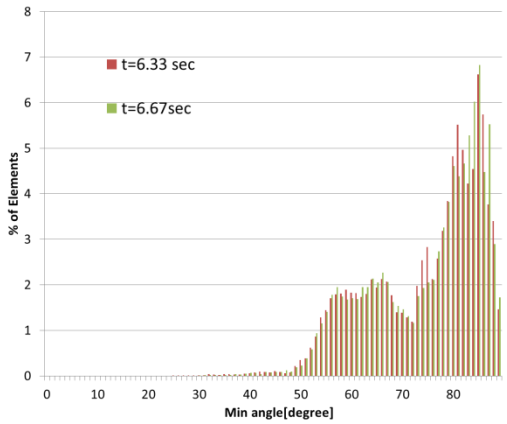

(b)

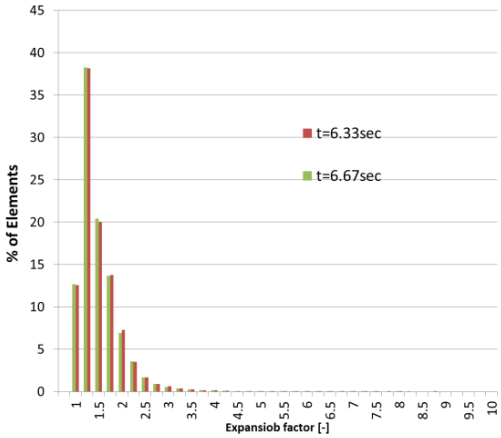

(c)

Figure 7-6 : Evolution of mesh quality histograms (a) Element volume (log value) distribution, (b) Minimum angle distribution,(c) Expansion factor distribution during a load rejection simulation between t=6.33 s to 6.67 s

7.4 Summary

Generally, the unsteady and steady simulations were applied for computing the no-load speed of a medium and a high head Francis turbine. In addition, the flow behavior, pressure fluctuations inside turbine and draft tube were investigated during load-rejection and at no-load condition.

The CFD results have demonstrated consistency in the prediction of the speed factor at no-load. There were significant discrepancies in the prediction of the discharge factor between CFD results and experiments that may correspond to the influence of the mesh quality, time resolution, the interface model, and the turbulence model.

As mentioned in the second article, the stage interface may affect the prediction the fluctuation of runner torque, the peak amplitude of pressure fluctuations, the average and maximum pressure on the blades during the no load condition.

In the thesis, the standard k-ε turbulence model, a robust and simple model, was used to develop methodologies with relatively low computational effort. Nevertheless, the RANS models are not capable of predicting all aspects of the flow, at no-load conditions with full accuracy. In order to provide more reliable results, more advanced turbulence models such as the Reynolds stress model or filtering methods such as Large eddy simulation (LES) may be required.

Another challenge in the development of CFD methods of operating conditions such as load rejection and no-load is the detailed validation of simulation results. This challenge is due to the fact that obtaining good measurement data such as unsteady pressure field in the runner and draft tube is both difficult and very expensive. More experimental research activities are needed to assess the reliability of the proposed methods, in order to apply it in the design process.

CHAPTER 8 CONCLUSION AND RECOMMENDATIONS

8.1 Conclusion and contributions

This research study has proposed, developed and evaluated numerical simulation methodologies, in modelling the Francis turbine during runaway, no-load conditions and load-rejection. The main outcome of the thesis was the development of a methodology used to simulate the load rejection, using simultaneously the modelling of the runner acceleration, and the movement of the guide vanes. Collaboration with Andritz Hydro Canada in this project led to an evaluation of the proposed methodology for a medium and a high head Francis turbine.

Two methodologies were developed and compared using the steady and unsteady simulations for calculating the no-load speed of Francis turbines. The unsteady simulations were performed for two geometric configurations: the complete turbine, and a single runner/distributor passage. The transient-rotor stator (TRS) and stage interface models were used to match stationary and rotating parts.

The turbine's dynamic parameters such as speed and discharge factors at no-load condition were computed and validated for a wide range of guide vane angles of a medium and a high head Francis turbine. The unsteady TRS simulations were found more accurate than the steady and unsteady stage simulations for calculating the speed factor at many opening angles, except at a gva of 15° of the high head Francis turbine.

The unsteady stage simulation is more accurate at gva from 13.5° to 20° for the medium head Francis turbine for calculating discharge factor than unsteady TRS and steady simulations. For the high head Francis turbine the unsteady stage and steady simulations were found more accurate than unsteady TRS simulation at gva from 20° to 26°.

Generally, the unsteady and steady simulations showed consistency for calculating the speed factor at no-load. Significant discrepancies between CFD results and experiments were computed in the prediction of the flow discharge factor, which may be attributed to a number of limits in the CFD approach, including the choice of the turbulence model, and limited spatial and temporal resolution.

The main advantage of the steady simulations was the ability to compute the no load speed in a short period of time with limited computational power compared to the unsteady simulations. In general, steady simulations provided a compromise between accuracy and required computational effort for calculating the no load speed.

The unsteady simulations were successfully used to analyze the operation of the Francis turbine at the no-load condition. The simulations led to a deeper understanding of the flow behavior and pressure fluctuations in the turbine and draft tube.

The unsteady TRS and stage simulations were compared in order to determine the influence of interface models on the accuracy of the results. The simulations predicted a similar trend in the runner speed, torque and flow behavior inside the turbine during the no-load condition of a medium head Francis turbine. However, the unsteady TRS simulation was capable of predicting more details of the torque and pressure fluctuations during the transient process. In addition, the simulation results showed sizeable differences in computing the pressure on the blades between TRS and stage simulations.

To investigate the operation of the Francis turbine during load rejection condition, a methodology was developed and validated, by performing 2D and 3D unsteady simulations. The runner acceleration during load rejection was modelled by an angular momentum equation, similar to the method applied in the no-load simulation. A combination of mesh deformation and re-meshing techniques was applied to simulate the guide vane movements of the Francis turbine during load-rejection.

The evolution of engineering quantities such as the runner speed, torque and inlet flow rate was investigated during load rejection. A discrepancy of 9% was observed between the simulation results and experiments for the prediction of the maximum runner speed. The pressure signals on the blade were evaluated, and validated during load rejection. Strong pressure signals were predicted at the leading edge by unsteady simulations and experiments. The fluctuations were computed by unsteady simulations at a much lower frequency range than experiments.

The unsteady simulations predicted similar flow behavior during load rejection and no-load conditions. The simulations showed that the flow inside the draft tube is separated into two concentric flow areas. The swirling flow moves downstream in the outer region near the wall. A reversing flow moves upstream toward the runner hub in the inner region. These complex flow

structures dissipate the hydraulic input energy in the turbine, and induce pressure fluctuations with a fairly wide range of frequencies. At the no-load condition, the pressure fluctuates with larger amplitudes than during load rejection because more hydraulic energy passes in the turbine with fixed guide vanes.

Overall, the load rejection and no load conditions produce complex flow structures inside Francis turbines which must be investigated to ensure the mechanical safety of hydraulic machines. In this regard, the proposed methodologies were able to present a qualitative analysis of the flow physics and turbine behavior during load rejection and no load conditions.

The main challenge in the development of CFD studies was the validation of unsteady simulations. Obtaining good experimental data such as pressure distribution on the runner or draft tube during load rejection, runaway and at no-load conditions is difficult and very expensive.

8.2 Recommendations for future studies

Regarding the research contributions and proposed methods used to simulate the Francis turbine operation during load rejection and no-load condition, the following subjects are recommended for future work.

The steady simulations, presented in the first article, were simple and fast when calculating the no load speed of the Francis turbine at different guide vane angles, in comparison with the unsteady simulations. Nevertheless, the steady simulations could be faster if the starting point is chosen near the no-load curve. Hence, it is recommended to improve the algorithm to choose the starting point for no-load speed calculations. For instance, to perform simulations on a sequence of guide vane angles. In this case, the first calculation starts from the runner angular speed at best efficiency point for the smallest guide vane angle. The next steady simulation can be continuing from no-load speed of the previous opening angle.

The load rejection simulation was performed only for one shut down scenario of a medium head Francis. The influence of different rates of guide vane movement on the unsteady loads, as well as on the runner blades, could be studied.

The simulation of the Francis turbine during load rejection was implemented on a single runner/distributor passage connected through a stage interface model to limit the computational cost. However, the stage model neglects some transient effects, because it performs

circumferential averaging of the fluxes at the interfaces. The natural next step of the proposed methodology is the simulation on the complete turbine, using transient rotor-stator for an accurate prediction of unsteady loads. Regarding the increase of computational capacity in the near future, the unsteady simulations using more advanced turbulence models such as the Reynolds stress model with finer meshes and time steps may be applied to predict more details of vortical flow and pressure fluctuations.

In this thesis, the movement of guide vanes was simulated using the combination of re-meshing and mesh deformation techniques. However, the simulation of the guide vane angles less than 3° was not possible due to low mesh quality. It would be useful to apply and compare other techniques to simulate movement of guide vanes. Among the various alternatives we distinguish the explicit mesh deformation technique, based on Inverse Distance Weighting (IDW) interpolation (Casartelli et al., 2014).

BIBLIOGRAPHY

Afshar, M. H., Rohani, M., & Taheri, R. (2010). Simulation of transient flow in pipeline systems due to load rejection and load acceptance by hydroelectric power plants. *International Journal of Mechanical Sciences, 52*(Copyright 2010, The Institution of Engineering and Technology), 103-115.

Alligné, S., Maruzewski, P., Dinh, T., Wang, B., Fedorov, A., Iosfin, J., & Avellan, F. (2010). *Prediction of a Francis turbine prototype full load instability from investigations on the reduced scale model.* Paper presented at the IOP Conference Series: Earth and Environmental Science.

Anand, M., Pope, S., & Mongia, H. (1993). *PDF calculations for swirling flows.* Paper presented at the 31st AIAA Aerospace Sciences Meeting and Exhibit.

ANDRITZ Hydro. (2014). Final High and Low Head Francis Turbine Test Report.

ANSYS CFX-User manual. Release 13 : Theory.

Antonsen, Ø. (2007). Unsteady flow in wicket gate and runner with focus on static and dynamic load on runner.

Bilgen, E., & Boulos, R. (1973). Functional Dependence of Torque Coefficient of Coaxial Cylinders on Gap Width and Reynolds Numbers. *Journal of Fluids Engineering, 95*(1), 122-126. doi: 10.1115/1.3446944

Casartelli, E., Mangani, L., Romanelli, G., & Staubli, T. (2014). Transient Simulation of Speed-No Load Conditions With An Open-Source Based C++ Code. *IOP Conference Series: Earth and Environmental Science, 15*(6), 062014.

Casartelli, E., Mangani, L., Romanelli, G., & Staubli, T. (2014). Transient Simulation of Speed-No Load Conditions With An Open-Source Based C++ Code. *IOP Conference Series: Earth and Environmental Science, 22*(3), 032029.

Cherny, S., Chirkov, D., Bannikov, D., Lapin, V., Skorospelov, V., Eshkunova, I., & Avdushenko, A. (2010). 3D numerical simulation of transient processes in hydraulic turbines. *IOP Conference Series: Earth and Environmental Science, 12*(1), 012071.

Côté, P., Dumas, G., Moisan, É., & Boutet-Blais, G. (2014). Numerical investigation of the flow behavior into a Francis runner during load rejection. *IOP Conference Series: Earth and Environmental Science, 22*(3), 032023.

Côté, P., Dumas, G., Moisan, É., & Boutet-Blais, G. (2014). Numerical investigation of the flow behavior into a Francis runner during load rejection. *IOP Conference Series: Earth and Environmental Science, 15*(6), 062014.

Coutu, A., Lauzon, J., Monette, C., Nennemann, B., & Huang, X. (2013). *Francis Runner: Cost of Operation, Presentation.* Paper presented at the 5th IAHR International Workshop on Cavitation and Dynamic Problems in Hydraulic Machinery, Lausanne, Switzerland, Sept.

Davidson, P. A. (2004). *Turbulence: an introduction for scientists and engineers*: Oxford University Press.

Dorfler, P. (2009). *Evaluating 1D models for vortex-induced pulsation in Francis turbines.* Paper presented at the 3rd IAHR International Meeting of the Workgroup on Cavitation and Dynamic Problems in Hydraulic Machinery and Systems, Brno, Czech Republic, Oct.

Dörfler, P., Sick, M., & Coutu, A. (2013). *Flow-induced pulsation and vibration in hydroelectric machinery: engineer's guidebook for planning, design and troubleshooting ; Peter Dorfler, Mirjam Sick, Andre Coutu*. London, [Angleterre]: Springer.

Fortin, M., Houde, S., & Deschênes, C. (2014). Validation of simulation strategies for the flow in a model propeller turbine during a runaway event. *IOP Conference Series: Earth and Environmental Science, 22*(3), 032026.

Galvan S , Reggio M , & Guibault F. (2011). Assessment study of k -E turbulence models and near-wall modeling for steady state swirling flow analysis in a draft tube using Fluent. *Engineering Applications of Computational Fluid Mechanics, 5*(4), 459-478.

Galvan, S., Reggio, M., & Guibault, F. (2011). Assessment study of k-epsilon turbulence models and near-wall modeling for steady state swirling flow analysis in a draft tube using Fluent. *Engineering Applications of Computational Fluid Mechanics, 5*(4), 459-478.

Guo, C., Wang, G., & Xiao, J. (2009, 27-31 March 2009). *Numerical Simulation for Hydraulic Characteristics of Cylindrical Valve in Runaway Protection Process.* Paper presented at the Power and Energy Engineering Conference, APPEEC 2009. Asia-Pacific.

Hasmatuchi, V., Farhat, M., Roth, S., Botero, F., & Avellan, F. (2011). Experimental Evidence of Rotating Stall in a Pump-Turbine at Off-Design Conditions in Generating Mode. *Journal of Fluids Engineering, 133*(5), 051104-051104. doi: 10.1115/1.4004088

Hosseinimanesh, H., Devals, C., Nennemann, B., & Guibault, F. (2015). Comparison of steady and unsteady simulation methodologies for predicting no-load speed in Francis turbines. *International Journal of Fluid Machinery and Systems, 8*(3), 155-168.

Hosseinimanesh, H., Devals, C., Nennemann, B., Reggio, M., & Guibault, F. (2015). A numerical study of Francis turbine operation at no-load condition. *Journal of Fluids Engineering, under review*.

Hosseinimanesh, H., Vu, T. C., Devals, C., Nennemann, B., & Guibault, F. (2014). A steady-state simulation methodology for predicting runaway speed in Francis turbines. *IOP Conference Series: Earth and Environmental Science, 22*(3), 032027.

Hosseinimanesh, H., Vu, T. C., Devals, C., Nennemann, B., & Guibault, F. (2014). A steady-state simulation methodology for predicting runaway speed in Francis turbines. *IOP Conference Series: Earth and Environmental Science, 16*(3), 032044.

Houde, S., Fraser, R., Ciocan, G., & Deschênes, C. (2012). Experimental study of the pressure fluctuations on propeller turbine runner blades: part 2, transient conditions. *IOP Conference Series: Earth and Environmental Science, 15*(6), 062061.

Huang, W., Fan, H., & Chen, N. (2012). *Transient simulation of hydropower station with consideration of three-dimensional unsteady flow in turbine.* Paper presented at the IOP Conference Series: Earth and Environmental Science.

Ida, T. (1989). Analysis of scale effects on performance characteristics of hydraulic turbines: Part 1: Scale formulae of hydraulic performance and loss distribution coefficients in model Francis turbines and pump-turbines. *Journal of Hydraulic Research, 27*(6), 809-831.

IEC60193. (1999-2011) *Hydraulic turbines, storage pumps and pump-turbines-model acceptance tests*

IEC61364. (1999) *Nomenclature for Hydroelectric Powerplant Machinery*.

Joukowsky, N. (1900). *Über den hydraulischen stoss in wasserleitungsrohren*.

Kolšek, T., Duhovnik, J., & Bergant, A. (2006). Simulation of unsteady flow and runner rotation during shut-down of an axial water turbine. *Journal of Hydraulic Research, 44*(1), 129-137. doi: 10.1080/00221686.2006.9521668

Levchenya, A. M., Smirnov, E. M., & Goryachev, V. D. (2010). RANS-based numerical simulation and visualization of the horseshoe vortex system in the leading edge endwall region of a symmetric body. *International Journal of Heat and Fluid Flow, 31*(6), 1107-1112. doi: http://dx.doi.org/10.1016/j.ijheatfluidflow.2010.06.014

LI, J., LIU, S., ZHOU, D., & WU, Y. (2009). Threedimensional unsteady simulation of the runaway transient of the Francis turbine. *Journal of Hydroelectric Engineering, 28*(1), 178-182.

Li, J., Wu, Y., Liu, S., & Zhu, Y. (2007). 3D Unsteady Turbulent Simulation of the Runaway Transient of the Francis Turbine. *ASME Conference Proceedings, 2007*(42886), 2005-2011.

Li, J., Yu, J., & Wu, Y. (2010). 3D unsteady turbulent simulations of transients of the Francis turbine. *IOP Conference Series: Earth and Environmental Science, 12*(1), 012001.

Li, Y., Song, G., & Yan, Y. (2015). Transient hydrodynamic analysis of the transition process of bulb hydraulic turbine. *Advances in Engineering Software, 90*, 152-158. doi: 10.1016/j.advengsoft.2015.08.006

Liu, J. T., Liu, S. H., Sun, Y. K., Wu, Y. L., & Wang, L. Q. (2012). Numerical study of vortex rope during load rejection of a prototype pump-turbine. *IOP Conference Series: Earth and Environmental Science, 15*(3), 032044.

Liu, S., Zhou, D., Liu, D., Wu, Y., & Nishi, M. (2010). Runaway transient simulation of a model Kaplan turbine. *IOP Conference Series: Earth and Environmental Science, 12*(1), 012073.

Magnan, R., Cupillard, S., Gauthier, G., Giroux, A., Page, M., & Deschênes, C. (2014). *Challenges in assessing the grid sensitivity of hydro-turbine CFD simulations.* Paper presented at the IOP Conference Series: Earth and Environmental Science.

Maruzewski, P., Hayashi, H., Munch, C., Yamaishi, K., Hashii, T., Mombelli, H. P., . . . Avellan, F. (2010). Turbulence modeling for Francis turbine water passages simulation. *IOP Conference Series: Earth and Environmental Science, 12*(1), 012070.

Melot, M., Monette, C., Coutu, A., & Nennemann, B. (2014). A new standard Francis runner design procedure to predict static stresses stresses at speed-no-load *Hydropower & Dams (1)*.

Nennemann, B., Morissette, J., Chamberland-Lauzon, J., Monette, C., Braun, O., Melot, M., . . . Giroux, A. (2014). *Challenges in Dynamic Pressure and Stress Predictions at No-Load Operation in Hydraulic Turbines.* Paper presented at the IOP Conference Series: Earth and Environmental Science.

Nennemann, B., Morissette, J. F., Chamberland-Lauzon, J., Monette, C., Braun, O., Melot, M., . . . Giroux, A. M. (2014). Challenges in Dynamic Pressure and Stress Predictions at No-Load Operation in Hydraulic Turbines. *IOP Conference Series: Earth and Environmental Science, 22*(3), 032055.

Nennemann, B., Vu, T. C., & Farhat, M. (2005). *CFD prediction of unsteady wicket gate-runner interaction in Francis turbines: A new standard hydraulic design procedure*. Paper presented at the HYDRO 2005 International Conference and Exhibition, Villach, Austria. http://infoscience.epfl.ch/record/90762

Nicolet, C. (2007). *Hydroacoustic modelling and numerical simulation of unsteady operation of hydroelectric systems.* EPFL. Retrieved from http://infoscience.epfl.ch/record/98534

Nicolet, C., Arpe, J., & Avellan, F. (2004). *Identification and Modeling of Pressure Fluctuations of a Francis Turbine Scale Model at Part Load Operation*. Paper presented at the Proceedings of the 22nd IAHR Symposium on Hydraulic Machinery and Systems 2004. http://infoscience.epfl.ch/record/59061

Nicolle, J., Morissette, J. F., & Giroux, A. M. (2012). Transient CFD simulation of a Francis turbine startup. *IOP Conference Series: Earth and Environmental Science, 15*(6), 062014.

Nilsson, S. (1997). Hydro unit start-up costs and their impact on the short term scheduling strategies of Swedish power producers-Reply.

Ren, R. (2015). Global status report. *Renewable Energy Policy Network for the 21st Century, Paris, France*.

Round, G. F. (2004). *Incompressible flow turbomachines: design, selection, applications, and theory*: Butterworth-Heinemann.

Ruprecht, A., Helmrich, T., Aschenbrenner, T., & Scherer, T. (2002, 2002). *Simulation Of Vortex Rope In A Turbine Draft Tube* Paper presented at the the Hydraulic Machinery and Systems 21st IAHR Symposium, Lausanne

Ruprecht, A., Helmrich, T., Aschenbrenner, T., & Scherer, T. (2002). *Simulation of vortex rope in a turbine draft tube.* Paper presented at the Proceedings of 22nd IAHR Symposium on Hydraulic Machinery and Systems.

Schlichting, H., & Gersten, K. (2000). *Boundary-Layer Theory*: MacGraw-Hill.

Seleznev, V. S., Liseikin, A. V., Bryksin, A. A., & Gromyko, P. V. (2014). What Caused the Accident at the Sayano–Shushenskaya Hydroelectric Power Plant (SSHPP): A Seismologist's Point of View. *Seismological Research Letters, 85*(4), 817-824.

Sjelvgren, D. (1997). Hydro unit start-up costs and their impact on the short term scheduling strategies of Swedish power producers. *Power Systems, IEEE Transactions on, 12*(1), 38-44.

Stanislav Pejovic, B. K., Qinfen Zhang. (2004). *Water Column Separation in Long Tailrace Tunnel*. Paper presented at the Hydroturbo 2004, on Hydro-Power Engineering, Brno.

Staubli, T., Senn, F., & Sallaberger, M. (2008). Instability of pump-turbines during start-up in turbine mode. *Hydro2008, Ljubljana, Slovenia, Paper*(9.6).

Streeter, V. L., & Wylie, E. B. (1993). *Fluid transients in systems*. Englewood Cliffs, N.J.: Prentice Hall.

Swaffield, J. A. (1993). *Pressure surge in pipe and duct systems*. Avebury: Aldershot.

Trivedi, C. (2014). Investigations of Transient Pressure Loading on a High Head Francis Turbine.

Trivedi, C. (2014). *Investigations of Transient Pressure Loading on a High Head Francis Turbine.* (PhD thesis), Lulea University of Technology, Sweden.

Trivedi, C., Cervantes, M. J., Dahlhaug, O. G., & Gandhi, B. K. (2015). Experimental Investigation of a High Head Francis Turbine During Spin-No-Load Operation. *Journal of Fluids Engineering, 137*(6), 061106-061106. doi: 10.1115/1.4029729

Trivedi, C., Cervantes, M. J., Gandhi, B., & Dahlhaug, O. G. (2014). Experimental investigations of transient pressure variations in a high head model Francis turbine during start-up and shutdown. *Journal of Hydrodynamics, Ser. B, 26*(2), 277-290.

Trivedi, C., Cervantes, M. J., Gandhi, B., & Dahlhaug, O. G. (2014). Pressure measurements on a high-head Francis turbine during load acceptance and rejection. *Journal of Hydraulic Research, 52*(2), 283-297.

Trivedi, C., Cervantes, M. J., Gandhi, B. K., & Dahlhaug, O. G. (2013). Experimental and Numerical Studies for a High Head Francis Turbine at Several Operating Points. *Journal of Fluids Engineering, 135*(11), 111102-111102. doi: 10.1115/1.4024805

Trivedi, C., Cervantes, M. J., Gandhi, B. K., & Dahlhaug, O. G. (2014). Transient Pressure Measurements on a High Head Model Francis Turbine During Emergency Shutdown, Total Load Rejection, and Runaway. *Journal of Fluids Engineering, 136*(12), 121107. doi: 10.1115/1.4027794

Trivedi, C., Gandhi, B., & Cervantes, M. J. (2013). Effect of transients on Francis turbine runner life: a review. *Journal of Hydraulic Research, 51*(2), 121-132.

Vu, T. C., Devals, C., Zhang, Y., Nennemann, B., & Guibault, F. (2011). Steady and unsteady flow computation in an elbow draft tube with experimental validation. *International Journal of Fluid Machinery and Systems, 4*(1), 85-96. doi: 10.5293/IJFMS.2011.4.1.085

Vu, T. C., Devals, C., Zhang, Y., Nennemann, B., Guibault, F., ccedil, & ois. (2011). Steady and unsteady flow computation in an elbow draft tube with experimental validation. *International Journal of Fluid Machinery and Systems, 4*(1), 85-96. doi: 10.5293/ijfms.2011.4.1.085

Vu, T. C., & Retieb, S. (2002). *Accuracy assessment of current CFD tools to predict hydraulic turbine efficiency hill chart.* Paper presented at the Proceedings of the 21st IAHR Symposium on Hydraulic Machinery and Systems.

Wagner, H. J., & Mathur, J. (2011). *Introduction to Hydro Energy Systems: Basics, Technology and Operation*: Springer.

Warnick, C. C. (1984). *Hydropower engineering*: Prentice-Hall.

Widmer, C., Staubli, T., & Ledergerber, N. (2011). Unstable Characteristics and Rotating Stall in Turbine Brake Operation of Pump-Turbines. *Journal of Fluids Engineering, 133*(4), 041101-041101. doi: 10.1115/1.4003874

Wikipedia, T. F. E. (2016). False position method, from https://en.wikipedia.org/w/index.php?title=False_position_method&oldid=711388970

Witteveen, J., & Bijl, H. (2009). *Explicit mesh deformation using inverse distance weighting interpolation.* Paper presented at the 19th AIAA Computational Fluid Dynamics Conference, AIAA, San Antonio, Texas, AIAA Paper.

Xiao, J., Zhu, E., & Wang, G. (2012). Numerical simulation of emergency shutdown process of ring gate in hydraulic turbine runaway. *Journal of Fluids Engineering, 134*(12), 124501.

Yan, J. P., Seidel, U., & Koutnik, J. (2012). Numerical simulation of hydrodynamics in a pump-turbine at off-design operating conditions in turbine mode. *IOP Conference Series: Earth and Environmental Science, 15*(3), 032041.